Mechanical Behavior of Meteorites:

Multiscale Characterization of the Strength and Failure Mechanism

by

Md Fazle Rabbi

A Dissertation Presented in Partial Fulfillment
of the Requirements for the Degree
Doctor of Philosophy

Approved July 2023 by the
Graduate Supervisory Committee:

Aditi Chattopadhyay, Co-Chair
Laurence A.J. Garvie, Co-Chair
Yongming Liu
Masoud Yekani Fard
Desiree Cotto-Figueroa

ARIZONA STATE UNIVERSITY

August 2023

ABSTRACT

In this research, the chemical and mineralogical compositions, physical and mechanical properties, and failure mechanisms of two ordinary chondrite (OCs) meteorites Aba Panu (L3) and Viñales (L6), and the iron meteorite called Gibeon (IVA) were studied. OCs are dominated by anhydrous silicates with lesser amounts of sulfides and native Fe-Ni metals, while Gibeon is primarily composed of Fe-Ni metals with scattered inclusions of graphite and troilite. The OCs were investigated to understand their response to compressive loading, using a three-dimensional (3-D) Digital Image Correlation (DIC) technique to measure full-field deformation and strain during compression. The DIC data were also used to identify the effects of mineralogical and structural heterogeneity on crack formation and growth. Even though Aba Panu and Viñales are mineralogically similar and are both classified as L ordinary chondrites, they exhibit differences in compressive strengths due to variations in chemical compositions, microstructure, and the presence of cracks and shock veins. DIC data of Aba Panu and Viñales show a brittle failure mechanism, consistent with the crack formation and growth from pre-existing microcracks and porosity. In contrast, the Fe-Ni phases of the Gibeon meteorite deform plastically without rupture during compression, whereas during tension, plastic deformations followed by necking lead to final failure. The Gibeon DIC results showed strain concentration in the tensile gauge region along the sample edge, resulting in the initiation of new damage surfaces that propagated perpendicular to the loading direction. Finally, an in-situ low-temperature testing method of iron meteorites was developed to study the response of their unique microstructure and failure mechanism.

ACKNOWLEDGMENTS

The completion of this dissertation was made possible by the contributions of many individuals to whom I am deeply grateful. I would like to express my sincere appreciation to my advisor, Regents' Professor Aditi Chattopadhyay, for her unwavering guidance, support, and insightful advice throughout my doctoral study. I am immensely grateful for her invaluable contributions that have shaped the direction of my research and motivated me to strive for excellence. I also extend my thanks to Dr. Laurence Garvie for his inspiration, motivation, and intellectual support at every step of the journey. His invaluable insights have greatly influenced the quality of my research. I am thankful to the members of my supervisory committee, Dr. Desiree Cotto-Figueroa, Dr. Yongming Liu, and Dr. Masoud Yekani Fard, for their time, expertise, and constructive feedback. I would like to acknowledge Dr. Erik Asphaug for sharing his knowledge and expertise on meteorites and asteroids, enriching the depth of my research. I am grateful to the faculty and staff of the Department of Mechanical Engineering at ASU for fostering a conducive academic environment. My deepest appreciation goes to my colleagues and fellow researchers at Professor Chattopadhyay's research center for their camaraderie, insightful discussions, and collaborative spirit, which have been instrumental in my growth as a researcher. Finally, I am profoundly thankful to my parents and my wife for their unwavering love, encouragement, and understanding, especially my wife's exceptional patience with our twin kids, throughout this endeavor.

I would also like to express my gratitude to the National Aeronautics and Space Administration for their funding support through Grant 80NSSC18K1444 and 80NSSC21K1983, provided under the SSO Near-Earth Object Observations and YORPD Program. Their support has been invaluable to the successful execution of this research.

TABLE OF CONTENTS

Page

CHAPTER Page

LIST OF TABLES

Table Page

LIST OF FIGURES

Figure Page

Figure Page

Figure Page

Figure Page

Figure Page

CHAPTER 1

INTRODUCTION

1.1 Background

Meteorites are extraterrestrial stony and metallic fragments of early solar system materials (Grady et al., 2006; McSween Jr et al., 2006; Walker and Cameron, 2006). They survived the energetic passage through our atmosphere and impacted the Earth's surface. A wide range of extraterrestrial materials are available for study, including rocks, debris, soil, regolith, and planetary dust. These materials have been collected through sample return missions such as NASA's Apollo lunar mission (Taylor, 2016), the Stardust mission (Brownlee, 2014), NASA's OSIRIS-REx (Lauretta et al., 2017), Hayabusa mission (Yoshikawa et al., 2015), and as meteorites found on Earth. The analysis of these samples provides valuable insights into the origin and formation of the solar system (Lauretta and McSween, 2006). Detailed examination of their mineralogy, composition, and isotopes helps us understand their origins and the processes that shaped their parent bodies (Lauretta and McSween, 2006). Currently, there are approximately 70,000 classified meteorites (https://www.lpi.usra.edu/meteor/), of which about 73% belong to the class known as ordinary chondrites (OC) (Grady et al., 2000). Although asteroids analogous to OCs represent a small fraction of the overall asteroid population, they share many similarities with near-Earth objects (NEOs) in terms of spectral properties (Binzel et al., 2002; Bottke Jr et al., 2002).

The NEO population is dominated by asteroids and rare comets, with sizes ranging from dust grains to tens of kilometers in diameter (Jedicke et al., 2002; Shoemaker, 1983). Some NEOs have orbits within a certain proximity to Earth (perihelion distance $q \leq 1.3$ AU; http://neo.jpl.nasa.gov/neo/groups.html) and similar orbital speeds, increasing the likelihood

of an encounter. As of May 2023, approximately 32,000 Near-Earth Objects (NEOs) have been identified through night sky surveys using telescopes, and this number continues to grow at a rate of nearly 3,000 additions per year (source: https://cneos.jpl.nasa.gov). It is estimated that there are still many NEOs with sizes ranging from 100 to 1000 meters that are yet to be discovered (Figure 1). Among these NEOs, around 20,500 are larger than 100 meters, with approximately 4,700 having a minimum orbit intersection distance (MOID) with Earth of less than or equal to 0.05 AU, classifying them as potentially hazardous (Mainzer et al., 2011). These potentially hazardous asteroids (PHA) pose a significant threat to human existence.

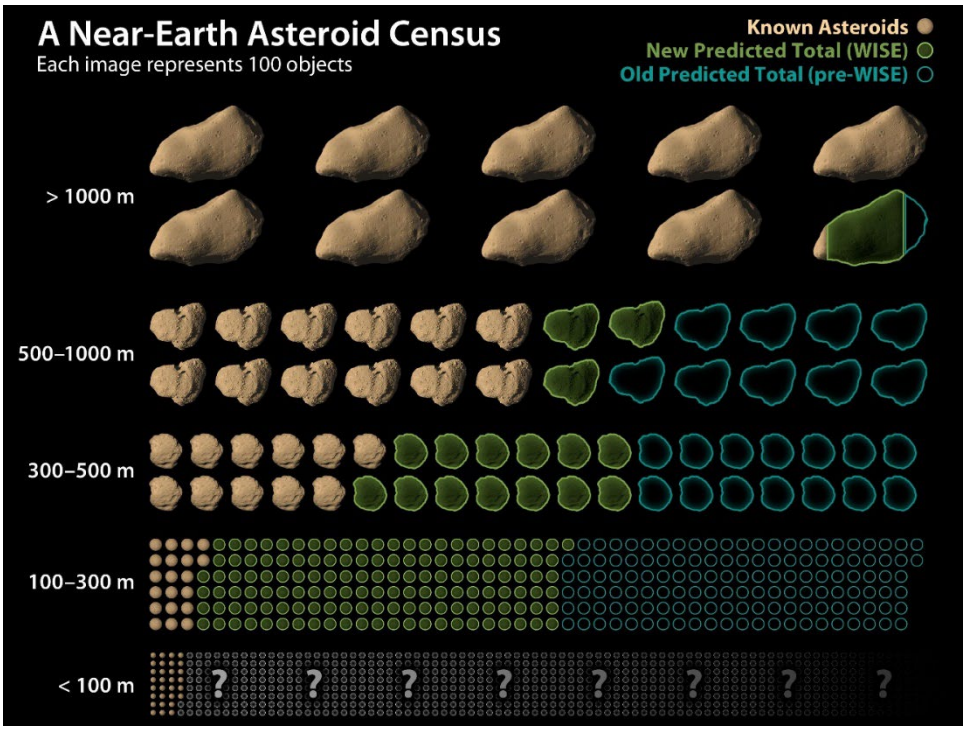

Figure 1. Chart of Discovered NEOs from the NASA Wide-Field Infrared Survey Explorer (WISE) with Estimated Numbers of Undiscovered Asteroids by Size. The Chart Shows That the Majority of Large Asteroids Have Been Discovered, but the Vast Majority of Small Asteroids Remain Undiscovered. Image Credit: Nasa/JPL-Caltech

A well-known asteroidal impact occurred near the Russian city of Chelyabinsk in 2013, releasing an estimated impact energy of 470 kt and injuring about 1500 people from the resulting shockwave, causing a natural disaster in a region with a population of over a million (Popova et al., 2013; Yeomans and Chodas, 2013). This 17 m bolide produced the largest airburst on Earth since the 1908 Tunguska event (Figure 2). While bolide impacts with environmental consequences are rare on a human timescale, they do occur, such as the Kaali impact event around 800 to 400 B.C. in present-day Estonia (Veski et al., 2001). Following the Kaali impact, farming, cultivation, and possibly human habitation in the region ceased for up to 100 years. Therefore, to prevent future catastrophic impacts on Earth, it is critical to study the strength and failure characteristics of NEOs through laboratory testing of meteorites, in addition to identifying new ones using advanced telescopes and deep space missions.

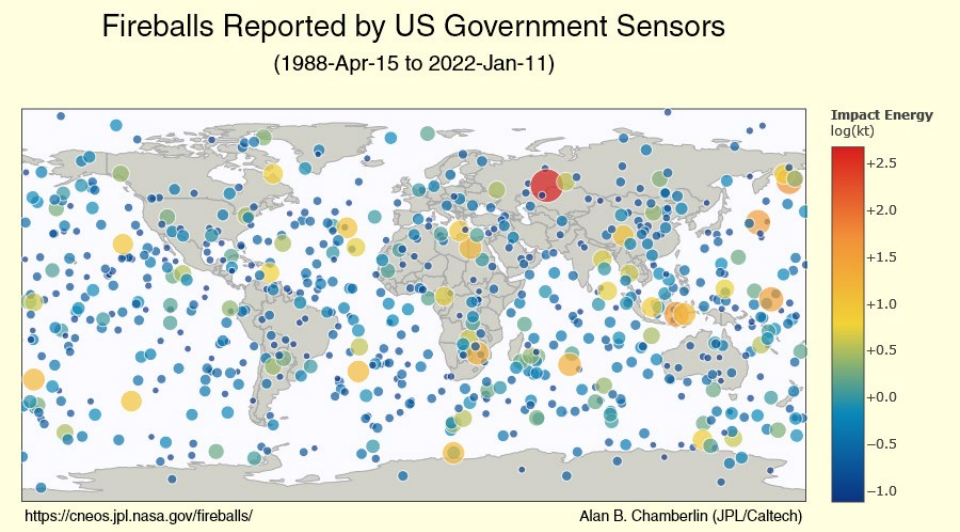

Figure 2. Atmospheric Fireball Events Corresponding to the Geographic Location Show Estimated Impact Energy for Each Event by Its Relative Size and Color. The Large Red Dot Corresponds to the 2013 Chelyabinsk Event over Southern Russia. Image Credit: NASA/JPL-Caltech.

NASA recently conducted the Double Asteroid Redirection Test (DART) mission, which was the first to demonstrate the principle of using a kinetic impactor to deflect an asteroid. DART impacted Dimorphos, the moonlet of the binary asteroid (65803) Didymos (Dotto et al., 2021). The change in momentum caused by the impactor was measured by ground-based telescopes, and its effect on the moonlet was studied to characterize the target's shape and conduct a scientific investigation using the LICIACube CubeSat (Cheng et al., 2023; Daly et al., 2023; Rivkin and Cheng, 2023; Thomas et al., 2023). As a result of the impact, Dimorphos' orbital period around Didymos was reduced by approximately 30 minutes, and the average distance between Dimorphos and Didymos also decreased. The significant change in the orbital period shows that the DART kinetic impact was successful in deflecting the asteroid Dimorphos. However, the calculation of post-impact momentum transfer and deflection efficacy varies from asteroid to asteroid, depending on the impact site characteristics. Thus, impact experiments with a high-fidelity model are necessary to develop a general strategy for impact deflection. Such deflection modeling requires laboratory measurements of meteorites' physical and mechanical properties, their scale dependence, and their relationship to the properties of parent asteroids.

1.2 Meteorites

Meteorites provide a window into understanding NEO compositions, structures, and properties. Although NEO populations refer to asteroids, comets, and precursor bodies of meteorites, objects that are in close vicinity to the Earth are presumed to have an asteroidal origin, and are known as near-Earth asteroids (NEAs). Meteoroids are small pieces of asteroids that result from collision events. When meteoroids enter the Earth's atmosphere at velocities

of about 15-20 km/s, the friction with the air causes them to decelerate. As a result, the surface temperature of the meteoroid rapidly increases to several thousand degrees Kelvin, leading to the luminous phenomena observed as meteors (Zanda and Rotaru, 2001). Smaller meteoroids in the millimeter size range are typically stopped in the upper atmosphere, resulting in brief meteors that do not persist for more than a fraction of a second. However, larger meteoroids with greater mass can penetrate deeper into the atmosphere, creating longer-lasting streaks of light before eventually vaporizing. The increased Ram pressure from air drag can cause a meteorite to break into several, sometimes thousands, fragments, significantly reducing their velocity (Perron and Zanda, 2005a). The fragments that survive this fiery passage through Earth's atmosphere are known as meteorites, ultimately reaching the ground with a velocity corresponding to free fall, typically ranging from one to a few hundred meters per second.

Chondrites are the most commonly recovered meteorites. Among the 1217 recovered meteorite falls, 84% are chondrites, which include 75% ordinary chondrites (32% H-, 37% L-, and 9% LL-group) and ~4% carbonaceous chondrites (Binzel et al., 2015) and a few rarer groups. Carbonaceous chondrites are thought to represent materials from C-type asteroids (containing carbonaceous materials such as carbon, hydrated minerals, and organic compounds) and S-type asteroids (dominated by anhydrous Fe-Mg-Al-Ca silicates). On the other hand, M-type asteroids represent a small portion of rare asteroid types that are thought to be dominated by Ni-rich iron, likely represented by iron meteorites (Nelson et al., 1993). In the early history of the solar system, the decay of short-lived radioactive nuclei provided the primary heat source to melt early planetesimals, which facilitated differentiation. During this differentiation process, the denser metallic iron and nickel sank to the center forming a metallic core surrounded by a less-dense silicate mantle (containing Na, Al, and Ca). This mantle can further differentiate into a basaltic crust and a denser silicate mantle.

Differentiated meteorites experienced major chemical and physical changes compared with the primitive meteorites, as they solidified from their molten state. This differentiation process is thought to be completed for large bodies such as Earth, Mars, and the moon, whereas it may not always be complete for smaller bodies (Perron and Zanda, 2005b). The undifferentiated, primitive meteorites, such as the carbonaceous chondrites reflect the composition of their parent material inherited from the solar nebula. Differentiated meteorites, represented by the achondrites, record the thermo-chemical process of planetesimal formation in the early solar system.

1.3 Chemical and Petrographic Characterization

The chemical, mineralogical, and petrographic properties of meteorites have received considerable attention (Khout, 2009; Norton, 2002; Rubin and Ma, 2021; Rubin, 1997; Sears, 2004). Reflectance spectroscopy of C-, S-, and M-type asteroids shows similarities to the carbonaceous chondrites, silicate-rich ordinary chondrites, and iron meteorites, respectively. However, it is difficult to find suitable spectral matches because asteroid surfaces are subjected to extended periods of space weathering, which changes their properties. Additionally, surfaces can be modified by impacts with other asteroidal materials. Alteration processes, such as aqueous alteration, thermal metamorphism, shock, and brecciation, may modify the chemical and mineralogical properties of meteorites, changing the mineralogy, structure, and physical properties of the original parent-body materials. For example, temperatures >0°C allow the reaction between water and other minerals, forming a complex mixture of clay minerals - a process known as aqueous alteration (Endress et al., 1996). Heat can cause significant chemical and structural changes in chondrites, equilibrating the silicate compositions and crystallizing the fine-grained matrix and chondrules. Although alteration by

water or temperature may have been completed, changes due to collision events - shock metamorphism - continue to occur.

More than 435 minerals have been identified in meteorites, reflecting a wide range of early Solar System environments (Rubin and Ma, 2021). The most abundant minerals in chondrites are olivine, pyroxene, plagioclase, and opaque phases containing metallic Fe-Ni, troilite, and chromite. Silicate minerals are major components in stony meteorites, while metals, primarily kamacite, and taenite, along with schreibersite, graphite, and cohenite, dominate iron meteorites. Stony meteorites are classified based on major element compositions, oxidation states, oxygen isotopic compositions, and petrology, while iron meteorites are classified based on chemical elements such as nickel, cobalt, gallium, germanium, and gold. The most characteristic feature of many iron meteorites is the Widmanstätten structure, which formed due to the intergrowth of two phases, kamacite, and taenite. These complex mineralogies and structures influence the physical properties of meteorites.

1.4 Physical Characterization

Physical properties such as density, porosity, elastic properties, and magnetic susceptibility provide information on asteroidal composition and breakup in impact events (Khout, 2009). A comparison of physical properties between meteorites and terrestrial basalt reveals that unweathered meteorites have higher porosity, suggesting that most stony meteorites are likely to be comparatively weaker (Flynn et al., 2018).

The measurement of porosity requires two different densities - grain and bulk density - along with their corresponding volumes. Grain density indicates the density of the material without pores, while bulk density considers the density of the material including the pores. Ordinary chondrites display a range of grain density from 3.25 to 3.80 g/cm3 (Britt and

Consolmagno, 2003; Consolmagno et al., 2008; Macke, 2010; Ostrowski and Bryson, 2019), with a trend of higher density for H, or high metal, and lower density for LL, or low metal, ordinary chondrites (Figure 3). Similarly, the carbonaceous chondrites that are dominated by anhydrous minerals, such as CV and CK chondrites, show a similar range in grain density. For example, CV, CO, CH, and CK meteorites have mean grain densities of 3.48±0.09 g/ cm3, 3.48±0.27 g/ cm3, 3.44 g/ cm3, and 3.47±0.02 g/ cm3, respectively (Britt and Consolmagno, 2003; Consolmagno et al., 2008). However, grain densities are lower in the hydrated carbonaceous chondrites, such as in CI, CM, and CR types. Britt and Consolmagno (2003) report mean grain densities of 2.26±0.08 g/ cm3, 2.71±0.11 g/ cm3, and 3.23±0.28 g/ cm3 for CI, CM, and CR meteorites, respectively. These lower densities indicate the presence of phyllosilicate minerals that have lower densities. For iron meteorites, the mean density is 7.51 ± 0.19 g/cm3, and this varies with the change in total nickel content, making it the densest meteorite among all categories (Macke, 2010).

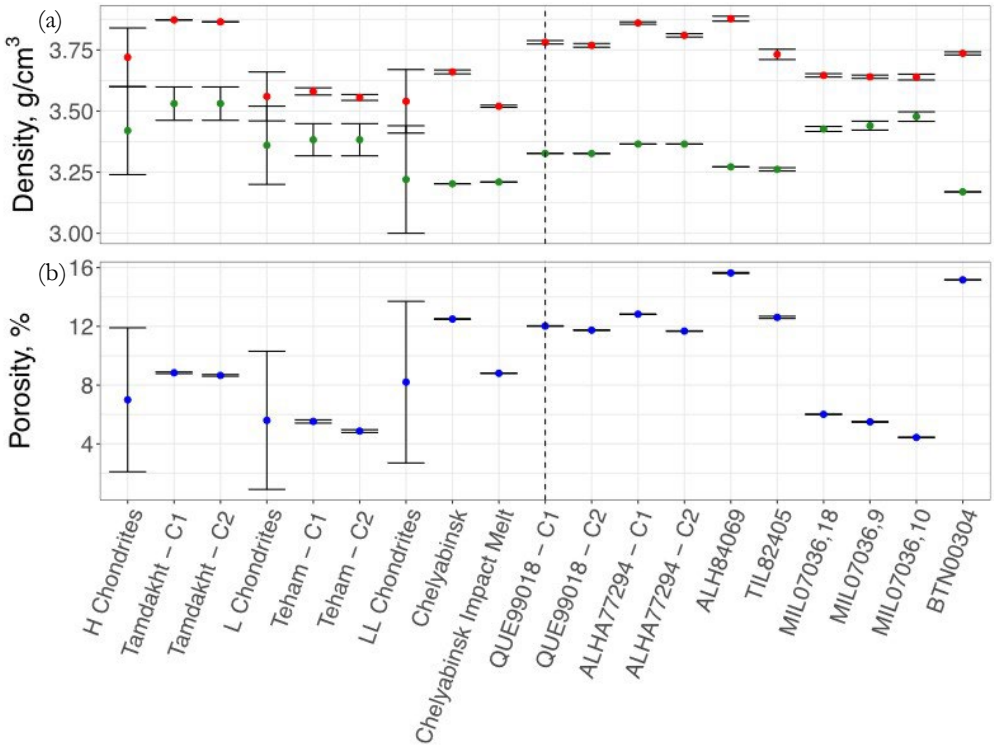

Figure 3. Physical Properties of H, L, and LL Ordinary Chondrites (Consolmagno et al., 2008) Exhibit Variations in (a) Bulk Density (Green) and Grain Density (Red), As Well as (b) Porosity. A Vertical Dashed Line Is Used to Distinguish Between Ordinary Chondrite Falls and Antarctic Ordinary Chondrites. Data From (Ostrowski and Bryson, 2020).

Weathering, thermal metamorphism, and shock significantly influence the density of meteorites. Weathering processes can lead to oxidation, causing a significant expansion in volume (Buddhue, 1957). This oxidation tends to increase the presence of less dense clay minerals, resulting in a decrease in the bulk density of the meteorite (Consolmagno S.J. et al., 1998, p. 19). Additionally, thermal metamorphism and shock events can alter the mineralogy of meteorites. FeNi metals can melt and flow into cracks and pore spaces, forming melt veins (Walker and Cameron, 2006). This process reduces the pore spaces and contributes to a

reduction in grain density. The combined effects of changes in bulk and grain density result in the wide range of porosity observed in meteorites.

Porosity refers to the measure of empty space within a material, which can exist in various sizes and shapes (Jones, 2009; Macke, 2010; Soini et al., 2020). It is a key characteristic that provides valuable insights into the formation processes, history, and alteration of materials over time. The presence and distribution of porosity can significantly influence the mechanical properties of materials, such as their ability to withstand impacts, and thermal conductivity (Bottke et al., 2002; Li et al., 2012; Opeil Sj et al., 2012). In the context of asteroids, porosity plays an important role in understanding their internal structure. A low macroporosity suggests a solid and cohesive body, while a high macroporosity indicates a rubble pile object held together by gravity (Richardson et al., 2002). Porosity also influences the atmospheric breakup of meteoroids by altering the heat transfer between the surrounding airstream and the meteoroid itself (ReVelle, 2001).

Porosity plays a crucial role in understanding the internal structure and composition of asteroids. By measuring the porosity and bulk density of meteorites, the porosity of asteroids can be estimated. Asteroids can exhibit both micro and macro porosity, with the measurement of microporosity being a challenging task. Macroporosity relies on the bulk density of meteorites and the grain density of asteroids. These parameters provide insights into the overall porosity of the asteroid. In the case of collision events, heavily impacted bodies are expected to have a moderate porosity, indicating a certain level of structural integrity. On the other hand, high-porosity objects suggest the presence of rubble piles, where the asteroid is held together by gravity rather than cohesive forces (Carry, 2012). Microporosity is of primary interest in meteorite studies. Three types of microporosity have been recognized, including crack porosity, cracks along the grain boundaries, and roughly spherical voids (Flynn et al.,

1999; Jones, 2009). The mean porosity of stony-iron meteorites is 0.0 ± 5.2%, and most ordinary chondrite porosity is within ~8.5%. The highest porosity of 34.9% is observed in carbonaceous CI1 chondrites (Macke, 2010). The porosity of meteorites is shown to correlate with other physical and mechanical properties, such as thermal conductivity, sound speed, elastic properties, strength, and response to mechanical (static and dynamic/impact) loads (Flynn et al., 2018).

1.5 Mechanical Characterization

Characterizing mechanical properties requires destructive tests. Conventional testing methods used to study terrestrial rock and concrete can be used to characterize the mechanical properties of ordinary and carbonaceous chondrites (Cotto-Figueroa et al., 2016; Pohl and Britt, 2020; Rabbi et al., 2021). These test methods require cylindrical-shaped samples for compression and indirect tension tests. However, the acquisition of suitably sized meteorites for lab testing poses a challenge. As a result, researchers utilize samples of various sizes and geometries in their studies. These include cubes (Cotto-Figueroa et al., 2016; Kimberley et al., 2011; Medvedev et al., 1985; Slyuta, 2010; Zotkin et al., 1987), cuboidal (Hogan et al., 2015), and cylindrical shapes (Tsuchiyama et al., 2009; Voropaev et al., 2017), due to the difficulty in acquiring suitably sized meteorites for lab testing. The shape of the samples varies from centimeter to micron-sized (Cotto-Figueroa et al., 2016; Tsuchiyama et al., 2009). Moreover, these tests have inherent challenges due to (1) difficulty in preparing experimental setup for lab tests, (2) lack of standard test specifications for meteorites, and (3) complexity due to anisotropic mechanical behavior resulting from distinct chemical compositions, heterogeneous microstructure, and the presence of cracks and shock veins, which lead to

complex failure characteristics. Furthermore, multiple samples from different types of meteorites are required to be tested to achieve reliability in their mechanical properties.

1.6 Macro-scale Characterization

The strength of meteorites, which refers to their response to external forces, can be evaluated through uniaxial quasi-static compression and tension experiments. However, laboratory measurement of meteorite strength is limited due to the difficulty in acquiring suitably sized meteorites, as they are inherently rare and expensive. This lack of available samples has resulted in relatively few published measurements, raising concerns about the statistical reliability of existing strength data (Pohl and Britt, 2020). In addition, significant variations in moduli and Poisson's ratio in conjunction with strength have been observed within ordinary and carbonaceous chondrites (Figure 4), which also exhibit spatial anisotropies in their mechanical properties due to their complex mineralogy and heterogeneous microstructures (Cotto-Figueroa et al., 2021, 2016; Flynn et al., 2018; Ostrowski and Bryson, 2019; Rabbi et al., 2021).

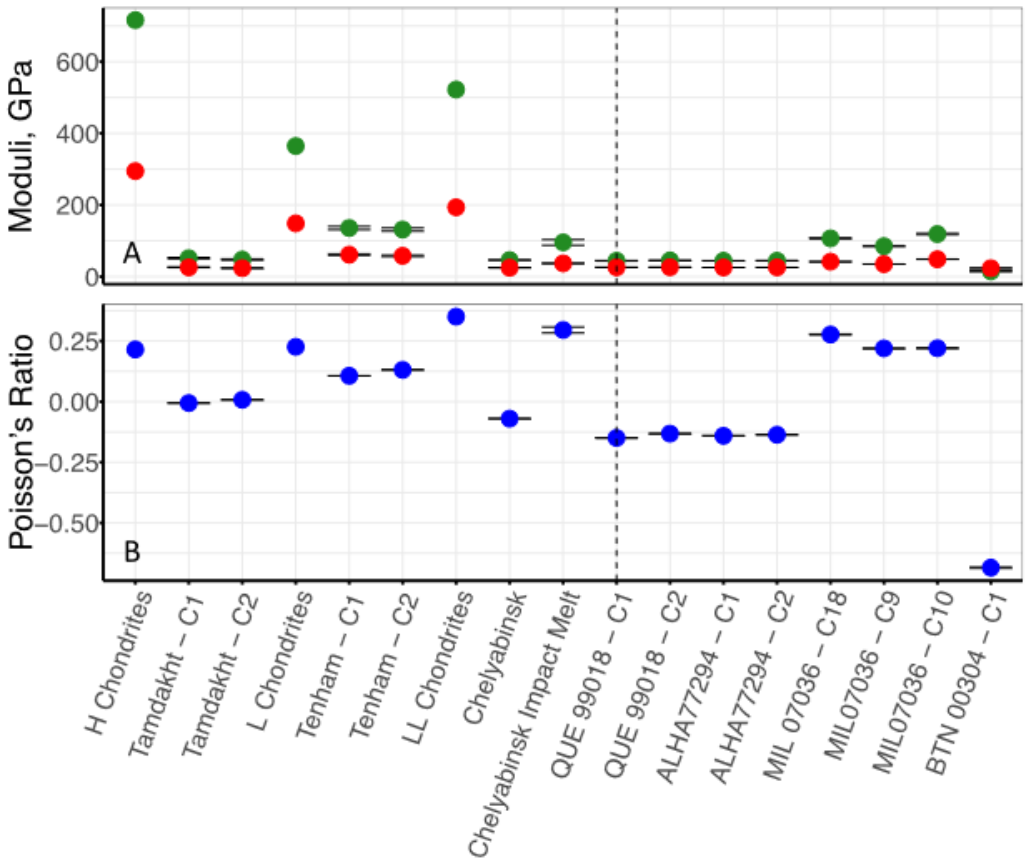

Figure 4. Elastic Properties of H, L, and LL Ordinary Chondrites Show Variations In (a) Elastic Modulus (Green) and Shear Modulus (Red) and (b) Poisson's Ratio, Which Is Estimated From the Elastic Wave Measurements. Data From (Ostrowski and Bryson, 2020).

A limited number of studies have reported the compressive strength of OCs, ranging from 30 – 700 MPa (Flynn et al., 2018; Ostrowski and Bryson, 2020, 2019; Pohl and Britt, 2020), with notable variations observed within individual meteorites. For example, a compression experiment conducted on ten 1-cm Aba Panu (L3) cubes revealed a failure strength range of 361.7 to 578.0 MPa (Rabbi et al., 2021). Similarly, the compression tests on seven 1-cm Viñales (L6) cubes resulted in a range of 110.5 to 187.8 MPa (Cotto-Figueroa et al., 2021; Rabbi et al., 2023), while Tamdakht (H5) exhibited a range of 76 to 247.4 MPa (Cotto-Figueroa et al.,

2016). The average compressive strength for H chondrites and L chondrites has been measured as 191.7±85.2 MPa and 171±133 MPa, respectively (Ostrowski and Bryson, 2019). It is evident from the data, particularly the measurements obtained from multiple samples of Aba Panu (L3) (Rabbi et al., 2021), that individual meteorites can deviate significantly from the current mean values.

When comparing the strength of different classes of meteorites, it has been found that iron meteorites display a higher mean strength due to their metallic compositions. They also exhibit plastic deformation under external forces (Gordon, 1970; Johnson and Remo, 1974; Rabbi et al., 2022; Remo and Johnson, 1975), unlike most ordinary and carbonaceous chondrites which undergo brittle failure due to their predominance of brittle silicates with preexisting cracks (Cotto-Figueroa et al., 2016; Hogan et al., 2015; Rabbi et al., 2021; Rabbi et al., 2021). These variations in strength and deformation behavior can have important implications for the interpretation of meteorite impact events and the dynamics of meteoroid entry into the Earth's atmosphere.

1.7 In-situ Digital Image Correlation

Characterizing meteorite failure requires an understanding of local and global deformation, which can be achieved using the noncontact full-field (3-D) Digital Image Correlation (DIC) technique during real-time experiments (Chu et al., 1985; Pan, 2011; Pan et al., 2009). DIC provides 3-D full-field deformation, which can be used to determine mechanical properties such as elastic modulus, Poisson's ratio, and anisotropy coefficient in the transverse direction while analyzing the digital images recorded before and after the mechanical tests (Farahani et al., 2020; Rabbi et al., 2021). The DIC technique is also effective in determining fracture characteristics: crack opening displacement (COD), crack extension, crack kinematics, and

identifying crack initiation, crack location, and propagation from the strain localization contours (Gehri et al., 2020; Miao et al., 2020; Pan, 2011). The DIC technique offers significant advantages in the study of limited numbers of meteorite samples. It enables the investigation of meteorite response to various external forces, including static and dynamic loading. This capability facilitates the exploration of potential relationships between the mechanical response of materials, structural characteristics, and defects (Abdulqader and Rizos, 2020).

1.8 Microscale Characterization

The use of the DIC technique allows us to gain valuable insights into the deformation behavior of a target surface, enabling a deeper understanding of how failure initiates and propagates at the macroscale. However, this technique is limited to investigating the underlying causes and dominant material internal characteristics that contribute to the failure mechanism. To obtain a comprehensive understanding of the failure mechanism, it is essential to complement DIC analysis with other techniques such as X-ray computed tomography (X-CT). X-CT is a three-dimensional non-destructive technique that has been applied in meteorite studies to reveal the internal structure, texture, and distribution of distinct phases in chondrites (Ebel and Rivers, 2007), pore spaces (Sasso et al., 2009), and chondrule sizes (Friedrich et al., 2008). The X-CT technique can detect microstructural characteristics such as cracks, voids, and heterogeneity in microstructures that can be difficult to identify by thin section analysis or ultrasonic measurements, (Vaneghi et al., 2021). Moreover, the X-CT method provides 3D data of the internal structure, including size, shape, and morphology of various phases, inclusions, and distributions of pores (Carlson et al., 2003; Dionnet et al., 2020b; Mees et al., 2003; Riad et al., 2014). Hence, it can be useful for the development of high-fidelity models to

investigate the influence of internal structure and defects on failure initiation and strength properties (Dionnet et al., 2020a; Kalasová et al., 2020; Liang et al., 2020).

Meteorite strength and elastic properties provide valuable information about the survivability of a meteor during its passage through the Earth's atmosphere, as well as key insights into the development of strategies to deflect potential near-Earth objects. A correlative study of local mechanical properties of heterogeneous multiphase structures using nanoindentation in combination with X-CT and analytical techniques, such as energy-dispersive X-ray spectroscopy (EDX), can be used to understand the multiscale physical and mechanical properties of meteorites, and by extension understand the properties of NEOs (Moyano-Cambero et al., 2017; Wheeler, 2021). Nanoindentation can produce a feature map of micromechanical properties, such as hardness, elastic modulus, and fracture toughness, of the minerals forming the meteorite, which can help infer the strength and response of a large bolide during an impact event (Moyano-Cambero et al., 2017; Wheeler, 2021). By combining multiple techniques and approaches, we can obtain a more holistic view of the strength and failure mechanism, incorporating both surface observations and internal material characteristics.

1.9 Strength and Failure Characterization

Bolides and asteroids composed of materials similar to meteorites are in general weaker than meter- to centimeter-sized meteorites (Cotto-Figueroa et al., 2016). A combined study is necessary to assess the strength of bolides and asteroids using the airburst data (Holsapple, 2009) and the laboratory measurements of meteorites designed to understand their strength and fragmentation. Studies on asteroid disruption and fragmentation modeling (Benz and Asphaug, 1999) have typically used terrestrial analogs such as basalt, granite, or even lunar

rocks (Durda et al., 2011). However, the reason for their material bias in mechanical properties remains unexplained. To date, the majority of the physical properties are obtained from non-destructive tests, such as bulk density and porosity (Consolmagno et al., 2008; Flynn et al., 2018; Jones, 2009; Macke, 2010; Molesky et al., 2015; Wilkison et al., 2003), thermal conductivity (Opeil et al., 2010), remnant magnetism (Weiss et al., 2002), textural and tomography studies (Ebel and Rivers, 2007; Sasso et al., 2009), and a few disruptive studies on ordinary chondrites and iron meteorites (Durda et al., 2011; Flynn, 2006; Flynn and Durda, 2004; Kimberley and Ramesh, 2011; Marchi et al., 2020). Although limited static and dynamic fracture properties (Flynn and Durda, 2004; Kimberley and Ramesh, 2011; Marchi et al., 2020), elastic constants, and sound speed measurements (Ibrahim and Hildebrand, 2012) have been reported on a few meteorites, rheological properties related to their failure and their scale-dependency have not been obtained for ordinary chondrites and iron meteorites.

1.10 Scale Dependent Strength

Laboratory measurements of the physical and mechanical properties of meteorites provide insight into the strength and fragmentation behavior of asteroids, allowing for the estimation of strength across a range of sizes, from centimeters to tens of meters, using a Weibull statistical approach (Cotto-Figueroa et al., 2021, 2016; Holsapple, 2009; Pohl and Britt, 2020). The link between statistical models for brittle or ductile fracture is derived by considering the difference in the ideal and actual response of the material under different load conditions (Tiryakioğlu, 2015). These variations in mechanical response can be attributed to preexisting cracks that initiate failure for brittle materials (Griffith and Taylor, 1921; Hogan et al., 2015; Rabbi et al., 2021; Ramesh et al., 2015) or pores and cracks in ductile materials (Knott, 1997; Thomason, 1990). Statistical distribution of strength and other fracture properties, such as

elongation and toughness, depend on the distribution of defect sizes; in other words, high-stress concentration occurs around the largest defect, which can then lead to failure (Epstein, 1948). This can be represented as an empirical relation between the cumulative probability of failure and failure strength, known as the Weibull distribution (Weibull, 1951), which has been applied in asteroid disruption models (Benz and Asphaug, 1999; Housen, 1999; Melosh et al., 1992).

While Weibull analysis allows for the derivation of the failure-related mechanical properties of asteroids from the laboratory measurements of meteorites, there is a need to characterize the mechanical properties of both stony and iron meteorites and to establish a relation for understanding the bulk physical and mechanical properties of NEOs. This effort to bridge the gap in knowledge of fracture-related mechanical properties between meteorites and asteroids will support future engineering studies and aid in developing strategies for NEO hazard mitigation, sample return, and human exploration.

1.11 Objectives of the Work

The primary objectives of this research are as follows:

1. Develop a comprehensive understanding of the bulk chemical, physical, and mechanical properties of chondritic and iron meteorites, and extrapolate this knowledge to gain insights into the properties of NEOs with similar compositions.
2. Determine the mineralogy of chondritic and iron meteorites by utilizing an electron microprobe analyzer equipped with wavelength dispersive spectroscopy and electron dispersive spectroscopy. Investigate how compositional variations in minerals affect strength and fracture behavior.

3. Characterize the fracture-related mechanical properties of meteorites, including failure strength, failure mode, and fracture behavior, under static load conditions for both chondritic and iron meteorites.
4. Investigate the influence of the complex microstructure of chondritic and iron meteorites, including preexisting defects such as porosity, pore-size distribution, voids, and microcracks, on failure mechanisms.
5. Analyze the distribution of metals and their structural characteristics in chondritic meteorites using X-ray micro-computed tomography. Examine how these factors influence failure initiation and propagation.
6. Develop low-temperature testing techniques for iron meteorites to investigate the in-situ deformation of their microstructure under tensile loads. Compare and contrast the failure mechanisms observed at ambient and low temperatures.

1.12 Outline

This dissertation is structured as follows:

Chapter 2 focuses on investigating the mechanical strength and failure mechanism of the Aba Panu (L3) ordinary chondrite. The chapter utilizes the 3-D DIC technique to perform non-contact full-field deformation and strain measurements during in-situ uniaxial quasi-static compression testing. Additionally, a numerical approach is employed to model the multiphase minerals present in this meteorite using commercially available software, Abaqus. A phenomenological model is also developed to study the phenomenon of initial crack closure observed in the mechanical response of Aba Panu. Lastly, the chapter analyzes fragments of the crushed samples to investigate the surface roughness and discusses its implications.

Chapter 3 provides an analysis of the mineralogical, physical, and mechanical properties of the Viñales (L6) ordinary chondrite. The focus is on investigating the deformation and failure behavior of the meteorite using in-situ 3-D DIC and X-CT techniques under quasi-static compression loading conditions. Furthermore, the chapter examines the influence of shock-melt veins and the presence of Fe-Ni on the mechanical response and failure mechanism of the Viñales meteorite. These features are studied in detail to understand their role in the overall behavior and structural integrity of the meteorite.

Chapter 4 presents a study on the microstructure of the Gibeon (IVA) iron meteorite using the electron microprobe analyzer. The chapter analyzes the deformation mechanism of the meteorite under compressive and tensile loading conditions at ambient temperature. It further investigates the primary minerals of the iron meteorite, namely kamacite, and taenite, and their deformation behavior. Additionally, the chapter includes in-situ low-temperature tensile testing of the iron meteorite to examine the influence of microstructure on its mechanical properties.

Chapter 5 summarizes the research contributions and discusses the limitations and challenges encountered during the investigation of stony ordinary chondrites and iron meteorites. Additionally, the chapter offers suggestions for future research, emphasizing the need to address the complex heterogeneous microstructure and variations in strength to develop physics-based models for ordinary chondrites.

CHAPTER 2

UNDERSTANDING ASTEROIDAL FAILURE THROUGH QUASI-STATIC COMPRESSION TESTING AND 3-D DIGITAL IMAGE CORRELATION OF THE ABA PANU (L3) CHONDRITE

2.1 Introduction

Understanding the physical nature of asteroids requires a thorough investigation of the physical and chemical properties of meteorites as most are fragments of asteroids. The mechanical strength of meteorites provides insights into the processes of atmospheric breakup and fragmentation (Foschini, 2001; Svetsov et al., 1995). The meteorites that survive atmospheric entry, ablation, and breakup are some of the strongest known materials as they survived ejection from their parent bodies, endured long periods in space, entered through Earth's atmosphere, and impacted and resided on Earth's surface (Melosh, 1984).

The strength of asteroids can be estimated from fireball data or laboratory analyses of meteorites (Popova et al., 2011). Asteroidal atmospheric flight and fragmentation measurements are used to estimate bulk strength in the meter-size range of pre-impact meteoroids. These strengths are typically weaker at the macro-scale when compared with the strengths of meteorites measured in the laboratory (Cotto-Figueroa et al., 2016; Flynn et al., 2018; Ostrowski and Bryson, 2019). Compression tests can be used to determine the strength of meteorites: these tests mimic the compressive loads experienced by asteroids during their passage through the atmosphere. Quasi-static compressive strength measurements have been performed on samples of various sizes, shapes, and geometries (Cotto-Figueroa et al., 2019, 2016; Hogan et al., 2015; Kimberley and Ramesh, 2011; Medvedev et al., 1985; Slyuta, 2010; Tsuchiyama et al., 2009;

Voropaev et al., 2017; Zotkin et al., 1987). The reported failure strengths vary with different scales of measurement and with the number and size of defects in the samples (Popova et al., 2011; Slyuta, 2017). In addition, complexity arises when analyzing meteorites as they exhibit a range of mechanical properties at a range of length scales. This variation occurs since meteorites were subjected to thermal and aqueous alteration, experienced shock at different degrees, or was affected by terrestrial weathering (Flynn et al., 2018).

Laboratory measurement of meteorite strength can help to predict and establish relations among centimeters to tens-of-cm-meter-sized meteorites to similar asteroidal bodies. Cotto-Figueroa et al. (2016) measured the strength properties of the Allende (CV3) and Tamdakht (H5) meteorites and determined their Weibull failure distribution. Their data, which was in accordance with the fireball data of the same type, shows that centimeter-sized meteorites are stronger than meter-sized boulders of similar composition. Hence, measurements of similar strength properties are necessary to predict the survivability of meteors during entry, and their effects upon impact, and are important for asteroid disruption models (Ostrowski and Bryson, 2019). Since the direct in situ strength measurements of asteroids are challenging, the laboratory characterization of meteorites provides a viable means to understand their strength behavior.

Understanding the strength and failure mechanisms of asteroids determined from laboratory measurements of meteorites can be enhanced using in-situ techniques that enable the measurement of spatially resolved local strains. The full-field, three-dimensional (3-D) digital image correlation (DIC) technique acquired during quasi-static compression testing can be used to analyze deformation behavior. DIC is a non-contact technique that compares high-spatial-resolution images acquired before, during, and after deformation, and provides the full-field in- and out-of-plane deformation fields (Chu et al., 1985). DIC allows the deformation distribution

on the target surface to be determined by measuring the strain field (Pan et al., 2009). This non-contact technique allows measurement of the full-field deformation and strain (point-by-point strain field). In contrast, standard methods such as uniaxial extensometers are designed based on the assumption of uniformity of deformation and can only measure the average strain within the gauge length. The DIC can also capture complex strain localization patterns and material behavior under any loading condition, a feature that is not available through conventional strain measurement techniques (Farahani et al., 2020; Gehri et al., 2020; Pan, 2011).

Furthermore, the study of internal microstructure and micromechanical strength properties of the constituent elements provides the necessary information to understand the multiscale mechanical response and failure behavior of meteorites. 3D non-destructive X-ray computed tomography (X-CT) is beneficial for investigating preexisting defects such as cracks and voids (Vaneghi et al., 2021), texture and distribution of various phases in chondrites (Ebel and Rivers, 2007), pore spaces (Sasso et al., 2009), and chondrule sizes (Friedrich et al., 2008). In conjunction, the local mechanical properties of these phases can be examined using nanoindentation (Brusnitsina et al., 2019; Wheeler, 2021). While a wide range of physical and mechanical properties of meteorites are available, including from disruptive experiments (Kimberley and Ramesh, 2011; Pohl and Britt, 2020), it is important to investigate the failure of meteorites in more depth, which can be achieved through a correlative study of full-field 3D DIC, X-CT, and nanoindentation.

This chapter presents the quasi-static response and failure analysis of the Aba Panu meteorite, an L3 ordinary chondrite fall. This meteorite was chosen because it represents the most common type of asteroidal body to produce meteorites - the ordinary chondrites. Therefore, it has direct applications for understanding hazard mitigation strategies for similar asteroidal bodies. This

study provides insights into the failure mechanism of Aba Panu under quasi-static compression tests, accompanied by the analysis of the full-field strain distribution using DIC. Mechanical properties were determined from both ultrasonic measurements and the stress-strain response, and the failure of Aba Panu was studied through localized responses due to microstructure by examining displacement and strain contour maps of the meteorite sample. Furthermore, a correlative study using X-CT and nanoindentation was performed to understand the effect of the microstructure and local mechanical properties on the bulk mechanical response. Quantitative and qualitative analysis of the deformed sample was conducted to evaluate the failure mechanisms. This study also attempts to explain the brittle failure mode using DIC, accompanied by the analysis of stress and strain response under quasi-static compression loading. Furthermore, a microstructure-based representative volume element (RVE) was developed to simulate the response of Aba Panu using the commercially available finite element package, Abaqus. Finally, the strain fields are compared with DIC results to verify the mechanical response.

2.2 Material and Methods

2.2.1 Material

A 1269 g complete Aba Panu stone was acquired for this study. The stone was cut in half (Figure 5), and one half was further cut into 10 one-centimeter cubes. The surface of the cut stone shows a largely uniform distribution of chondrules, Fe-Ni metal, and sulfides (Figure 5). Most of the stone is dominated by light-colored, well-developed chondrules and chondrule fragments separated by a thin dark matrix. The chondrules range from 50 to 2500 μm, with a mean of 710±397 μm (n=100), and one outlier at 4.2 mm. The chondrules are visible in the optical images (Figure 5 and Figure 6) as light green to grey rounded to angular fragments.

The surface also showed three anhedral clasts (Figure 5 c1 to c3) that were petrographically distinct from the bulk.

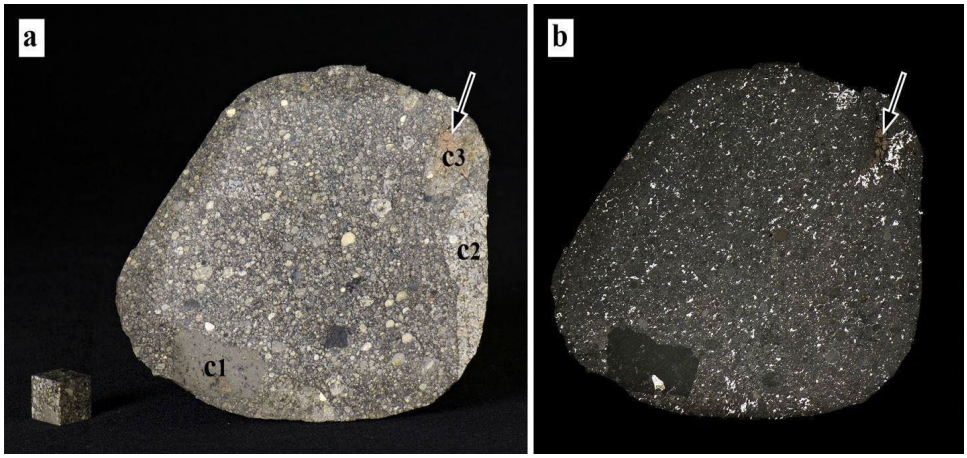

Figure 5. Photographs of the Cut and Polished Surface of the 1269 g Aba Panu Stone. (a) Photo Taken with the Light Angled to Clearly Show the Distribution of Chondrules, and Clasts C1 to C3. Arrow Points to a Large Troilite Region. A 1-cm Aba Panu Cube Is Shown for Scale. (b) Photograph of the Same Surface as in (a) but with the Light Incident Normal to the Meteorite Surface. The Fe-Ni Metal and Troilite Are Reflective and Bright.

These clasts were not sampled during the physical property measurements and the 1-cm cubes were cut from the average L3 lithology. The opaque mineralogy is dominated by Fe-Ni metal and troilite (Figure 7). Fe-Ni metal occurs in several mineralogical forms and petrographies: a) Rare mm- to –cm grains, e.g., clast C3 in Figure 5, and the 2-mm troilite with enveloping kamacite in Figure 6; b) Anhedral grains 50 to 200 μm with holly-leaf-shaped outlines dominated by kamacite, and rounded 20 to 50 μm -sized Ni-rich grains of taenite; c) 20 to 50 μm -sized grains of taenite scattered throughout the matrix and as rims around chondrules; and, d) Pervasive fine-grained micron and submicron-spheres of Fe-Ni metal and troilite, and crack filling troilite within the matrix between the chondrules. This distribution is

revealed in the Fe, S, Fe without S, and Ni x-ray element maps (Figure 6), and in the high-resolution BSE images (Figure 7).

Mineral phases and compositions were determined using the field-emission electron microprobe analyzer (EMPA, JEOL JXA-8530F Hyperprobe) equipped with both wavelength-dispersive spectrometer (WDS) and energy-dispersive spectrometer (EDS). WDS-EDS data were acquired with an accelerating voltage of 15 kV and a current of 14.92 nA. The Java-based image processing software, ImageJ (Schneider et al., 2012), and Photoshop CS were used to process the x-ray elements maps and to quantify mineral sizes and areal densities. The areal percentages of the different components (Table 1) reveal the distribution of the major and minor components. As expected for an ordinary chondrite, silicates, measured by the Si K map, dominate and cover 91 areal%, whereas light-colored silicates measured from the optical image (Figure 6a) cover 75 areal%. The 16 areal% difference between the two measurements primarily represents the sum of dark-colored silicates in the matrix and opaques, dominantly Fe-Ni metal and troilite. Opaques constitute 8.8 areal%, though the area in Figure 6a contains a rare metal/troilite nugget, without which the totals are 5.1 areal%. For comparison, the reflective phases of the whole face are shown in Figure 5b, excluding the two clasts C1 and C3, which constitute 4.8 areal%, which is a similar measurement of the cube face in Figure 6a. The two accessory minerals, chromite, and Ca-phosphates are widely distributed but sparse in ordinary chondrites. Chromium is largely present at high concentrations in chromite, constituting 0.3 areal%, and P in Ca-phosphates covering 0.2 areal%. The distribution of different elements is a result of thermal metamorphism and causes complex texture and provides clues on their parent asteroid body formation and overall response to failure.

2.2.2 Ultrasonic Measurements

Sound wave velocities were measured using an Olympus 5077 PR ultrasonic pulse generator/receiver. A square wave pulse was applied to the ultrasonic transducer, which generated short ultrasonic pulses. A pair of 5 MHz full-contact transmission longitudinal ultrasonic transducers (V-110 RM, Olympus NDT) and a normal incidence shear wave transducer (V-156RM, Olympus NDT) were used as ultrasonic pulse sensors/actuators. The ultrasonic pulses were then amplified, and bandpass filtering was applied to minimize the scattered noise from the receiving signals.

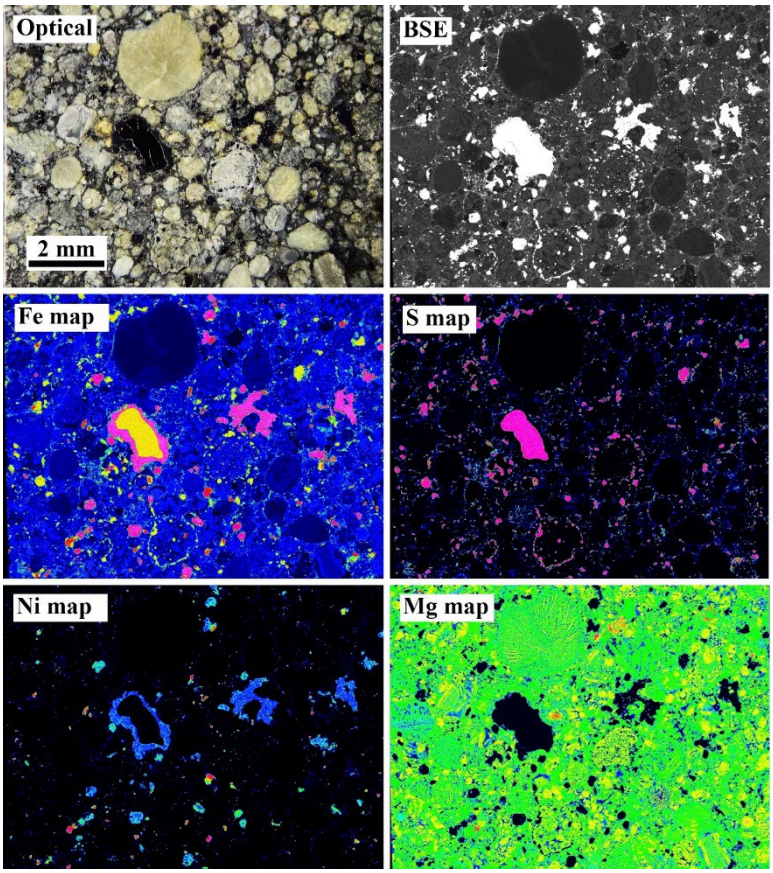

Figure 6. Optical Photograph, Back-scattered Electron (BSE) Image, and X-ray Maps (Fe, S, Ni, and Mg) from a Representative 1-cm Aba Panu Cube. The Optical Image Shows the

Distribution of the Light-colored Chondrules Separated by a Dark Matrix. The Distribution of High-Z Phases (Primarily Fe-Ni Metal and Troilite) Shows Bright White in the BSE Image. The Fe and S Maps Show the Location of the Troilite (Yellow in the Fe Map and Pink in the S Map) and Low-Ni Kamacite (Pink in the Fe Map). The "Fe and S Map" Shows the Distribution of the Kamacite and Taenite Grains. Nickel (Ni Map) Is Distributed Primarily in the Kamacite (Blue), with Rarer Grains of Taenite (Red to Green).

A shear wave couplant was used to reduce the acoustic impedance mismatch between the air and solid faces of the transducer and meteorite surface. Data were acquired from all three planes for each cube. Continuous signal data acquisition was accomplished using the National Instrument PXI 1042 hardware with a NI-Scope and an interchangeable virtual instrument. The data was further analyzed to estimate the time of arrival and the longitudinal (V_L) and shear (V_S) wave velocities in MATLAB. Sound wave velocities (VS and VL) were used to derive the elastic (E) and shear (G) moduli of the meteorite as shown in the following equations e.g., (Hu and Wang, 2016).

$$\nu = \frac{1 - 2\left(\frac{V_S}{V_L}\right)^2}{2 - 2\left(\frac{V_S}{V_L}\right)^2} \tag{2.1}$$

$$E = \frac{V_L^2 \rho (1+\nu)(1-2\nu)}{1-\nu} \tag{2.2}$$

$$G = {V_S}^2 \rho = \frac{E}{2(1+\nu)} \tag{2.3}$$

where ρ is the density, and ν is the Poisson's ratio. The E and G measurements from sound wave velocities indicate the directional heterogeneity and variation in compressive strength of meteorites related to their density and porosity/cracks density.

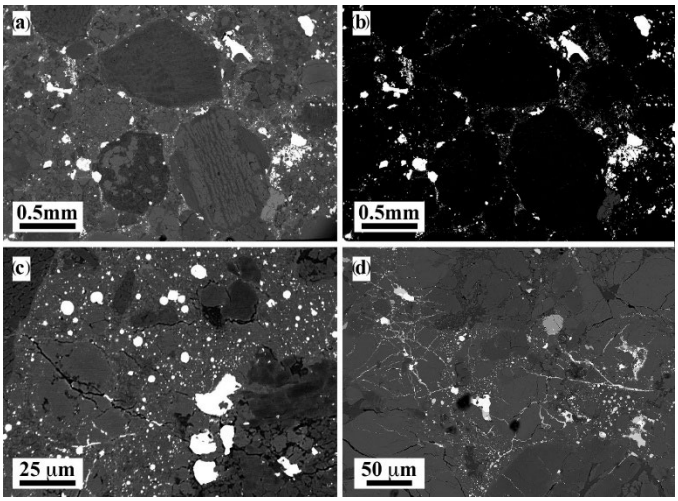

Figure 7. Backscattered Electron Images of Aba Panu. a) and b) of the Same Region Showing a Range of Chondrule Types Surrounded by Metal and Sulfide (White). In b) the Contrast Has Been Adjusted so That the Silicates Appear Dark and More Clearly Show the Metal and Sulfide Between the Chondrules. c) and d) Higher Magnification Image of a Matrix Region Between Large Chondrules. The Matrix Is Dominated by Silicate Fragments and an Abundance of Micron and Submicron-sized Spheres of Fe-Ni Metal and Troilite.

Table 1. Areal % of Selected Minerals and Elements Across the Aba Panu Cube Face as Shown in Fig. 4 Determined by X-ray Mapping with WDS and by Optical Measurements.

Mineral/element	Areal %
Si (Kα X-ray map)	91
Chondrules/fragments optical	75
Matrix (silicate+opaque)	16

Silicate matrix	7.2
Opaque – metal+sulfide	8.8 (5.1)*
Fe-Ni metal (Kα X-ray map)	4.8 (2.0)*
FeS (Kα X-ray map)*	4.0 (3.1)*
Al Kα X-ray map	13.5
Cr Kα X-ray map	0.3
P Kα X-ray map	0.2

* number in brackets is the areal% without the large metal/troilite nugget.

2.2.3 Porosity and Pore Size Distribution

Three small pieces of Aba Panu with irregular geometry were selected for testing in a nitrogen absorption porosimeter to determine pore size and distribution. The specific surface area of pores was measured using the Brunauer Emmett and Teller (BET) technique, and the pore size distribution was calculated by the Barrett-Joyner-Halenda (BJH) method (Bardestani et al., 2019) at 77 K using a Micrometrics Tristar II 3020 surface area and porosity analyzer. Furthermore, the porosity of the 1 cm cubes was calculated from bulk and grain density measurements. The bulk volume of each cube was also measured using digital calipers to estimate bulk densities. An Ultrapyc 1200e N_2 gas pycnometer was used to determine the grain densities, which was calibrated with the calibration spheres for each test to ensure repeatability. Using the average bulk and grain density, the total porosity was computed using Eq. (2.4).

$$P = \left(1 - \frac{\rho_b}{\rho_g}\right) * 100\% \tag{2.4}$$

where bulk density $\rho_b = \frac{M_m}{v_b}$ (where M_m is the mass of the meteorite) and grain density $\rho_g = \frac{M_m}{v_g}$

2.2.4 Quasi-static Uniaxial Compression Tests

The strength and mechanical response of the Aba Panu cubes were measured using the Universal Testing Machine Instron 5985 frame, equipped with a 250 kN load cell and compression fixtures of 145 mm diameter radial platen, with a maximum rated load capacity of 100 kN. The load cell was calibrated by Instron to ensure the accuracy and repeatability of the measurements. The tests were conducted in a displacement control mode at 0.25 mm/min or 4.2e-4 /sec strain rate at ambient temperature. The ASTM D7012 test standard was modified for the cubes to perform the quasi-static compression test (Figure 8). The ASTM standard explains the details of the testing procedure for the compressive strength and elastic moduli of the intact rock core, wherein specimens are designed according to ASTM standard D4543. It is suggested that the specimens have a cylindrical design to avoid edge effects. However, cubes were utilized due to our objective of implementing the DIC measurements where conformity in their dimension and shape are maintained as recommended by the ASTM D4543 standard. The surfaces of the meteorite that were in contact with the compression platens were lubricated using all-temperature silicone oil to avoid friction effects and bulging during compression and to maintain a uniaxial compressive state of stress during testing. Despite these measures, five samples showed an experimental artifact related to stress concentration due to sharp edges leading to premature failure from the sample edges or corners. Failure initiation and propagation on two samples were unable to identify from the

DIC measurements as they occurred in the non-speckle sides of the tested specimens. These samples were excluded from the analysis of the failure mechanisms.

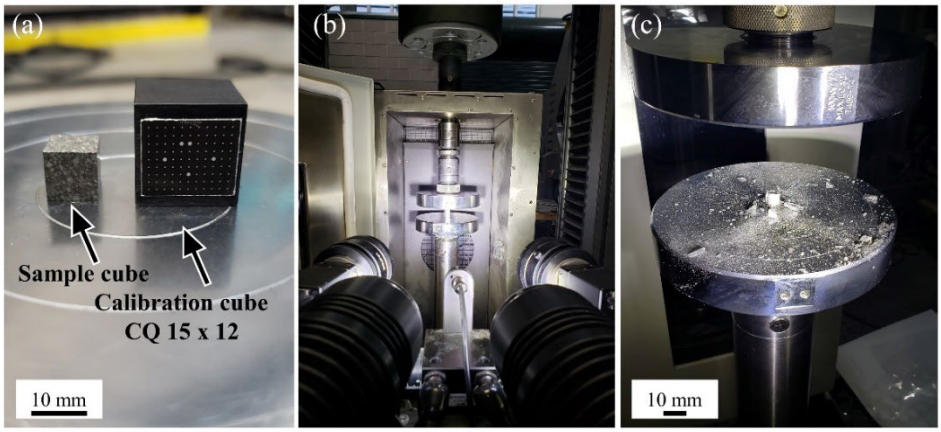

Figure 8. Experimental Setup for the Uniaxial Compression Testing. (a) Cube for Testing and DIC Calibration Cube, (b) Compression Testing Lab Setup with the Full-field 3D DIC, and (c) Remains of the Cube after Failure.

2.2.5 Three Dimensional (3D) Digital Image Correlation (DIC)

The in-situ displacement and strain field evolution on the surface of the cubes were measured using an ARAMIS 5M 3D DIC system and calibrated using the cubic calibration panel CQ15x12 (Figure 8a). Samples for DIC were prepared in two steps. One face of each cube is first sprayed with white paint to create a base and then a stochastic speckle pattern is created using black paint. This stochastic pattern allows tracking of the surface deformation during loading. Constant lighting was maintained using two LED light sources. Two 2448x2050 pixel stereo cameras equipped with CCD image sensors of 50 mm focal length were used to capture images at 1 frame per second (Figure 8b), similar to previous testing on Allende (CV3) and Tamdakht (H5) (Cotto-Figueroa et al., 2016). The distance and orientation of the cameras, along with image characteristics (e.g., focus and lens distortion), were

optimized during the calibration process. This allowed for maintaining the dimensional consistency of the measurement system, with the help of a calibration object. During calibration, intersection deviation was kept to a minimum, ~0.044 for correlation between the reference facets and target facets. Subsequently, computations were undertaken by selecting a region of interest, defined as a computation mask, and by generating a start point. The ARAMIS DIC software uses a small square image detail called a facet with the following specifications: facet size 15 x 15 pixels with a facet step of 13 pixels corresponding to a 2-pixel overlapping area. A robust correlation coefficient, zero-normalized cross-correlation – ZNCC was used (default by ARAMIS software) as correlation criteria to analyze the images. ARAMIS then computes the deformation by identifying the coordinate of the facet, as well as through the stochastic spray patterns (from the right and left cameras) of the undeformed and deformed images. Post-processing of the images in DIC software generates the displacement and strain field in the x-, y-, and z-direction. It computes an orthogonal rotation matrix and stretch tensor from the Cauchy strain tensor. Stretch ratios, the eigenvalues of the stretch tensors, are used to calculate the major (φ_1) and minor strains (φ_2). The third principal strain (φ_3) can be calculated from the major and minor strains considering the volume consistency. Equivalent von Mises strain is then, calculated from the strain tensor components using the following formula (GOM, 2013):

$$\varphi_{eq} = \sqrt{\frac{2}{3}(\varphi_1^2 + \varphi_2^2 + \varphi_3^2)} \tag{2.5}$$

2.2.6 X-ray Computed Tomography and Nanoindentation

The 3D X-ray computed tomography technique was applied to characterize the internal microstructure, determine the distribution and morphology of inclusions, and identify

preexisting cracks in the cubes. Tomography scans were performed at 140 kV with a low energy filter and an exposure time of 4 s using a lab-scale X-ray CT system (Zeiss Xradia 520 Versa, Carl Zeiss XRM, Pleasanton, CA, USA). A total of 3201 projections were obtained with a voxel size of 7.9 μm. The 3D reconstruction of all transmission scans was achieved using a commercial software package (Zeiss XMReconstructor).

A correlative study was performed by nanoindentation in conjunction with the X-CT technique to determine local micromechanical properties, such as reduced elastic modulus and hardness, of Aba Panu meteorite samples corresponding to different mineral phases. A commercial nanoindenter XP system (MTS, Agilent Technologies AZ) equipped with a Berkovich diamond tip with a radius smaller than 20 nm and an indent depth of up to 2 μm was used for the experiments. Prior to the test, the indenter tip was calibrated using fused silica. Using the continuous stiffness measurement (CSM) technique, dynamic contact stiffness during the loading time, which is insensitive to thermal drift at this stage, was measured as a function of indentation depth. Hardness and reduced elastic modulus were calculated from the load-displacement curves. All tests were conducted at a strain rate of 0.05/s with a maximum indentation depth of 1500 nm.

2.2.7 Finite Element Analysis

A 3D Representative Volume Element (RVE) was reconstructed using the mechanical and microstructural characterization of Aba Panu samples to simulate the mechanical response. Dream3D, an open-source software, was used to develop the RVE based on the actual size sample. The features of the RVE, including equivalent phase sizes and distribution obtained from Backscattered Electron (BSE) images, were considered, along with porosity, while developing the microstructure-based RVE. This RVE includes three primary phases, namely

metal, chondrule, and matrix, along with porosity. Material properties used to develop a synthetic polycrystalline 3D RVE in real dimensions are presented in Table 2. Periodic boundary conditions were applied for each phase, and a hexagonal mesh was generated in Dream3D, which was later imported into Abaqus software. A finite element model was created to study the mechanical response of the sample. This model used the multiphase 3D RVE in real dimensions. Material properties such as elastic modulus and Poisson's ratio for each mineral were defined using the Engineering constant option in Abaqus. Horizontal translations of the upper and lower parts of the sample were restricted to constrain rigid body motion. Finally, a finite element analysis was performed at a displacement rate of 0.25 mm/min, similar to the experiment. Strains were determined from the average nodal displacement on the surface of interest and compared with the experimental results of the Digital Image Correlation (DIC) measurements.

Table 2. Distribution of Mineral Phases and Properties Used to Generate the RVE.

Parameters	Metal	Chondrule	Porosity	Matrix
Avg. vol%	7%	36%	4%	60%
Max phase size	20.08	49.4	4.48	
Min phase size	6.04	14.87	1.64	
Crystal structure	Cubic	Hexagonal		Cubic
Shape	Ellipsoid	Ellipsoid	Ellipsoid	Ellipsoid
Boundaries	periodic	periodic	periodic	
Elastic Properties	210 GPa	124.5 GPa		142.5 GPa*
Poisson's ratio	0.30	0.25		0.31*

* (Hart, 2015)

2.3 Result and Discussion

2.3.1 Ultrasonic Measurements

The measured values of longitudinal and shear wave velocities of the Aba Panu samples are 4427±94 and 2270±49 m/s, respectively (Table 4). These results are within the range of L-type ordinary chondrites (Jones, 2009), where the mean longitudinal and shear wave velocities are 3443±1389 and 2028±787 m/s, respectively. Using Eqs. (2.1-2.3), the elastic modulus of Aba Panu was calculated as 61.7±2.1 GPa. This variability in elastic wave velocities and modulus can be attributed to the anisotropy and heterogeneous nature of different L-type ordinary chondrites. Variations in mineralogy, porosity, bulk density, and microcracks can influence wave velocities and elastic properties (Flynn et al., 2018; Ostrowski and Bryson, 2019).

2.3.2 Porosity and Pore Size Distribution

Porosity is an important property of the meteorite and affects strength and mechanical response. To calculate the total surface area of a porous material, the Brunauer–Emmett–Teller (BET) theory is widely used (Bardestani et al., 2019). This study estimates the average BET surface area of Aba Panu to be 0.1262 m^2/g, with a molecular cross-sectional area of 0.1620 nm^2 for N_2 adsorption. Multilayer adsorption on micro- and macro-pores was observed from the type II isotherm linear plot shown in Figure 9, indicating unrestricted monolayer and multilayer adsorption on the macro-porous adsorbent. Additionally, the shape of the hysteresis loop offers valuable insights into the pore structure. The presence of a steep slope at a high relative pressure (p/p0) between 0.9 and 1.0 indicates the existence of macropores within the cube. The branches of the hysteresis loop, which can be classified as H3 type, exhibit nearly

parallel behavior across a broad range of relative pressure (p/p0) (Rouquerol et al., 1994). This type of hysteresis loop is commonly observed in slit-like pores with a wide distribution of internal voids and hollow spherical mesopores. The thickness of the pores between 0.3 nm to 0.5 nm was estimated using the Harkins and Jura equation (Emmett, 1946).

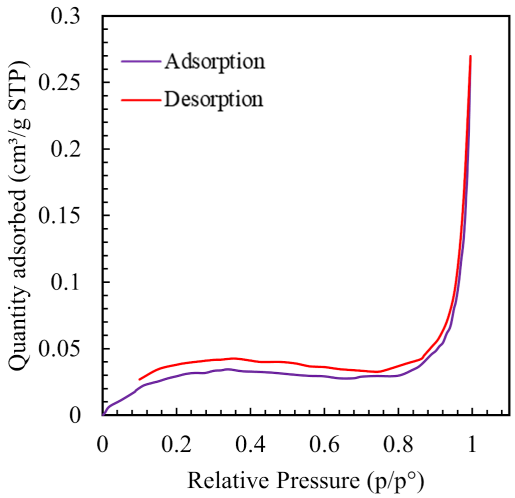

Figure 9. Type II Monolayer-multilayer Adsorbent Isotherm. The Data Is Consistent with a Macro-porous Specimen That Possesses a Wide Distribution of Pore Sizes. Hysteresis Loop from Adsorption and Desorption Isotherm Can Be Classified as H4 Type and Reveals Slit-like Pores, Internal Voids, and Hollow Spherical Mesopores.

Pore sizes are classified as micro- (<2 nm), meso- (2~50 nm), and macro-pores (>50 nm). In the gas adsorption technique, the Barrett-Joyner-Halenda (BJH) method is used to measure the pore size. The average pore size (4V/A) was measured as 44.7 nm, and the cumulative volume of pores was calculated as 0.0004 cc/g from the BJH desorption. Pores ranging from 10.7 to 1.7 nm showed the largest incremental area of 0.011 m2/g (Figure 10a), whereas the most incremental volume of 0.00042 cc/g was observed between pore sizes of 304.7 to 226.7 nm (Figure 10b). Multiple peaks in Figure 8 after the most incremental pore volume are evidence of different pore size distributions for different chondrules and minerals. The

correlation between differential pore areas with an increased pore size suggests the sample has slit pores and macro-cracks.

In addition to studying pore geometry, which includes size and volume, porosity can also be determined by measuring the bulk and grain density of a cube. The use of an N_2 gas pycnometer, which measures true volume, allows us to estimate the grain density. For Aba Panu, the average bulk density was measured as 3.4 g/cm³, while the grain density was slightly lower at 3.3 g/cm³. This difference can be attributed to the averaging error in calculating the bulk volume using a slide caliper. Despite this error, the close values of both densities indicate a very low porosity in the Aba Panu cube. In ordinary chondrites, porosity resulting from micro-cracks is common, caused by the successive compression and decompression of a solid medium due to shock waves during cratering and disruptive events. (Consolmagno et al., 2008).

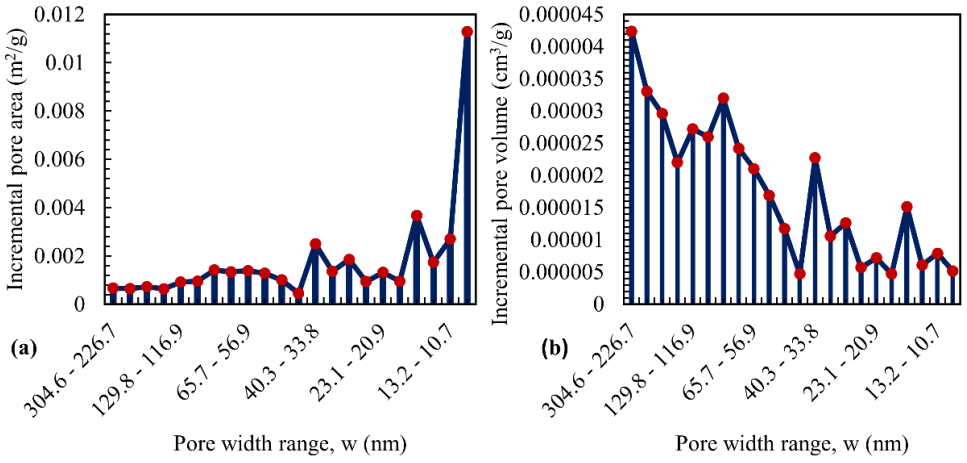

Figure 10. The BJH Adsorption Pore Distribution of Aba Panu Shows a Broad Range of Pore Sizes and Distribution with (a) Incremental Pore Area and (b) Incremental Pore

Volume. The Average Pore Width Is Marked for Each Range and a Stacked Line Is Plotted Through the Markers over Both Bar Charts.

2.3.3 Mechanical Response from Uniaxial Compression Tests and DIC

The mechanical responses of the ten samples under compression loading are presented using the true stress-strain curves (Figure 11). A typical stress-strain response of an Aba Panu cube comprises three regions as shown in Figure 12. The axial and lateral strains were obtained from the in-situ DIC measurement, and the volumetric strains (Figure 12b) were calculated using the following equation (Bieniawski and Bernede, 1979):

$$\frac{\Delta V}{V} \approx \varepsilon_{axial} + 2\,\varepsilon_{lateral} \tag{2.5}$$

Region I records a low initial elastic modulus. It spans 0 to ~0.28% strain when the axial strain starts to show a change in slope due to compaction. This can be attributed to the closing of microcracks and pores due to the increase in inelastic strain in this region (Figure 12b). After 82 seconds or ~0.28% strain, the DIC strain showed nonlinear elastic deformation that corresponds to region II. We estimated the elastic moduli from this region of the stress-strain curves based on the average modulus calculations (Bieniawski and Bernede, 1979). In region III, the DIC captured crack initiation at 175 seconds corresponding to 0.79% strain (see Figure 12c) and propagation until final failure. Although the curves from cubes without experimental artifacts show similar responses, the boundaries of each stage vary slightly due to pre-existing defects (such as voids) and heterogeneity of the microstructure (Figure 7).

The mean compressive strength for Aba Panu is 438.4±77.5 MPa, with a range of 361.7 to 578.0 MPa (Table 3). The tested samples typically failed at the ultimate strength (Figure 12a) without significant deformation at an average failure strain of 0.82±0.18%. Table 3 reports

failure strains from all cubes; these small strain-to-failure values are indicative of a brittle failure mechanism. The mean of the elastic modulus, measured from the slope of all ten stress-strain curves, is 55.5±17 GPa. The results were compared and showed good agreement with the ultrasonic measurements within a deviation of 10% (compare with Table 4). Reported values of compressive strength for ordinary chondrites range from 20.00 MPa (Elenovka) to 456 MPa (Tsarev) (Cotto-Figueroa et al., 2016; Medvedev et al., 1985; Molesky et al., 2015; Ostrowski and Bryson, 2019; Slyuta, 2017; Zotkin et al., 1987). This large range is predominately a result of mineral phase distributions and microstructural defects such as microcracks, voids, nano-, and micro-porosity in the meteorites (Flynn et al., 2018; Ostrowski and Bryson, 2019).

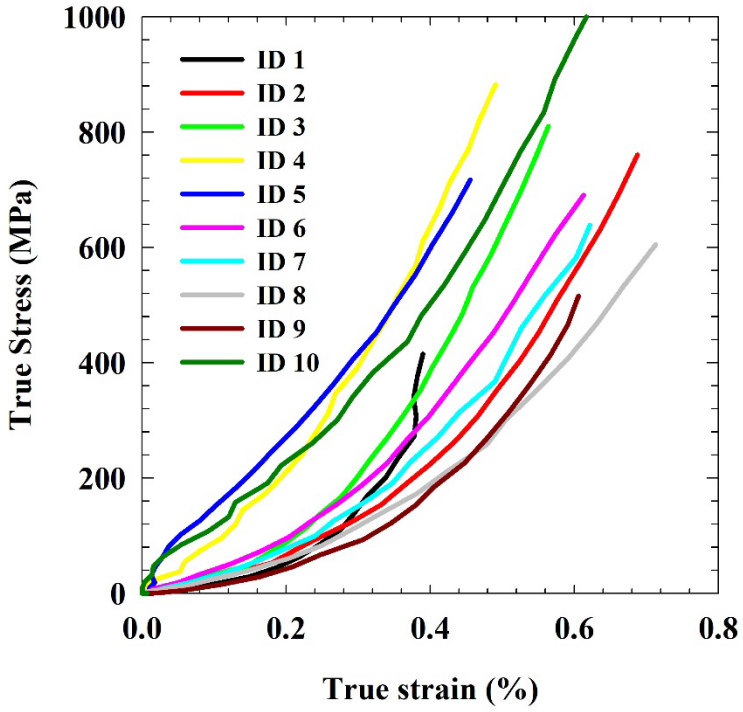

Figure 11. True Stress-strain Responses for Ten Aba Panu Cubes under Uniaxial Quasi-static Compression Loading.

Three samples that did not show an edge effect were selected for the 3-D full-field deformation measurements. Three displacement fields (along x, y, and z), maximum principal strain, and equivalent strain were studied as field variables, provided by default by the DIC software to characterize the failure qualitatively. The displacement and strain contours of one representative sample (sample #1) before failure at strains ~0.002% and ~0.26%, and at failure, at a strain, ~0.48%, are presented to explain the failure mechanism using the DIC (Figure 13 and Figure 14). Contours vary from sample to sample due to different locations of crack initiation and propagation. Axial splitting and multiple fracturing patterns from three samples are shown in Figure 15.

Maximum and minimum values of the y-displacement observed at the top and bottom faces before failure are due to the contact between the sample and compression platens of the Instron machine. Localization spots in the x- and z- displacement contours indicate the likely failure locations since the highest displacements contribute to the failure initiation (Figure 13).

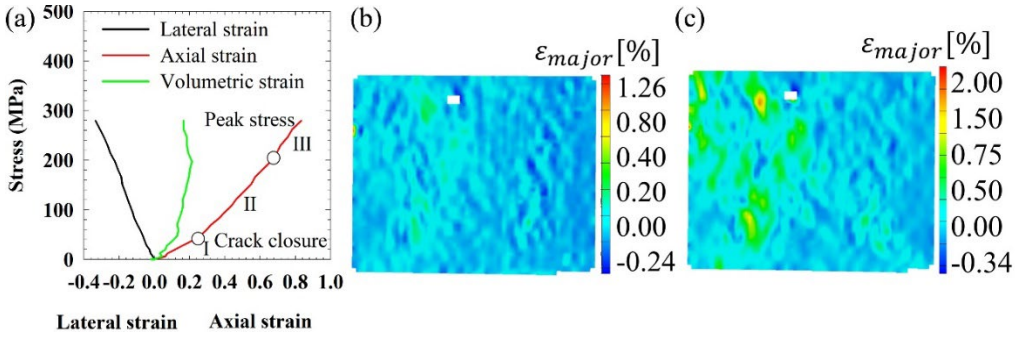

Figure 12. Cube #9 (a) Axial, Lateral, and Volumetric Strains; (b) Major Strain Contour at ~0.28% Strain; And, (c) Major Strain Contour at ~0.79% Strain.

Table 3. Physical and Mechanical Properties of the Ten Aba Panu Cubes.

Cube#	Height (mm)	Width (mm)	Thickness (mm)	Mass (g)	Vol. (cc)	Density, ρ (g/cm3)	Compressive strength, σUCS (MPa)	Failure strain (%)	Elastic modulus, Ec (GPa)
01	10.13	10.13	10.13	3.574	1.04	3.44	365.3	0.48	49.42
02	10.04	10.17	10.17	3.567	1.04	3.44	392.2	0.99	46.35
03	10.13	10.09	10.18	3.584	1.04	3.44	511.4	0.78	77.36
04	10.17	10.12	10.17	3.579	1.05	3.42	548.9	0.67	91.37
05	10.10	10.08	10.08	3.501	1.03	3.41	470.2	0.62	65.60
06	10.17	10.17	10.11	3.611	1.05	3.45	399.1	0.88	49.95
07	10.16	10.10	10.15	3.557	1.04	3.42	382.7	0.91	45.00
08	10.03	10.08	10.10	3.516	1.02	3.44	374.8	1.04	30.79
09	10.03	10.15	10.18	3.570	1.04	3.44	361.7	0.83	42.71
10	10.07	10.15	10.04	3.579	1.03	3.49	578.0	1.02	56.39
Mean:	10.11	10.11	10.12	3.554	1.03	3.44	438.4	0.82	55.49

Table 4. Elastic Properties of the Ten Aba Panu Cubes from Ultrasonic Measurements.

Cube#	Long. wave velocity, VL (m/s)	Shear wave velocity, Vs (m/s)	Elastic modulus, E (GPa)	Shear modulus, G (GPa)	Poisson's ratio, ν
01	4321	2677	58.5	24.7	0.19
02	4360	2708	58.9	24.9	0.18
03	4362	2766	60.9	26.2	0.16
04	4494	2775	63.1	26.5	0.19
05	4342	2797	60.1	26.3	0.14
06	4311	2745	60.4	26.2	0.15
07	4476	2798	63.2	27.0	0.17
08	4442	2806	62.7	27.0	0.16
09	4593	2804	64.5	27.0	0.20
10	4574	2823	65.1	27.5	0.19
Mean:	4427	2770	61.7	26.3	0.17

Although axial displacement fields provide an understanding of the local deformation, crack initiation under compressive load can be better explained by the local strain evolution. The maximum principal strain is computed using the built-in function in the ARAMIS software and the strain field is plotted as contours using the DIC (Figure 14a).

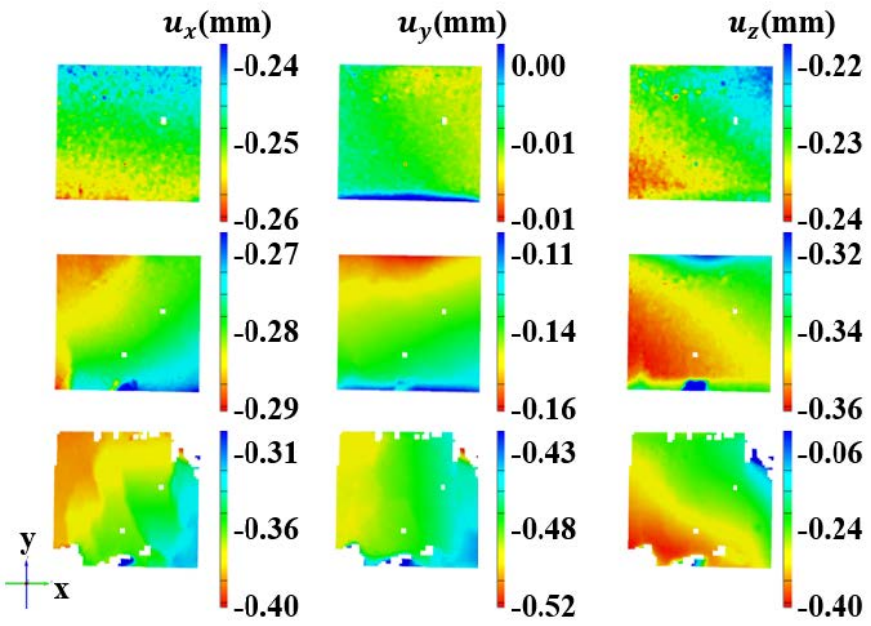

Figure 13. Identification of Local Maxima from the DIC Displacement Contours along the (a) X-axis, (b) Y-axis, and (c) Z-axis for Sample #1 Before (at Strain ~0.002% and ~0.26%) and at Failure (at Strain ~0.48%).

The contour of maximum principal strains is associated with local tensile and compression strains which detect crack initiation sites before failure at a strain of ~0.26% in this sample. Subsequently, it provides the direction of crack propagation and failure pattern by locating the maximum principal strain. The global axes of the resulting maximum principal strains did not show rotations, whereas as expected the local axes show localizations due to the heterogeneous microstructure and geometrical discontinuity. Maximum values depicted in red color in the contour expose the crack initiation site and yellow colors expose the path and direction for crack propagation. Another important strain field variable, known as the equivalent strain, is also used for identifying the failure patterns (Figure 14b).

The equivalent strain was obtained in this experiment by default from the ARAMIS 3-D DIC using Eq. 2.5. Unlike principal and shear strains, the equivalent von Mises strain provides

a scaler numerical value that is suitable to investigate the failure pattern since it considers both normal and shear components of strain. As shown in Figure 14b, the region of maximum equivalent strain before the failure develops at the bottom face of the sample due to the nucleation of microcracks. With the increase of load, adjacent microcracks are connected creating a larger crack and more microcracks begin to coalesce from the top face that provides the information about the path of crack propagation. The analysis of the contour of equivalent strains before and at failure shows the effectiveness of the full-field DIC measurements to detect the location of crack initiation regardless of the difference in the failure mechanisms.

2.3.4 Failure Mechanism

Pre-existing microcracks in the Aba Panu meteorite samples are presumably caused by the complex formation of the parent body, thermal and shock processes in space, and shock events during its entry to Earth (Flynn et al., 2018; Pohl and Britt, 2020; Slyuta, 2017). The failure during the uniaxial compression tests originates from pre-existing microstructural flaws. The failure mechanism involves pre-existing microcrack closures, microcrack growth, and subsequent failure, as shown in the mechanical response (Figure 12). Full-field DIC maps locate the maximum strain from the maximum principal strain and equivalent strain contour maps (Figure 14). The maximum strain results from localized tensile stress acting on microcracks that orient parallel to the principal stress direction. It can be explained, as the applied compressive load increases, it induces tensile stresses at the tip of cracks causing a high-stress concentration and when this stress overcomes the local tensile strength, new cracks, known as wing cracks, begin to form in the oblique direction to those flaws.

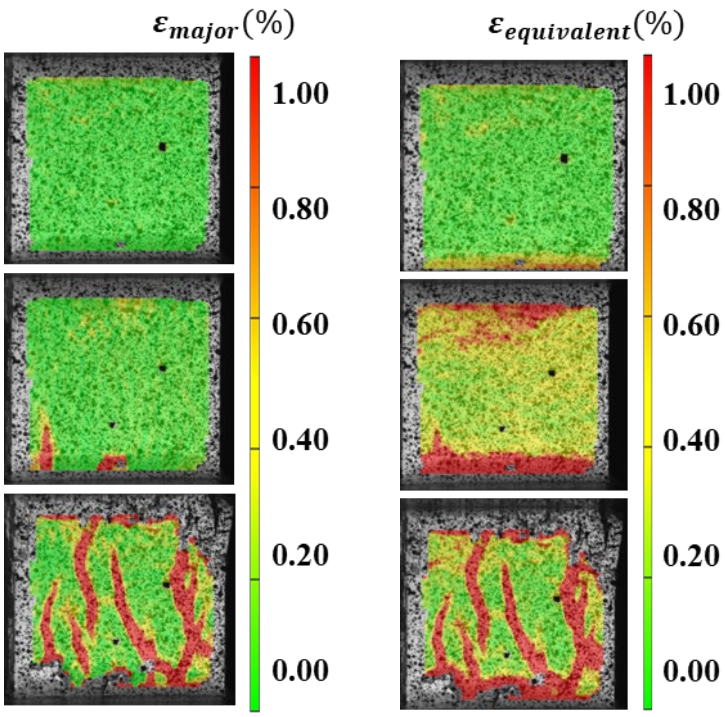

(a) (b)

Figure 14. Identification of Crack Initiation and Failure Pattern from DIC Strain Contours by (a) Maximum Principal Strain Associated with a Local Tensile and Compressive Strain, and (b) Equivalent Strain (von Mises), a Single Scaler Numerical Value Determined from the DIC Measurements, for Sample #1 Before (at Strain ~0.002% (Top) and ~0.26% (Middle)) and at Failure (at Strain ~0.48% (Bottom)).

Additional increases in loading cause many wing cracks to form and grow in parallel to the maximum principal stress direction and then to coalesce and cause failure in axial splitting (Figure 15). This failure mechanism is commonly seen in brittle materials (Bobet and Einstein, 1998). The regions noted as numbers 1 and 2 in Figure 15 represent the chronology of crack initiation for three different samples. In Figure 15a, cracks start from the bottom face of the cube shown by region 1. As the applied load increases, more cracks originate from the top face on the XY plane, resulting in axial splitting. Figure 15b shows that the crack initiation

happens along the YZ plane and afterward, a large axial crack grows from the top face along the XY plane showing failure in multiple in-plane axial splitting. Figure 15c shows cracks originating first from the YZ plane, but a large crack grows at high stress from the bottom face of the XY plane, and the coalescence of other cracks leads to failure in a multiple fracturing mechanism, suggesting that the propagation of wing cracks was guided by the heterogeneity in the microstructure. This results from the release of strain energy leading to random breakage of the sample at higher compressive stress. Different locations of the crack initiation may be caused by the spatial distribution of flaws and relatively weaker zones present in each sample (Flynn et al., 2018; Pohl and Britt, 2020).

Furthermore, the analysis of maximum principal strain before failure was extended on two additional Aba Panu samples by overlaying its contour on optical micrographs to understand the influence of different minerals that contributed to the failure mechanism (Figure 16). An optical micrograph of a representative sample shows the location of metals, chondrules, and matrix (Figure 16a).

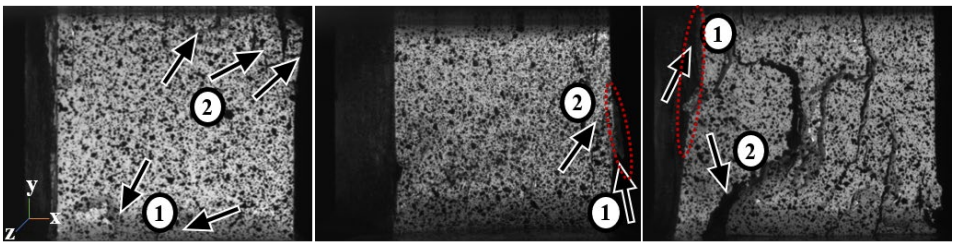

(a) (b) (c)

Figure 15. Failure Pattern of Three Different Cubes Showing (a) Axial Splitting (Sample#1, Strain ~0.48%), (b) Multiple In-plane Axial Splitting (Sample# 2, Strain ~0.98%), and (c) Multiple Fracturing (Sample# 9, Strain ~0.82%). Numbers on the Inset of Each Image Represent the Order of Crack Initiation During Loading.

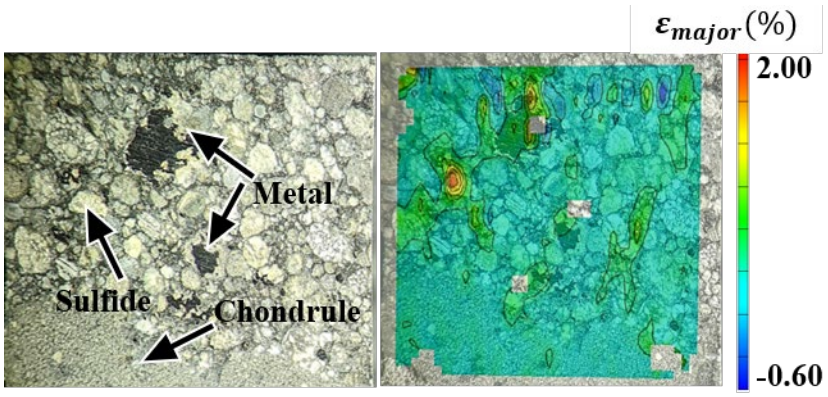

(a) (b)

Figure 16. (a) Optical Image of 1-cm Aba Panu Cube Showing the Mineralogy and Texture, (b) an Overlay of the Maximum Principal Strain Contour Showing Strain Concentration Around the Large Metal Grains.

Metals in ordinary chondrites are ductile whereas chondrules, troilite, and matrix are brittle (Liang et al., 2020). This may lead to differences in local displacement and strain due to a mismatch between the strength, stiffness, and nature of the fracture. However, optical micrographs of the fracture surfaces showed no evidence that any particular minerals are more responsible than the others in the failure initiation (Figure 16b). This implies the defects present in the microstructure such as porosity, micro-voids, microcracks in chondrules, matrix, and interfaces between matrix metals are the source of crack nucleation, which finally leads to failure.

Table 5. Physical and Mechanical Properties of Aba Panu, Compared with the Literature Values of (M=mean, Sd=standard Deviation) L-type Ordinary Chondrites.

Material	Bulk density (g/cm^3)		Porosity (%)		Elastic modulus (GPa)		Ultimate compressive stress (MPa)	
	M	SD	M	SD	M	SD	M	SD
Aba Panu (L3) ordinary chondrite	3.44	0.03	-	-	55.49	17.04	438.42	77.52
L ordinary chondrite	3.35*	0.16*	5.8*	4.7*	39.69†	26.90†	299♦	164♦

*Britt and Consolmagno, 2003, †Jones, S.F., 2009, ♦Pohl and Britt, 2020

2.3.5 Fragment Analysis

Fragments of the Aba Panu samples from compression tests are further analyzed to calculate the fractal dimension and examine the roughness related to their structural heterogeneity (Figure 17). The fractal dimension provides insight into the fracture properties of rocks, concrete, or ceramics (Borodich, 1999; Kuls'kov et al., 2006; Saouma and Barton, 1994). The analysis begins with dry sieve analysis on fragments to develop a cumulative particle mass distribution. Finally, the fractal dimension is derived using the box-counting method, and the joint fracture coefficient is calculated to determine the roughness of the fracture surface.

Each fragment is analyzed using the open-source image processing software, ImageJ, to determine its size and shape. First, a median filter is applied to reduce noise by around 3 pixels, and then the target image is converted to an 8-bit image for threshold adjustment. Boundaries between adjacent particles are generated from the binary image using the watershed command in ImageJ. Subsequently, all particles are analyzed to estimate their aspect ratio and size distribution. The average fragment area and perimeter are estimated to be 3.03 mm^2 and 6.70 mm (n=465), respectively. Notably, almost 85% of the fragments belong to a size of < 2 mm

(n=392 out of 465), and the estimated mean circularity is 0.64, indicating random shapes of the fragments. Additionally, dry sieve analysis reveals that the particle size distribution of fragments is dominated by particles in the micron size range. Table 6 details the cumulative mass and particle number of the tested fragments. Power-law size distribution on asteroid population is commonly applied to explosion and impact fragmentation of rocky materials (Hawkins, 1960; Mc Crosky, 1968). This power-law size distribution can be expressed as N≈m^(-b), where N is the number of fragments of mass > m, and b is the negative slope in the log(N) – log(m) plot, also known as the fractal dimension.

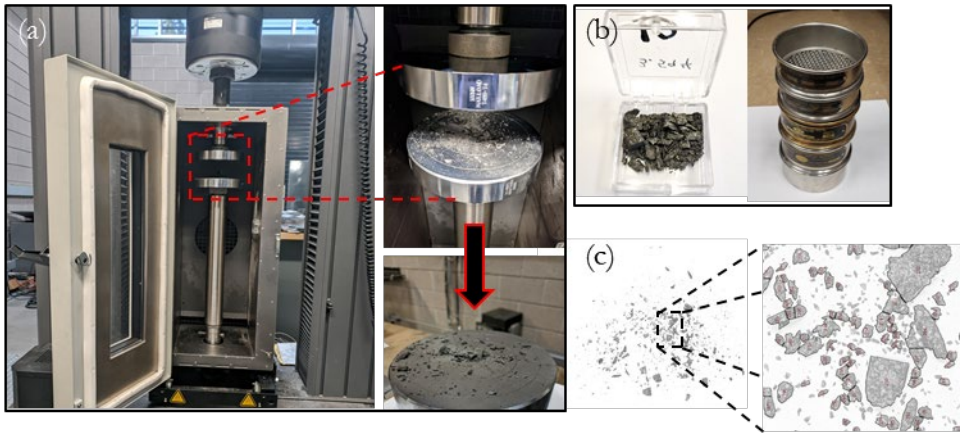

Figure 17. (a) The experimental setup for the fragment analysis shows the fragments after quasi-static compression testing, (b) crushed sample and different-sized sieves, and (c) image processing for the morphological analysis using ImageJ.

Table 6. Fragment Mass and Size Distribution.

Sieve no.	Sieve size (mm)	Avg. mass (gm)	Cumulative mass (gm)	Percent retain (%)	Cumulative percent retained	Percent passing (%)	Particle number	Cumulative particle number	Fractal Dim., D	JRC
10	2.00	2.43	2.43	72.59	72.59	27.41	23	23	1.20	59.20
20	0.84	0.52	2.95	15.63	88.23	11.77	96	119	1.26	66.0
40	0.00043	0.20	3.15	6.08	94.31	5.69	501	620	1.55	91.74
60	0.00025	0.08	3.23	2.27	96.58	3.42	1,139	1,759	1.75	104.72
	Pan	0.10	3.33	2.97	99.55	0.45				
	Sum	3.33								

The power-law size distribution of the Aba Panu sample shows a fractal dimension of 1.28 (Figure 18), suggesting a comparatively smooth profile of the small fragments. The analysis continued for each sieve size of 2, 0.84, 0.00043, and 0.00025 mm to obtain the distribution of fractal dimensions (Figure 19). The box-counting method, which is already built into the ImageJ software, is used to calculate the fractal dimension. 2-D images of fragments are analyzed and split into square boxes with a side length of ε, which are then used to cover the images and count the total number of boxes, N. By taking the ratio of log(N) and log(1/ε) as ε tends to 0, the fractal dimension is calculated (Wu et al., 2020). A total of 1139 particles passed through the smallest sieve of 0.00025 mm, showing a fractal size of 1.20, which can be attributed to extreme grinding. As the sieve size increases, a maximum fractal dimension of 1.75 is estimated, as shown in Figure 19. Matsumoto et al. (2018) reported that the fractal dimension of the cumulative crater diameter of Itokawa particles varies from 1.3 to 2.3 (Matsumoto et al., 2018). An empirical formula establishes a relationship between fractal dimension (D) and Joint Roughness Coefficient (JRC), given by $JRC = 118.89(D-1)^{0.4343}$

(Li and Huang, 2015). JRC is considered one of the major factors that affect the strength and deformation of stony meteorites and is related to peak shear strength (Otto et al., 2021). A mean JRC of 80.52 ± 18.4 has been calculated, indicating that roughness increases with the increase in the spatial dimension of the fragment particles. Aba Panu exhibits a lower fractal dimension and JRC, which may suggest compound fragmentation phenomena that can be compared to hypervelocity impact and/or repeated collisions of meteorite fragments.

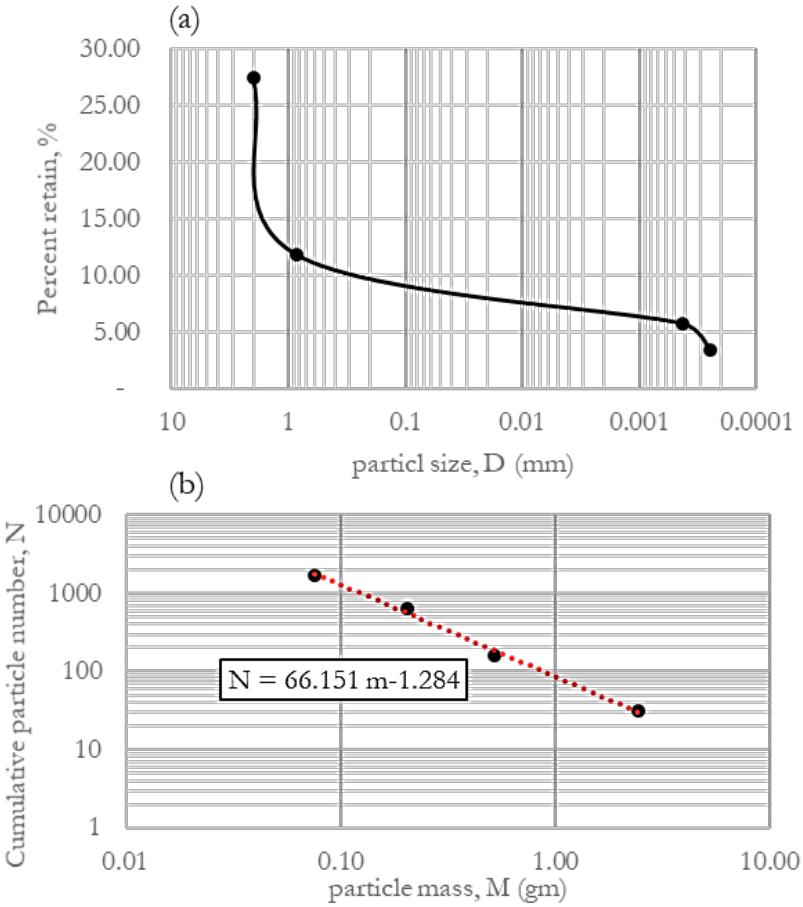

Figure 18. Fragment Sieve Analysis shows (a) Particle Size Distribution, and (b) Cumulative Particle Mass Distribution on a Log-scale. The Slope of the Power Law Distribution in Log (N) – Log (M) Shows a Fractal Dimension of 1.284.

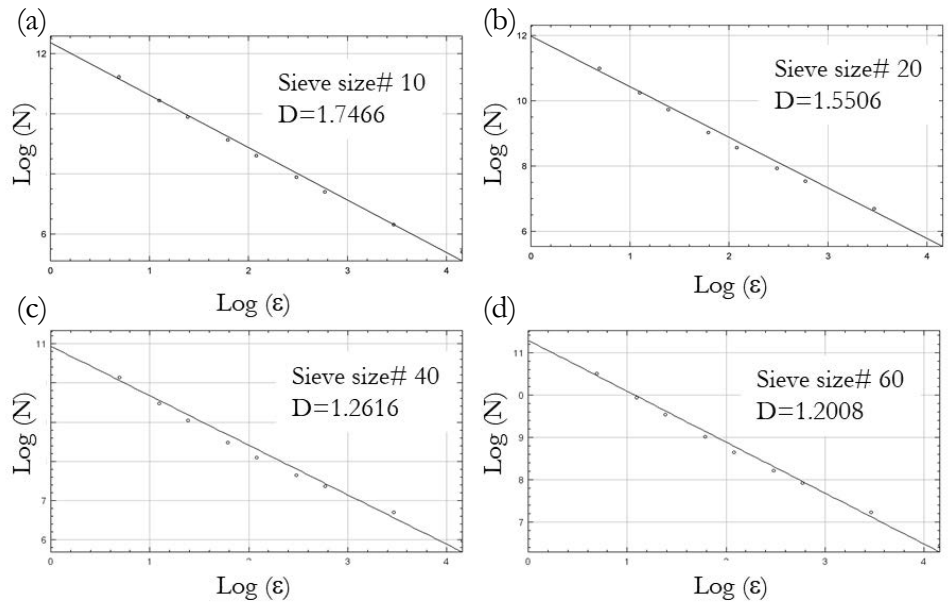

Figure 19. Fractal Dimension Measurement for (a) Sieve Size 10, Opening 2 mm, (b) Sieve Size 20, Opening .84 mm, (c) Sieve Size 40, Opening .00043 mm, and (d) Sieve Size 60, Opening .00025 mm Using the ImageJ Box-counting Method. Fractal Dimension Decreases with the Increase of Sieve Sizes.

2.3.6 X-ray Computed Tomography (X-CT) and Nanoindentation

Chemical analyses of the primary silicates (olivine and pyroxene), troilite (FeS), metal (Fe-Ni), and matrix phases were obtained using EMPA equipped with WDS and EDS and then correlated with X-CT and nanoindentation analysis (Figure 20). X-CT was performed to investigate the presence of initial defects, such as voids and cracks, in the sample. Using the identified mineral phases, X-CT projection images were used to develop a 3-D representation of the sample to estimate the 3-D phase distribution. Nanoindentation was then performed on these phases to estimate the local mechanical properties, such as hardness and elastic modulus (Table 7).

Table 7. Mechanical Properties of the Primary Mineral Phases in Aba Panu Determined by Nanoindentation.[+]

Mechanical properties		Olivine/ Pyroxene	Metal (Fe-Ni)	Troilite (FeS)
Modulus (GPa)	Mean	179.09	211.26	107.95
	Std. dev.	9.31	9.43	3.39
Hardness (GPa)	Mean	13.87	3.31	3.85
	Std. dev.	0.95	0.14	0.21

([+] TJ Huang et al., 2021)

The minerals are distinguished based on their different X-ray absorption properties (Friedrich et al., 2008), resulting in 83.55% olivine and pyroxene, 12.61% matrix, 1.86% kamacite, and 1.98% troilite. The glass phases inside the chondrule are easily distinguishable but challenging to segment automatically due to their complex morphology. For comparison, the most abundant phases in ordinary chondrites are olivine and pyroxene, which combined vary from 46.7 to 85.4 wt.% (Dunn et al., 2010). Dunn et al., (2010) also reported that average olivine phases increase from H- to LL-chondrites, but pyroxene phases show the opposite trend. Aba Panu, L3 ordinary chondrites show a similar mineral phase distribution that is consistent with the typical modal analysis of ordinary chondrites.

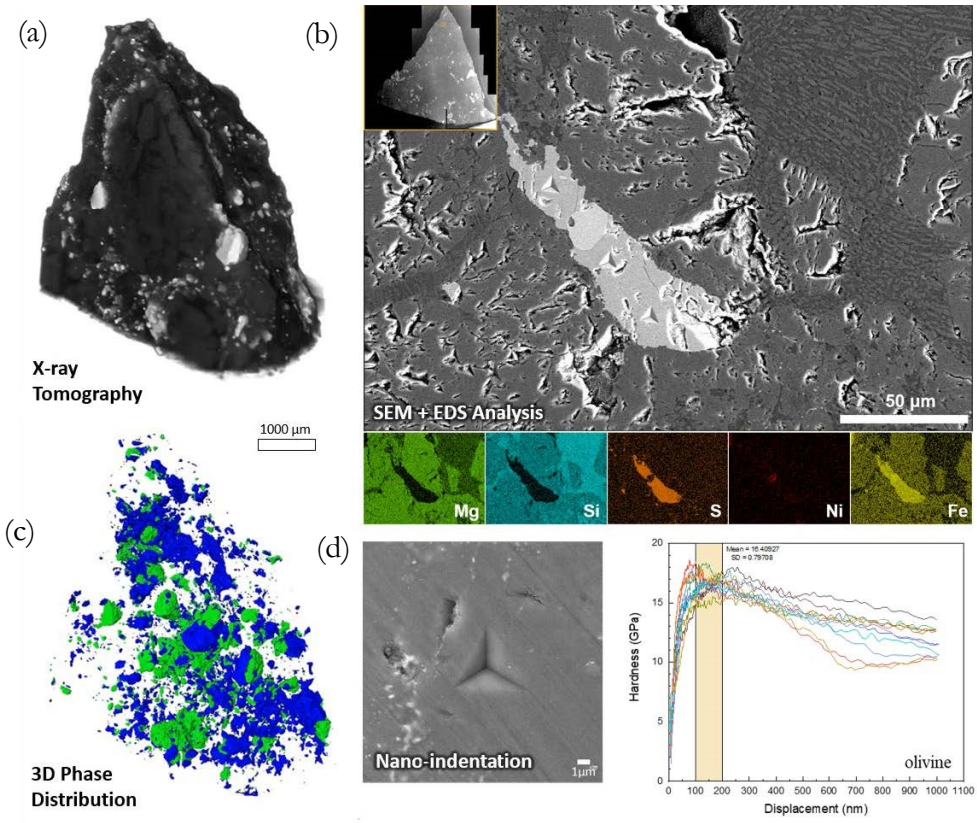

Figure 20. A Correlative Study on Aba Panu Shows (a,c) X-ray Tomography of a Sample and Its 3D Phase Distribution Obtained from the Segmentation of Major Elements, (b) SEM Image and EDS Maps of Different Minerals, and (d) Local Mechanical Properties Using the Nanoindentation (Source: T J Huang et al., 2021).

Furthermore, local mechanical properties such as elastic modulus and hardness can be calculated from the load-displacement curve obtained by nanoindentation for different phases. The continuous stiffness measurement (CSM) technique is used to determine mechanical properties as a function of indent depth. Nanoindentation is conducted with a strain rate of 0.05/s and a depth of 200 nm for olivine and pyroxene, and 500 nm for Fe-Ni metal and troilite (FeS). The results show a higher elastic modulus of 211.16 ± 9.31 and reduced hardness of 3.31 ± 0.14 for Fe-Ni metal phases compared to other phases. On the other hand, the average hardness of 13.87 ± 0.95 for olivine and pyroxene is higher than that of other phases.

The average micromechanical properties of different phases in the Aba Panu meteorite are similar to those of the Chelyabinsk LL5-6 ordinary chondrite (Moyano-Cambero et al., 2017). The dissimilar properties of multiple phases can result in the nonlinear bulk strength of the material. Mechanically hard olivine and pyroxene dominate Aba Panu and can be considered load-bearing phases, with relatively weaker phases of metal and troilite. The difference in elastic modulus between the hard phase and the bulk sample may suggest that with an increase in size, the total volume of preexisting flaws increases, resulting in a lower modulus in the bulk property measurements.

2.3.7 Numerical Modeling

A microstructure-based 3-D Representative Volume Element (RVE) can be reconstructed from the 2D surface micrograph and used to represent the mechanical response and failure of Aba Panu. The RVE is acquired by combining the EPMA data and the corresponding BSE images. Using characteristic features such as volume fraction, size, and shape distribution of chondrules and minerals, a simple polycrystalline polyphase synthetic microstructure was built using open-source Dream3D software. This RVE is simplified by considering only two primary phases: matrix and porosity. The two primary phases are assumed to be chondrules and metals, with their statistical distribution of phase size calculated from the microstructure. The pore size distribution, obtained from BET and BJH methods, was incorporated as precipitates, and the remaining phases were generalized as the matrix in the microstructure (Figure 21). Crystallographic features were assumed to be similar to other ordinary chondrites (J. Petrovic, 2001). Periodic boundary conditions were applied to the primary phases and the precipitates during the RVE reconstruction. Material properties required for the modeling were obtained from the uniaxial compression test. Despite the limitations of the simplified

model, numerical analysis was performed on the RVE using Abaqus, yielding reasonable results.

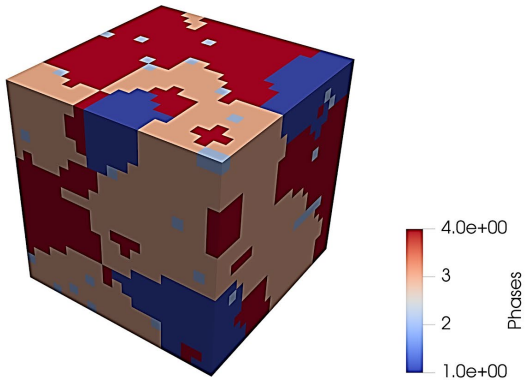

Figure 21. 3-D Synthetic Polycrystalline RVE Development for the Aba Panu Cube Using the Dream 3D Software Showing Three Phases (Metal in Blue, Chondrule in Brown, and Matrix in Red) and Defects (Porosity) in Light-blue Color.

The stress-strain response from the Finite Element (FE) model (Figure 22a) captures the elastic and post-elastic behavior of Aba Panu. However, the crack-closing phenomena were unable to be captured by this simple model. Hence, despite a similar elastic modulus, a slight difference in the stress-strain response was detected between the model and experiment. High equivalent stress (von Mises) was observed close to the microstructural defects (Figure 22b) indicating possible locations of crack initiation. The maximum local stress appears on the FE model towards the edge with surface defects. The results of the numerical simulation of the compression test, performed at a constant displacement rate, show a close approximation in the equivalent strain obtained from the DIC measurement.

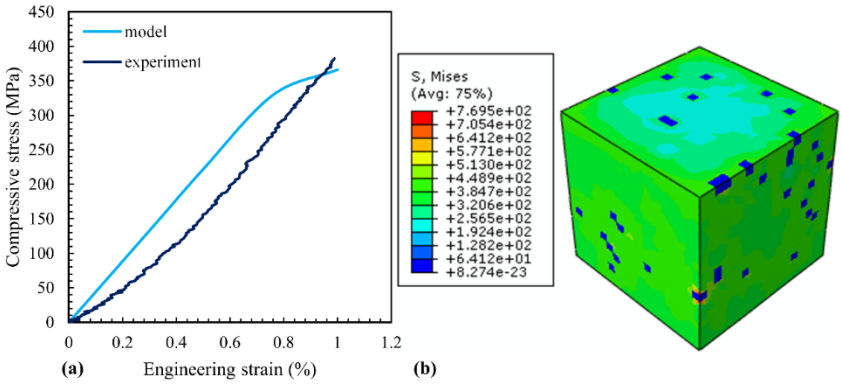

Figure 22. (a) Comparison Between the Experimental Result and the FE Model Shows the Stress-strain Response, and (b) Numerical Modeling for Compression Test Showing High Equivalent Stress (von Mises) Close to Defects Using the Abaqus Software.

2.3.8 A Phenomenological Model for Meteorites' Crack Closure Effect

A wide range in strength for ordinary chondrites has been reported in recent studies, indicating the influence of important factors such as physical and mechanical properties, multiphase minerals, and metal contents. Meteorite porosity alone can affect various physical properties, including deformation under stress, strength, and impact response. Therefore, we advance this numerical approach by introducing an appropriate brittle damage model to simulate the experimentally observed damage mechanisms and better understand the response and failure behaviors of the Aba Panu meteorite.

The mechanical response of Aba Panu meteorite samples (Figure 12a) can be divided into three stages: (i) crack closure, (ii) non-linear elastic deformation, and (iii) crack initiation and rapid propagation. The presence of microcracks affects the strength and deformation behavior of meteorites. Compression tests show an initial non-linear response, which refers to the crack closure phenomenon. The effect of preexisting microcracks can be evaluated using the

effective medium theory (Schubnel and Guéguen, 2003), which represents the total strain as a function of matrix strain and extra strain induced by the microcracks.

$$\varepsilon_{ij} = \varepsilon^{o}_{ij} + \Delta\varepsilon_{ij} = (S^{o}_{ijkl} + \Delta S_{ijkl})\sigma_{kl} \tag{2.6}$$

Matrix axial strain represents strain without preexisting cracks. It is linearly related to the elastic modulus of the sample and can be written as $\varepsilon_1^m = \frac{\sigma_1}{E}$, where $\sigma_1 and\ E$ are the applied axial stress and elastic modulus, respectively. For one-dimensional analysis, the non-linear elastic response of the meteorite can be modeled by assuming cracks (preexisting microcracks) axial strain as a negative exponential function of axial stress (Peng et al., 2015).

$$\varepsilon_1 = \frac{\sigma_1}{E} + V_m[1 - \exp(-\frac{\sigma_1}{n})] \tag{2.7}$$

where, the model parameter, Vm represents maximum closure strains of microcracks, and n is a model parameter with stress unit.

Damage due to the initiation of new cracks under compression and its growth can be written as

$$\sigma = E\varepsilon(1 - D) \tag{2.8}$$

Where σ is the effective stress, ε is the strain, and D is a damage variable. Assuming that the internal microcracks in the damage process are random and the strength of microcrack elements obeys a Weibull distribution, then the micro-element damage rate can be written as:

$$\frac{dD}{d\varepsilon} = \frac{m}{a}\varepsilon^{m-1}\exp(-\frac{\varepsilon^m}{a}) \tag{2.9}$$

The Weibull shape parameter, m, and scale parameter, a, can be calculated based on the peak stress and peak strain, using the following equations: (Li et al., 2021; Yang et al., 2005).

$$m = \frac{1}{\ln(E\varepsilon_c / \sigma_c)}, and \;\; a = m\varepsilon_c \tag{2.10}$$

Where $\sigma_c$is the peak stress and ε_c is strain corresponding to the peak stress.

The effectiveness of the model is verified with the experimental test data, and a combined stress-strain response is shown in Figure 23. The current phenomenological model successfully captures the initial crack closure of the Aba Panu sample. We estimate the model parameter Vm for the maximum crack closure strain of the crack as 0.0021, which closely matches the experimental data. The other model parameter n determines how the crack closure behaves and is estimated as 31.9. However, these parameters may vary with changes in the stress-strain response of Aba Panu.

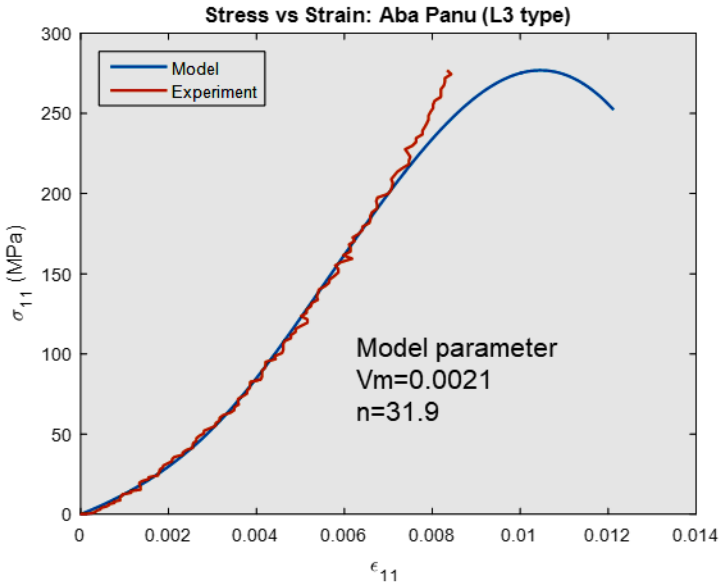

Figure 23. Comparison of the Proposed Empirical Model Used to Capture the Initial Crack Closure Phenomena with the Experimental Stress-strain Response of the Aba Panu Meteorite.

As the model parameter n increases, the crack-closure effects start to minimize, as shown in Figure 24. So, at a higher n value, the sample behaves as a solid material without any microcracks and microstructural flaws. Another model parameter, Vm, represents the maximum strain of microcrack closure, and as it increases, this model predicts more microcracks present in the sample. As a result, it requires a relatively high load to close all microcracks. Although this phenomenological model is limited to the physics-based interaction of complex microstructure and preexisting flaws, it shows promise in capturing the initial crack closure for the brittle fracture response of the Aba Panu meteorite sample.

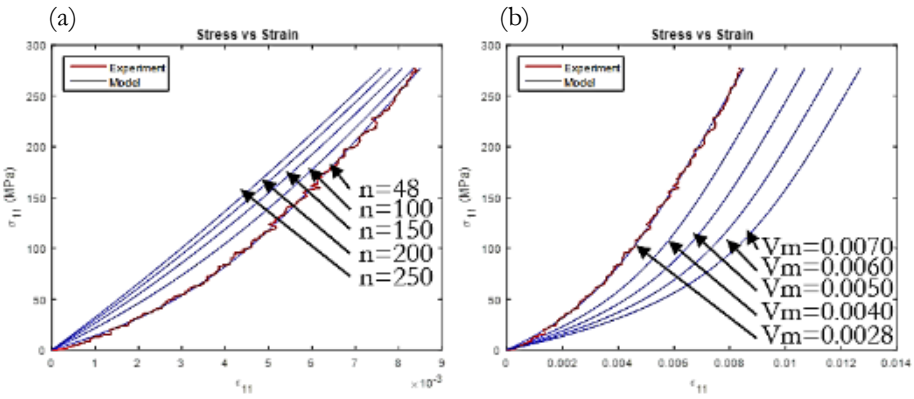

Figure 24. Parametric Study of Model Parameters (a) n Shows the Influence of Microcracks Present in the Sample as the Increase of n Reduces the Effect of Crack Closure and (b) Vm Shows the Effect of Maximum Crack Closure Strain in Model Stress-strain Response.

2.4 Summary

This study presents the analysis of the failure mechanisms of the Aba Panu meteorite using full-field 3-D digital image correlation (DIC) as a non-contact measurement technique, under quasi-static compression loading conditions. The Aba Panu samples exhibit comparatively higher strength than previously studied ordinary chondrites. A range of fine to coarse grain Fe-Ni, with various morphological characteristics, presence of cracks, and crack-filling troilite (Figure 6 and Figure 7), leave a possible indication of strength variation in an inhomogeneous microstructure. The mineralogical study reveals that the brittle failure behavior of Aba Panu is dominated by silicates. Under quasi-static loading, multiple hotspots (locations of maximum strain) in the evolution contour of maximum principal and equivalent strains, as identified from the DIC analysis, indicate multiple microcrack nucleation and propagation sites. Furthermore, qualitative analysis of strain localization using high-spatial-resolution images showed good correspondence with optical micrographs, revealing axial splitting failure and multiple fracturing mechanisms originating from preexisting microstructural flaws. The full-field DIC technique can be applied to investigate in-situ deformation and failure in other similar asteroidal materials. Additionally, a correlative study on mineral phases and local mechanical properties revealed the presence of strong load-bearing phases such as olivine and pyroxene, and weak phases such as troilite.

To understand the variation of strength in brittle failure using numerical modeling, a Representative Volume Element (RVE) was developed based on the microstructural characteristic features of the Aba Panu meteorites. Although the RVE was simplified to assume only three primary phases from chondrules and minerals, its response to equivalent strain can closely approximate the experimental response. A model combining a

phenomenological model of crack closure and a damage constitutive relationship was developed to describe the brittle behavior of the Aba Panu (L3) meteorite. The model predicts the initial crack closure due to compression loading, which closely follows the damage progression.

The obtained results improve our understanding of the response of typical ordinary chondrites under compressive loading, which is a step forward in predicting the properties of asteroidal materials during sample return missions, resource utilization, scientific exploration, and hazardous asteroid mitigation. The insights into the failure mechanisms of the Aba Panu meteorite can also help interpret asteroid disruption and develop strategies to mitigate potential hazards during space exploration and Earth impact events.

CHAPTER 3

MULTIMODAL CHARACTERIZATION AND FAILURE ANALYSIS OF THE VIÑALES (L6) ORDINARY CHONDRITE

3.1 Introduction

Meteorites, the remnants of asteroids and comets that have survived the Earth's atmospheric entry (Petrovic, 2001), offer valuable insights into the estimation of the physical and mechanical properties of asteroids (Ostrowski and Bryson, 2019, 2020; Petrovic, 2001; Slyuta, 2017). This knowledge plays a critical role in the development of strategies to mitigate planetary defense hazards (Council et al., 2010; Daly et al., 2023; Rivkin and Cheng, 2023; Sears et al., 2016, 2015). The properties of meteorites are influenced by the diverse composition of their constituents, the distribution and volume fractions of individual minerals, and the presence of preexisting flaws (Cotto-Figueroa et al., 2021; Rabbi et al., 2021).

The microstructure and mineral compositions of meteorites offer valuable insights into their complex history, encompassing their formation within the parent asteroid and subsequent ejection from it (Rubin, 1997). The mineralogy of meteorites serves as a source of information about the environmental conditions prevailing on the parent body, including factors such as oxygen fugacity, temperature, pressure, and shock events, which exert notable influences on their physical and mechanical properties. Certain meteorites undergo thermal, aqueous, or shock alteration, leading to the development of a diverse microstructure that imparts distinct physical properties in comparison to their original state within the parent bodies (Endress et al., 1996). During the thermal metamorphism, changes are induced in the structural and chemical properties of chondrites, resulting in the equilibration of silicate

compositions and the crystallization of fine-grained matrix and chondrules. These alterations manifest in various microstructural features observed in chondrules and minerals, including micro-cracks, voids, irregular fractures, and intersecting cracks (Leroux, 2001). These flaws can also be attributed to shock-induced metamorphism (Leroux, 2001; Molaro et al., 2015) as well as the substantial thermal gradient existing between different phases, arising from disparities in thermal conductivity and elastic modulus (Liang et al., 2020).

The mechanical behavior and deformation mechanisms of meteorites are influenced by the presence of preexisting flaws, diverse mineral compositions, and complex heterogeneous microstructure (Hogan et al., 2015). To assess the strength of ordinary chondrites, compression tests have been employed as they provide insights into the fragmentation processes that occur during the atmospheric entry of meteorites (Cotto-Figueroa et al., 2016; Hogan et al., 2015; Medvedev et al., 1985; Rabbi et al., 2021; Slyuta, 2010; Voropaev et al., 2017). The strength properties of meteorites vary across different sample sizes and length scales, highlighting the intricate nature of understanding their mechanical behavior and deformation mechanisms (Ostrowski and Bryson, 2019; Popova et al., 2011; Slyuta, 2017).

Ordinary chondrite meteorites typically demonstrate brittle responses under uniaxial compressive load, where fracture mechanisms involve the initiation of tensile microcracks from preexisting flaws. The relative frictional sliding of these flaws generates tension microcracks that deviate sharply from the sliding plane (Paliwal and Ramesh, 2008). These microcracks eventually merge, resulting in axial splitting. Therefore, controlled laboratory testing of meteorites is crucial to evaluate their mechanical properties and gain insights into their detailed physical responses.

In this study, the Viñales meteorite was analyzed using electron probe microanalysis (EMPA) and X-ray micro-computed tomography (X-CT) to investigate its constituents.

EMPA analysis was utilized to detect major elements such as Fe, Ni, and others from Backscattered Electron (BSE) images, which were then correlated with CT scan images obtained from X-CT. The distribution of high-density phases within the samples was estimated from the X-CT scans, and the mechanical properties of the Viñales meteorite were determined through quasi-static compression tests. Due to the limited availability of rare meteorites, conducting a large number of tests to fully characterize their mechanical behavior is often not feasible. Therefore, the findings from this study could be valuable in developing physics-based predictive models that can reduce the need for expensive tests and provide insights into the mechanical behavior of similar meteorites.

3.2 Materials and Methods

The Viñales meteorite fell in 2019 in the northwestern region of Cuba's province of Pinar del Rio (Gattacceca et al., 2020). In this study, fourteen 1-cm cube samples were prepared from a Viñales stone obtained from the ASU Buseck Center for Meteorite Studies (Figure 25b). Viñales has a well-preserved black fusion crust with a smooth, matte texture. Yin and Dai (2021) reported a two-layered fusion crust with the upper layer displaying tiny dendritic and skeleton crystals of olivine and pyroxene, while the lower layer shows more fractured mineral grains and metal inclusions (Yin and Dai, 2021). Viñales has shock-metamorphic features such as shock melt veins, fractured minerals, recrystallized Fe-Ni metals, and troilite (Figure 25a). The shock stage is classified as S3 or partly S4, indicating a shock pressure of > 5-10 MPa (Gattacceca et al., 2020). Viñales is an equilibrated L6 ordinary chondrite due to its average Fa and Fs contents in olivine and pyroxene, medium-grained feldspar grains, and recrystallized matrix (Gattacceca et al., 2020).

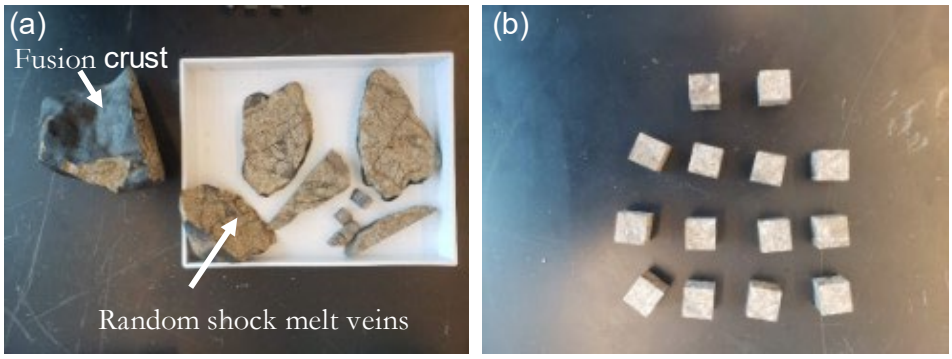

Figure 25. Viñales Meteorite (a) Shows a Black Fusion Crust with a Tan Interior and Dark Shock-melt Veins, and (b) Fourteen 1-cm Cubes for the Experiments Prepared from One of the Slices in (a).

The analysis of mineral compositions and their different phases was conducted using a field emission electron microprobe analyzer (EMPA, JEOL JXA-8530F Hyperprobe) equipped with wavelength dispersive spectrometers, operating at an exciting voltage of 20 kV and a beam current of 58.9 nA. A correlative study was carried out by comparing x-ray elemental maps from the EMPA and backscatter electron images from the SEM to characterize the microstructure.

Mineral distributions were investigated using the X-CT technique. X-CT images were acquired using a microfocus sealed X-ray source (Bruker Skyscan 1272) and a 16-MP X-ray detector (4904 x 3280 pixels), which was a 14-bit cooled CCD fiber optically coupled to a scintillator. X-CT was operated at a voltage of 100 kV and a current of 100 μA. A 3D density volume was reconstructed, and 2D/3D analysis of the X-CT images was performed to investigate the texture and internal structure and to estimate the mean volume fractions of the metal inclusions. Also, X-CT analysis was conducted on three cubes before and after the uniaxial compressive experiments to examine crack propagation and fragmentation.

Uniaxial compression tests were performed at a displacement rate of 0.25 mm/min to maintain quasi-static conditions using the Instron 5985 load frame. Tests were accompanied by in-situ digital image correlation (DIC) to capture the displacement and strain evolution and were continued until the final failure of the samples. Experimental setups are detailed in Section §2.2.5. Although all samples were investigated using quasi-static compression experiments, the failure mechanism and fragmentation were analyzed from the samples that were free from premature failure.

3.3 Results and Discussion

The Viñales cubes exhibit a random distribution of irregularly shaped, bright-colored Fe-Ni metal grains embedded in a light-colored, irregularly fractured silicate matrix (Figure 25). X-ray intensity maps of Fe and Ni provide insight into the spatial distribution of kamacite and taenite (Figure 26. Additionally, major silicate-bearing minerals such as olivine, pyroxene, and plagioclase have been identified through the Mg, Al, and Si X-ray intensity maps. The samples have experienced a moderate level of shock, corresponding to shock stage 4 (Gattacceca et al., 2020; Yin and Dai, 2021). Analysis of backscattered electron (BSE) images has revealed the presence of multiple randomly oriented shock veins with sizes smaller than 1 mm, as well as two larger shock veins exceeding 3 mm in thickness. Furthermore, chondrule boundaries have been identified (Figure 25 and Figure 26). Various shock metamorphic features, including irregular fractures in silicate minerals like olivine and pyroxene, recrystallized metals and troilite, and numerous opaque shock melt veins, have been observed within the Viñales cube. The relatively round-shaped silicate minerals found in the shock veins suggest that they have undergone a recrystallization process.

3.3.1 Ultrasonic Characterization

Elastic wave velocity measurements were utilized to calculate the elastic properties of the Viñales meteorite by analyzing the electric pulse propagation characteristics through the samples. The process involved using an Olympus 5077 PR electric pulse generator/receiver to generate and amplify electric pulses sent to the transducers, as well as filter background noise for the received pulse. Normal and shear waves are then applied to the sample using Olympus V-110RM and V156-RM full contact transducers, respectively, which serve as actuator-sensor pairs. To minimize signal attenuation and enhance analysis accuracy, Olympus shear wave coupling fluid was applied to the surface of the transducer to reduce contact pressure on the meteorite surface. For this study, eight Viñales cubes were used. The PI-1042 Digital Acquisition system was employed for signal data processing and extraction of wave characteristics, which were used to compute the normal and shear wave velocities for the estimation of mechanical properties.

$$\nu = \frac{1 - 2\left(\frac{V_S}{V_L}\right)^2}{2 - 2\left(\frac{V_S}{V_L}\right)^2} \tag{3.1}$$

$$E = \frac{V_L^2 \rho (1 + \nu)(1 - 2\nu)}{1 - \nu} \tag{3.2}$$

$$G = {V_S}^2 \rho = \frac{E}{2(1 + \nu)} \tag{3.3}$$

Here, V_S and V_L are normal and shear wave velocity, E and G are elastic and shear modulus, ρ is the material density, and ν is Poisson's ratio.

Phenomenological equations are used to calculate the elastic properties; where the elastic longitudinal modulus along each direction (E) is represented by Eq. 3.1. The material symmetry of Viñales is considered isotropic as the wave velocity components along the principal directions of all the tested cubes are approximately the same. Therefore, the shear modulus (G) is computed based on isotropic linear elastic relations, as shown in Table 8. The average Young's modulus (E_{avg}) is determined to be 38 MPa, with G estimated at approximately 16.1 GPa and Poisson's ratio (ϑ) near 0.19.

Elastic wave velocities of meteorites depend on various factors, including material compositions, porosity, shock state, and degree of lithification (Greenberg and Castagna, 1992). As waves propagate through the cubes, variations in minerals and material heterogeneity can lower the wave velocities, resulting in lower elastic moduli. The presence of microcracks, porosity, and inter-grain boundaries in both metals and minerals act as points of weakness, further reducing the material's elastic modulus and inducing variability in strength, as evident in Figure 31. The amount of change in elastic wave velocities correlates with the crystal structure of minerals and pore morphology (Birch, 1961). For example, the meteorite Mount Tazerzait (L5), with a porosity of 17.2%, exhibits a longitudinal wave velocity of 2930 m/s and a shear wave velocity of 1870 m/s, while a low-porosity meteorite like Richfield (LL3), with a porosity of 1.8 ± 0.6%, exhibits a longitudinal wave velocity of 5110 m/s and a shear wave velocity of 2450 m/s (Britt and Consolmagno, 2003; Flynn et al., 1999). In L ordinary chondrites, the mean longitudinal wave velocity is reported as 3443 ± 1389 m/s, and the mean shear wave velocity is 2028 ± 787 m/s (Jones, 2009). It is observed that elastic wave velocities tend to decrease with increasing porosity, while they increase with the increase in bulk density of the meteorite.

In addition to preexisting flaws like porosity strongly influencing elastic wave velocities, there could be other factors at play, such as the presence of shock-melt veins in the meteorite cubes. Viñales meteorite shows randomly oriented shock melt veins, with sizes mostly <1 mm and a few >3 mm. These shock-melt veins are part of the meteorite's metamorphic history and can cause variations in elastic wave velocities by altering the composition of minerals and metals and/or by decreasing the overall porosity (Hons and Hildebrand, 2004).

Table 8. Mechanical Properties of Eight Viñales Cube using Elastic Wave Velocity Measurements*.

Cube no.	Normal velocity, $V_N\ (m/s)$	Shear velocity, $V_S(m/s)$	Elastic modulus, $E\ (GPa)$	Shear modulus, $G\ (GPa)$	Poisson's ratio, ν
V-1	3515.25	2210.85	37.8	16.2	0.17
V-3	3674.18	2330.61	41.0	17.6	0.16
V-4	3646.14	2239.26	39.7	16.6	0.20
V-5	3510.40	2117.31	35.5	14.7	0.21
V-10	3649.53	2243.07	39.5	16.7	0.19
V-11	3452.13	2073.11	34.8	14.4	0.21
V-13	3751.36	2320.99	43.0	18.1	0.19
V-14	3348.84	2085.18	33.2	14.1	0.18
Mean	3568.23	2202.17	38.0	16.1	0.19
SD	125.24	94.05	3.1	1.4	0.01

* (Hamza et al., 2023)

3.3.2 Microstructural Characterization

The microstructure of Viñales was analyzed using a field-emission electron microprobe analyzer (EPMA) equipped with a wavelength dispersive spectrometer (WDS). Backscattered electron (BSE) images show three dominant phases (Figure 26a). The first phase is the silicate matrix, which is a brittle component primarily composed of olivine, pyroxene, and feldspar. The second phase is the shock melt vein, formed during extraterrestrial impact events, and composed of fragments of matrix, troilite, and chromite minerals. Lastly, the metal and sulfide grains are randomly distributed throughout the matrix phase and at the interface of the shock melt vein.

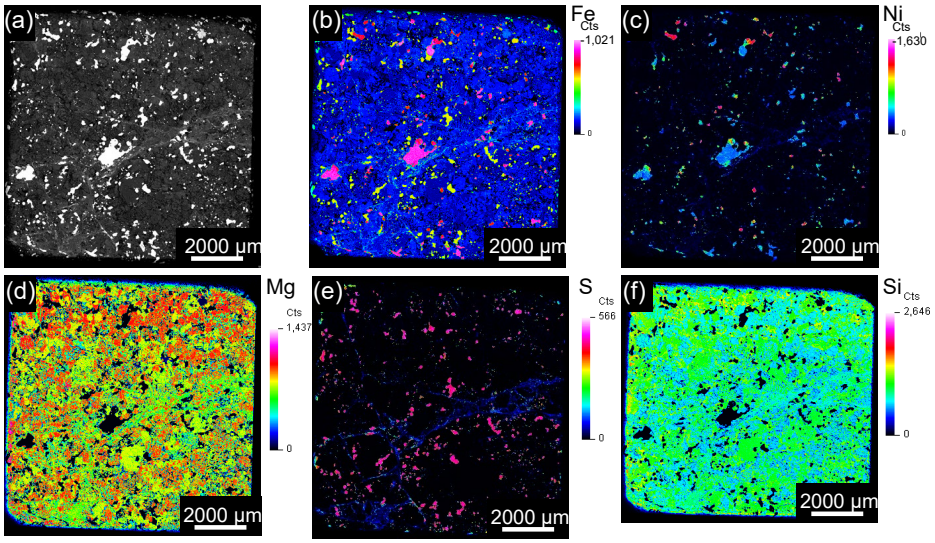

Figure 26. (a) BSE Image of a Typical Viñales Cube Showing the Distribution of Silicates, Which Is Black in the Image, Grey Which Is the Shock Vein, and Bright Which Are Metals and Sulfides. X-ray Intensity Maps of (b) Fe, (c) Ni, (d) Mg, (e) S, and (f) Si from the EPMA Show the Distribution of Minerals and Metals.

X-ray intensity maps were generated using WDS to analyze the primary elements in the meteorite – Fe, Ni, Mg, S, and Si. The Fe X-ray intensity map shows the highest concentrations

in the metals (pink), medium concentrations in the sulfides (lime green), and lowest in the silicates (blues) (Figure 26b); the pink and lime green correspond to the bright phases in the BSE image (Figure 26a). Within the metal grains, there is a gradient of Fe concentrations, indicating the presence of different metal phases. Figure 26c displays a Ni X-ray intensity map, where Ni is primarily distributed in the metals: light blue corresponds to kamacite, whereas lime green and red represent different taenite and plessites phases. These images show that the metal is dominated by kamacite and smaller sub-grains of Ni-rich taenite. Taenite has a face-centered cubic (FCC) crystal structure with abundant dislocation slip at lower critical resolved shear stress compared to kamacite, which has a body-centered cubic (BCC) structure with complex dislocation cores. The distribution of S and average Fe levels (indicated in yellow in Figure 26b) indicates a strong overlapping Fe and S signal (Figure 26e), coming from the distribution of troilite. The Mg X-ray intensity map (Figure 26d) shows the distribution of Mg, which, together with Fe and Si, shows the distribution of olivine and pyroxene. Finally, the bulk of the meteorite is Si-rich (Figure 26f), reflecting its dominant silicate nature.

As a result of thermal metamorphism on the parent body, most chondrules are largely recrystallized and integrated with the matrix (Figure 26). The mineralogy, its elemental composition, and overall texture are consistent with a type 6 ordinary chondrite. In this type of chondrite, the metamorphic temperature refers to the equilibrium temperature at which coexisting mineral phases reach diffusive equilibrium. At this temperature, the boundary of the chondrule begins to disappear. The heat of thermal metamorphism alters the mineral texture and composition and may arise from the energy released during collisions, radioactive decay (such as ^{26}Al and ^{60}Fe), and electromagnetic inductions (Huss et al., 2006; Rubin, 1997). This thermal metamorphism leads to the equilibration of olivine and pyroxene, resulting in more chemically homogeneous silicate minerals. X-ray intensity maps obtained from the

wavelength-dispersive spectroscopy (WDS) analysis of the Viñales cube show that the majority of minerals are silicates, along with metals and sulfides.

3.3.3 Porosity and Pore Size Distribution

In addition to characterizing the different microstructure phases, it is crucial to identify the shape and size of microstructure flaws to understand the deformation mechanism and brittle failure of Viñales meteorite samples. These stony meteorites are inherently brittle, and the nucleation, growth, and interactions of micro-cracks control their inelastic deformation and failure. Upon mechanical loading, pores coalesce and form micro-cracks that propagate through the brittle phases, resulting in abrupt fracture. To accurately model brittle fracture, a high-fidelity representative volume element that includes flaw distribution is needed as the foundation for comprehensively understanding the mechanical behavior of the meteorite. Therefore, the N_2 gas pycnometer is utilized to measure bulk porosity, and the Brunauer-Emmett-Teller (BET) method is employed for adsorptive characterization to extract porosity features.

Six cubes were selected for analysis using the N_2 gas pycnometer to determine the bulk porosity of the Viñales meteorite. The bulk density of the cubes was calculated by measuring their mass and bulk volume, while the true density was measured using the Anton Paar Ultrapyc 5000 N2 gas pycnometer. Before conducting the experiments, the testing equipment was calibrated using a standard steel calibration sphere provided by Anton Paar.

To ensure precise measurements and maintain a measurement variance below 0.2%, true density measurements were repeated ten times for each cube. The porosity of the cubes was then calculated using Equation 2.4. Table 9 presents the porosity measurements of the six Viñales cubes, which ranged from 6.49% to 4.00%, with an average porosity of 5.66%. These

values fall within the range of porosity values observed in L ordinary chondrites, as reported in studies by Britt & Consolmagno (2003) and Consolmagno et al. (2008). For a more detailed investigation of porosity and to understand their variation, two cubes were selected for further analysis: V-3 with a porosity of 6.49%, and V-13 with a porosity of 4%. These cubes were examined using the X-CT technique.

The highest porosity observed in our Viñales cube V-3 was 6.49%, with corresponding longitudinal and shear wave velocities measured as 3674 m/s and 2330 m/s, respectively. On the other hand, the lowest porosity of 4.0% was measured in cube V-13, which exhibited longitudinal and shear wave velocities of 3751 m/s and 2320 m/s, respectively. The results show a weak correlation between slight changes in porosity and elastic wave velocities in the Viñales cubes. Although more cubes need to be tested to establish such a relation, the results of these two cubes suggest other factors such as mineral composition, and material heterogeneity may contribute to the variability of the measurements.

Published data shows that the shock state of ordinary chondrites does not have a significant influence on their porosity (Consolmagno et al., 2008; Consolmagno S.J. et al., 1998). However, it is worth noting that highly porous meteorites tend to exhibit lower strength and reduced thermal and electrical conductivity (Soini et al., 2020). Furthermore, porosity plays a critical role in understanding the evolution of parent bodies during the early solar system, as well as their fragmentation and catastrophic disruption during impact events.

Table 9. Porosity Measurement of Six Viñales Cubes using N_2 Gas Pycnometry.

Cube no.	Volume (cc)	Mass (g)	Avg. bulk density (g/cc)	Avg. grain density (g/cc)	Porosity (%)	Ultimate Strength (MPa)
V-3	1.02	3.33	3.27	3.50	6.49	110.52
V-5	1.00	3.31	3.29	3.52	6.40	119.30*
V-10	1.02	3.41	3.34	3.57	6.41	136.47
V-11	1.01	3.41	3.36	3.51	4.29	118.95
V-13	1.01	3.43	3.39	3.53	4.00	134.41
V-14	1.01	3.32	3.29	3.51	6.36	86.19**
Mean	1.01	3.37	3.32	3.52	5.66	117.64
SD	0.01	0.05	0.04	0.02	1.07	16.73

*V5 – Compression test was interrupted for X-CT analysis
**V14 – Damaged sample

The specific surface area of pores was measured using the Brunauer Emmett and Teller (BET) N_2 technique, and the pore size distribution was calculated by the Barrett-Joyner-Halenda (BJH) method at 77 K using a Micrometrics Tristar II 3020 surface area and porosity analyzer. The BET test uses nitrogen as the adsorbate at 77 K to determine the specific surface area and pore volume (Sing, 1998). Pores are classified according to the International Union of Pure and Applied Chemistry (IUPAC) recommendations. Nanopores have a pore size of less than 2 nm, mesopores have a pore size between 2-50 nm, and macropores have a pore size greater than 50 nm (Kuila and Prasad, 2013; Rouquerol et al., 1994).

Figure 27 shows the gas adsorption and desorption isotherms, pore volume, and pore area of two Viñales fragments. The isotherms represent the amount of gas adsorbed as a function of relative pressure (P/P_0), where P is the absolute equilibrium pressure, and P_0 is the condensation pressure. The isotherms display low adsorption at a lower relative pressure ($P/P_0<0.02$), followed by a plateau region indicating a variety of mesopores, such as fine mesopores and large mesopores. The hysteresis loop associated with capillary condensation

and evaporation occurs at high relative pressure, with isotherms showing a convex shape at high relative pressure (P/P_0>0.8).

The Viñales fragments exhibit a hysteresis loop similar to the type IV isotherm; however, they lack a plateau region at high relative pressure, indicating a classification as a type IIB isotherm with a type H3 hysteresis pattern (Rouquerol et al., 1994). The adsorption and desorption isotherms provide information about the porous structure of the fragments. The presence of a steep slope at a high relative pressure (P/P_0) in the range of 0.9 to 1.0, instead of a plateau region seen in type IV isotherms, suggests the presence of macropores in the fragments. The H3 hysteresis pattern further indicates the existence of slit-like pores. The desorption branch of the isotherm exhibits a forced closure at $4 < P/P_0 < 5$, indicating the presence of small mesopores within the fragments (Figure 27a and Figure 27b).

The BET surface area and adsorption pore volume are reported in Table 10. The results reveal an average specific surface area of 0.927 m^2/g and an average single-point adsorption pore volume of 2.53×10^{-3} cm^3/g. The pore size distribution of the Viñales fragments exhibits a bimodal distribution, with a major peak between 100 to 140 nm. Additionally, a few pores larger than 140 nm are present in the fragments, as indicated by the rapid decrease in dV/dlog (w) (Figure 27c and Figure 27d). Furthermore, the pore area distribution (dA/dlog (w)) shows a unimodal distribution with a peak pore size ranging from 6 nm to 40 nm (Figure 27e and Figure 27f). Pores with diameters ranging from 3 nm to 50 nm can be attributed to intra-tachoid porosity or fine mesopores, representing the pore space within tachoids formed by turbostatic stacking. Pores with sizes from 50 to 100 nm can be attributed to intertactoid or intra-aggregate porosity, i.e., large mesopores and fine macropores. Pore sizes larger than 200 nm were unable to be characterized as N_2, as an adsorbent, is limited in measuring sizes over 200 nm.

Table 10. Adsorptive Pore Characterization for Viñales Ordinary Chondrite using the N_2 BET Method*.

Samples no.	Mass (g)	BET surface area (m^2/g)	Adsorption pore volume (cm^3/g)
1	0.3845	0.8801	0.002661
2	0.3036	0.8323	0.002402
3	0.2491	0.9047	0.002406
4	0.2597	0.9608	0.002705
5	0.2137	1.0587	0.002455
Mean	0.28212	0.92732	0.0025258

*(Hamza et al., 2023)

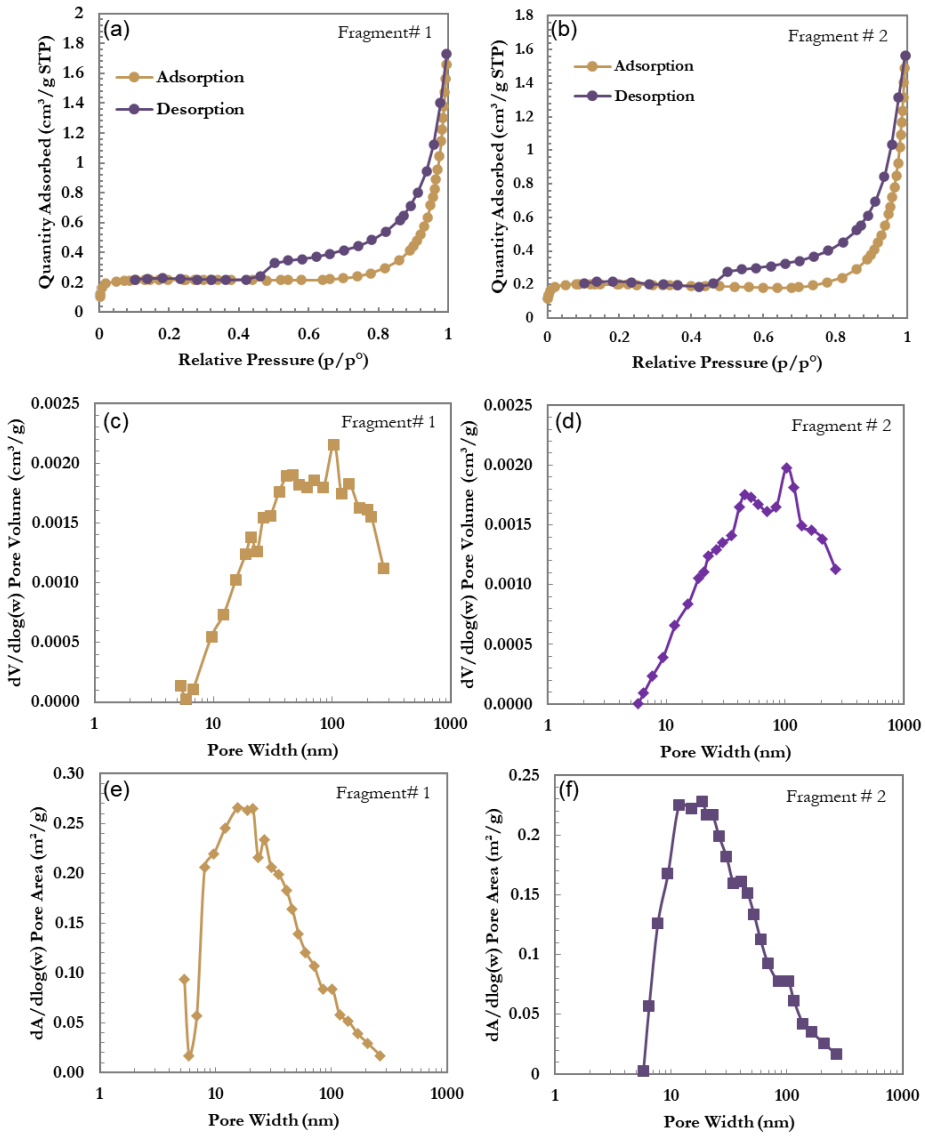

Figure 27. BET Surface Area and Pore-size Analysis for Two Viñales Fragments Show (a-b) Adsorption and Desorption Linear Isotherms Indicating the Quantity of N_2 Adsorption and Desorption per unit Mass at a Temperature of 77.35 K. The Shape of the Isotherms Suggests the Presence of Fine Mesopores, Larger Mesopores, and Micropores in the Viñales Fragments. (c-d) BJH Pore Volume Obtained from the N_2 Isotherm Shows a Bimodal Distribution with a Major Peak Between 100 – 140 nm, while (e-f) BJH Pore Area Obtained from the N_2 Isotherm Shows a Unimodal Distribution with a Major Peak Between

6 – 40 nm. The Halsey-Faas Correction Has Been Applied to Both Pore-volume and Pore-size Measurements.

3.3.4 3D Structural Characterization

A non-destructive structural analysis was conducted using X-ray computed tomography (CT) scans to generate a 3D volumetric density map of high-density phases, specifically Fe-Ni metal. The CT scans were performed using a 6-positioned integrated filter: Al 0.5 mm + Cu 0.038 mm, with a resolution of 4 μm per pixel and a rotation of 360 at a 0.15^0 step. The acquired X-CT images were reconstructed using the NRecon software provided by the Bruker system. Reconstructed images underwent beam hardening correction, ring artifact reduction, and smoothing.

The CTAn software from the Bruker system was utilized to analyze various features, including the volume fraction and morphological characteristics of Fe-Ni. A mean denoise filter was applied to the grayscale reconstructed images, and binary images of Fe-Ni were obtained by segmenting the grayscale images at a threshold level calculated from the BSE image in correlation with the WDS elemental images. Different minerals exhibit distinct X-ray transmission capabilities, resulting in varying distributions of grayscale levels ranging from 0 to 255.

Figure 28 presents the X-CT results for cubes V-3 and V-13. The morphometry analysis of the V-3 cube revealed a Fe-Ni volume fraction of 1.6%. The fractal dimension was estimated as 2.36, with a total number of 11,650 Fe-Ni particles, and the structural thickness of Fe-Ni ranged from 0.02 to 0.7 mm. The X-CT analysis of cube V-13 showed a volume fraction of 2.2% for the metal and a fractal dimension of 2.41. This cube contained 18,497 Fe-Ni particles with a structural thickness varying from 0.02 mm to 0.7 mm.

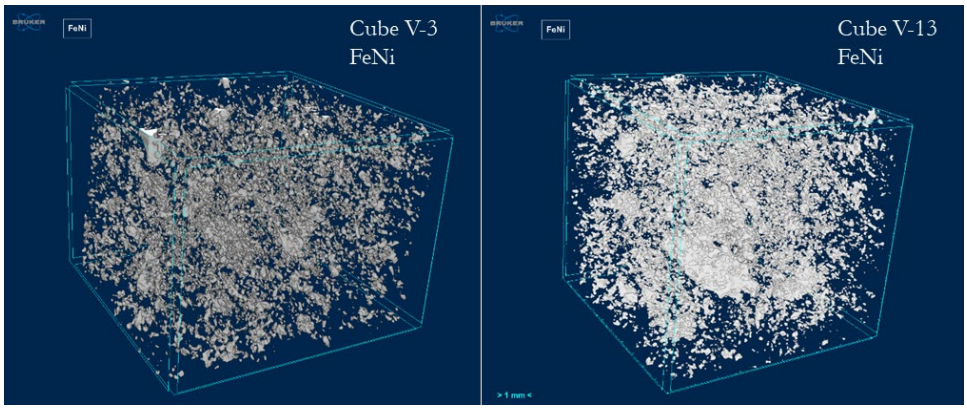

Figure 28. X-ray CT Analysis of Viñales Cubes (V-3 and V-13) Using the Bruker Skyscan 1272 X-ray Tomograph. Grayscale Tomography Images Were Used to Segment the Fe-Ni by Applying Threshold Values for Fe-Ni. This Threshold Value Was Obtained by Correlating the X-CT Images with the BSE and WDS Elemental Images. Quantitative and Qualitative Analysis Was Performed on These Segmented Data to Obtain Metal Distribution and to Analyze Its Structure and Morphology. The Resulting Distribution Is Shown in a 3-D Reconstructed Volume of Fe-Ni in White Color.

3.3.5 Quasi-Static Compressive Strengths

Quasi-static compression tests were conducted to investigate the strength, stiffness, toughness, and strain-to-failure characteristics of the Viñales meteorite. Fourteen cubes were prepared and tested with uniaxial compression accompanied by Digital Image Correlation (DIC) (Table 11). An interrupted compression test was performed on cube V-5 to study crack propagation during the initial peak in its stress-strain curve. X-CT was utilized to examine the crack initiation site and the impact of minerals, such as troilite and matrix, on crack propagation within cube V-5. Among the compression experiments conducted, premature failure occurred in five cubes (V-1, V-6, V-7, V-8, and V-14). Compressive stress and strain values were determined using the initial geometry of the cubes. Figure 29a illustrates a typical

stress-strain response, with strain calculated from DIC measurements and stress derived from the measured load and cross-sectional area of the cube. The DIC strain exhibited unstable local strain when the stress reached the ultimate stress, resulting in abrupt failure. Therefore, the stress-strain response of the DIC measurements is presented only until the ultimate stress (Figure 5a). The elastic modulus, calculated as 33.3 GPa, was determined from the slope of the linear section of the stress-strain response using the least-squares method.

Table 11. Physical Properties and Ultimate Compressive Strength of 14 Viñales Cubes

Cubes no.	Avg. L(mm)	Avg. W(mm)	Avg. T(mm)	Vol (cc)	Mass (g)	Density (g/cc)	UCS (MPa)	Comments
V-1	9.91	9.85	9.69	0.95	3.34	3.53	59.47	PF
V-2	10.10	10.08	10.00	1.02	3.63	3.57	133.26	
V-3	10.06	10.04	10.08	1.02	3.33	3.27	110.52	
V-4	10.18	10.08	10.12	1.04	3.32	3.20	187.76	
V-5	10.01	10.00	10.03	1.00	3.31	3.29	119.30	IT
V-6	10.06	10.04	9.94	1.00	3.29	3.28	71.23	DM
V-7	10.04	9.98	10.03	1.01	3.32	3.31	42.33	PF
V-8	9.97	9.97	9.87	0.98	3.19	3.25	66.70	PF
V-9	10.10	10.08	10.06	1.02	3.44	3.36	*	DM
V-10	10.07	10.06	10.07	1.02	3.41	3.34	136.47	
V-11	10.06	10.03	10.05	1.01	3.41	3.36	118.95	
V-12	10.06	10.03	10.06	1.02	3.39	3.34	135.54	
V-13	10.07	10.01	10.05	1.01	3.43	3.39	134.41	
V-14	10.01	10.03	10.06	1.01	3.32	3.29	86.19	DM
Mean	10.05	10.02	10.01	1.01	3.37	3.34	107.86	
SD	0.05	0.06	0.11	0.02	0.10	0.10	38.95	
Mean excluding damaged samples							136.70	

UCS – Ultimate compressive strength
PF – Premature failure during the compression test
IT – Test interrupted for X-ray microcomputed tomography
DM – Damaged samples
* Compression test not performed on damaged sample V-9

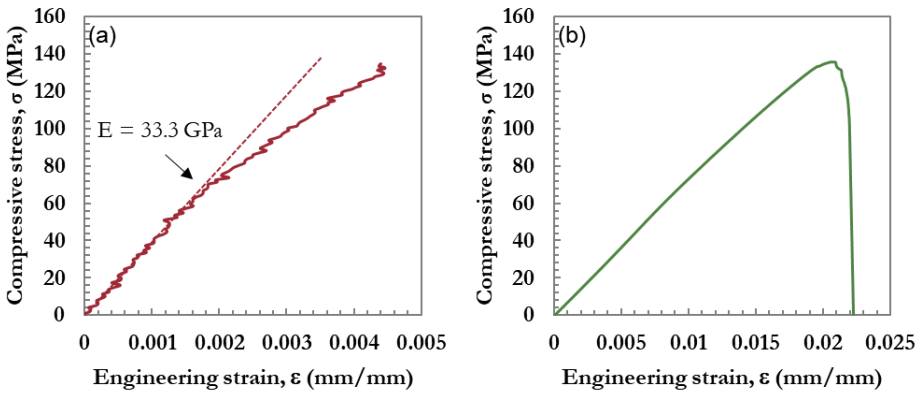

Figure 29. Engineering Stress and Strain Responses of a Viñales Cube (V-12) at a Displacement Rate of 0.25 mm/min. In (a) the Strain Was Obtained from the DIC Measurements and Elastic Modulus Was Calculated from the Slope of the Linear Section of the Plot Shown as a Dotted Line. In (b) Strain Was Obtained from the Cross-head Displacement of the Instron Machine Without Machine Compliance Correction. This Plot Was Used to Analyze the Failure Response Instead of Measuring the Elastic Modulus of the Sample.

The stress-strain response from cross-head displacement was analyzed for all thirteen cubes (Figure 30 and Figure 31). The average density of the thirteen cubes was measured as 3.34 g/cc, which overlaps with the L ordinary chondrite (Britt and Consolmagno, 2003). All thirteen samples exhibited brittle behavior in their stress-strain response and demonstrated similar failure modes under compressive load. However, the results showed variability in the strength data, with the ultimate compressive strength ranging from 110.52 MPa to 187.76 MPa, with a mean of 136.7 MPa (excluding the damaged cubes as noted in Table 11). This variability can be attributed to the complex mineralogy, heterogeneous microstructure, and the presence of microstructural defects such as microcracks, voids, nano-, and micro-porosity in the meteorites (Flynn et al., 2018; Ostrowski and Bryson, 2019). Additionally, variations in

mineral volume fractions, particularly in the Fe-Ni phase within the samples, may contribute to the observed strength variations (Figure 26).

Similar variations in compressive strength have been observed in ordinary chondrites, with reported values ranging from 20.00 MPa (Elenovka) to 456 MPa (Tsarev) (Cotto-Figueroa et al., 2016; Medvedev et al., 1985; Molesky et al., 2015; Ostrowski and Bryson, 2019; Slyuta, 2017; Zotkin et al., 1987). For the L6 ordinary chondrites, the compressive strength varies from 82.9 MPa (Ness County 1894) (Buddhue, 1942) to 265 MPa (Kunashak) (Medvedev et al., 1985). Notably, a much higher quasi-static compressive strength of 1100 ± 250 MPa has been reported for the Novato N01 L6 ordinary chondrite, which the author attributed to irregular loading of the surface area (Jenniskens et al., 2014).

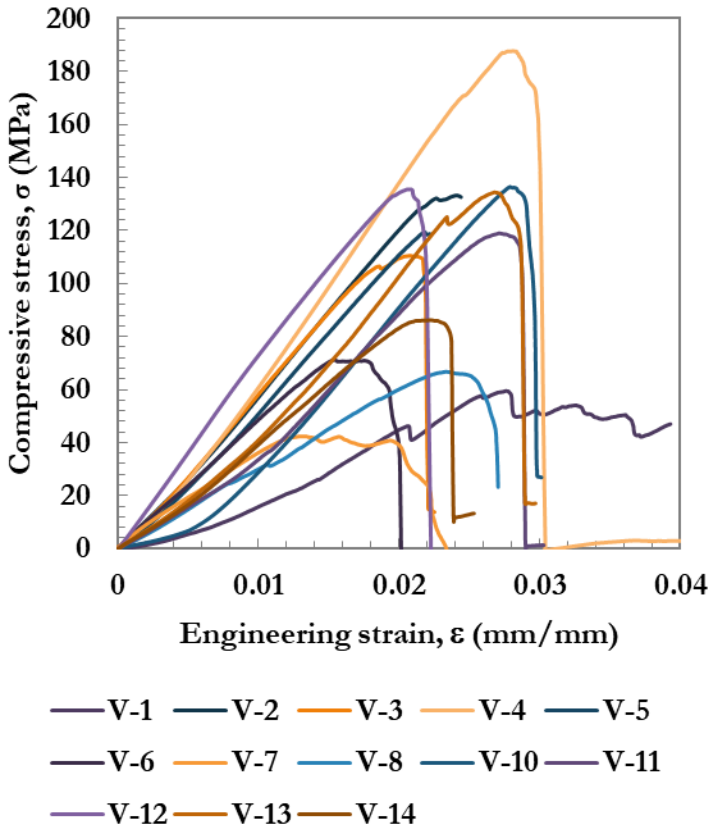

Figure 30. The Engineering Stress and Strain Responses of Thirteen Viñales Cubes at Ambient Temperature Exhibit a Wide Range of Compressive Strengths. Engineering Strain is Calculated from the Cross-Head Displacement of the Instron Test Frame. Cube V-9 Was Damaged During Sample Preparation and Hence Not Shown. This Plot Shows All Results, Including the Five Cubes That Failed Prematurely During Uniaxial Compression Experiments.

Previous research on ordinary chondrites has demonstrated a strong correlation between porosity and compressive strength (Flynn et al., 2018; Medvedev et al., 1985; Ostrowski and Bryson, 2019; Tsvetkov and Skripnik, 1991). For instance, low-porosity ordinary chondrites like La Lande (L5) with a porosity of 2.9% exhibit a compressive strength of 420.5 MPa (Blum et al., 2006; Ostrowski and Bryson, 2019), while Aba Panu (L3), with a porosity of 3.8%, shows a compressive strength of 438.4 MPa (Rabbi et al., 2021, 2021). In contrast, ordinary chondrites with above-average porosity, such as Holbrook (L/LL6) and Elenovka (L5), with porosities of 10.9% and 10.5% respectively, display compressive strengths of 63 MPa and 20 MPa (Britt and Consolmagno, 2003).

Further investigation was conducted to establish a correlation between the mechanical behavior and porosity of the Viñales cube under compressive loading. Six randomly selected cubes were analyzed, and their porosity was measured using an N_2 gas pycnometer. The compressive of the six cubes was then correlated with their respective porosity values (Figure 31). The cube with the highest porosity, V-3 (6.49%), exhibited an ultimate compressive strength of 110.52 MPa. Conversely, the cube with the lowest porosity, V-13 (4.0%), exhibited an ultimate compressive strength of 134.41 MPa. Interestingly, cube V-10, with a porosity of 6.41%, displayed the highest ultimate compressive strength of 136.47 MPa in the quasi-static compressive experiments. These findings suggest that although porosity can contribute to

material weakness and failure initiation, the compressive strength of the Viñales cubes appears to be relatively independent of minor changes in porosity (Figure 31a).

Furthermore, when considering the densities of the cubes, cube V-13 exhibited relatively high bulk and true densities of 3.39 g/cc and 3.53 g/cc respectively, while cube V-3 had a bulk density of 3.27 g/cc and a true density of 3.50 g/cc. The strongest cube, V-10, on the other hand, displayed the highest true density of 3.57 g/cc among all the tested cubes. Therefore, the relationship between compressive strength and true density suggests that the complex textural and compositional variations in metals and minerals may be responsible for the observed strength variations in the material (Figure 31b).

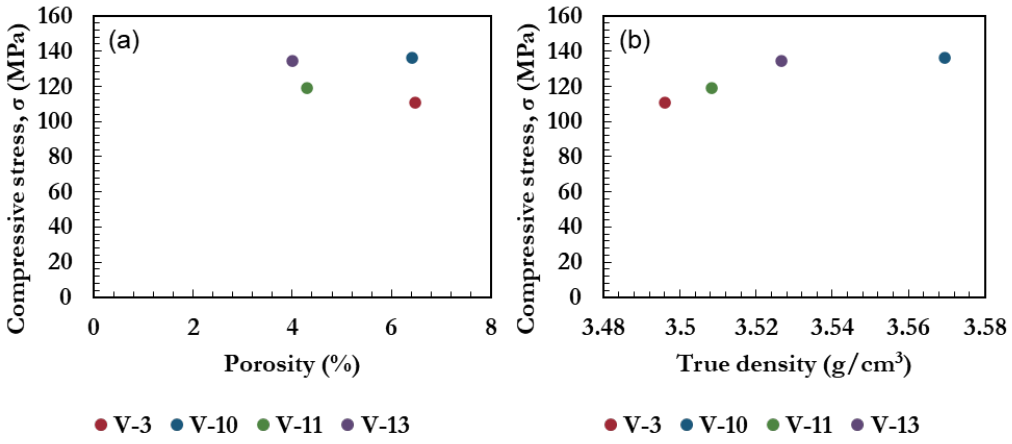

Figure 31. Variation in Compressive Strength of Viñales Cubes (V-3, V-10, V-11, and V-13) With Minor Change in (a) Porosity and (b) True Density Illustrate No Significant Relationship. Cube V-5 and V-14 were Excluded from The Analysis Because They Were Damaged During Tests as Mentioned in Table 11.

3.3.6 Failure analysis

The Vinales cubes exhibited brittle failure under quasi-static compressive loading, similar to other ordinary chondrites (Cotto-Figueroa et al., 2021; Kimberley and Ramesh, 2011; Rabbi

et al., 2021). Failure initiation likely occurs from a single crack that originates from preexisting flaws and propagates through the silicate phases and/or grain boundaries of metals and minerals. Figure 32 and Figure 33 illustrate optical images of a pristine cube and a crushed cube from a top-view orientation, highlighting the region of crack initiation. At low stresses (<20 MPa) and strains (<0.01), the cubes display a low elastic modulus associated with crack closure phenomena (Figure 30). As the stress increases, the cubes undergo deformation, reducing in length and increasing in width under compressive loading, as evidenced by the linear section of the stress-strain response, known as the elastic region. No perceptible cracks were observed in the DIC results corresponding to the elastic region.

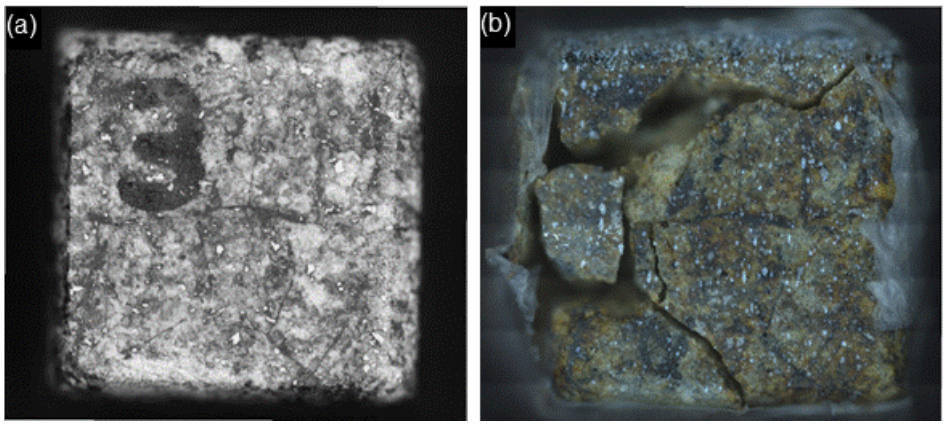

Figure 32. Optical Image of a 1-cm Viñales Cube (V-3) along the Axial Direction from a Top-view Orientation, showing (a) Cube Before Compression and (b) After Compression. The Tested Sample Shows Complex Crack Networks That Propagated Through the Most Brittle Phase, Despite the Presence of Shock Melt Veins During the Uniaxial Compression Experiment.

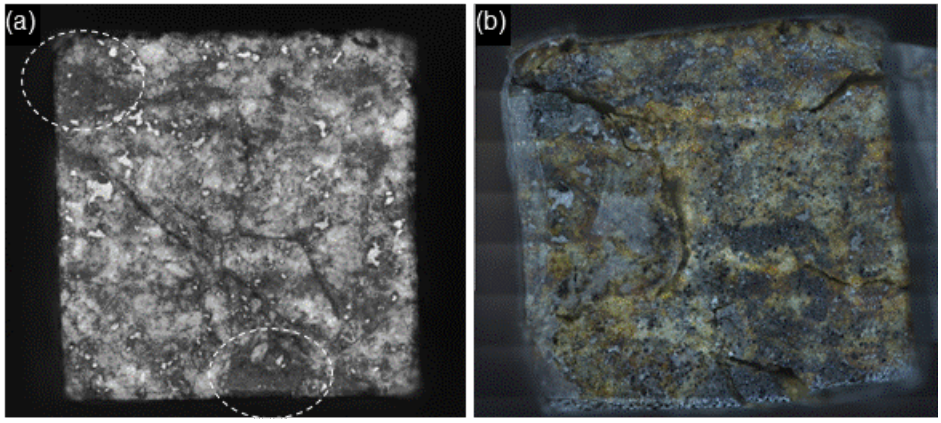

Figure 33. Optical Image of a 1-cm Viñales Cube (V-13) Taken along the Axial Direction from a Top-view Orientation Shows (a) Cube Before Compression and (b) After Compression. The Tested Sample Shows the Location of Crack Initiation from the Dark Silicate Phase as Marked by White Circle and Crack Paths.

With further increase in load, the compressive stress approaches the ultimate compressive stress, and crack begins to originate from the preexisting flaws. As the stress continues to increase, multiple cracks appear, connecting through the weakest regions of the sample. The coalescence of adjacent cracks facilitates the development of complex crack networks under a compressive load that rapidly propagates, causing axial splitting and brittle failure.

Axial splitting failure during compressive loading in brittle materials is commonly attributed to the initiation and propagation of wing cracks (Kimberley and Ramesh, 2011; Nemat-Nasser and Horii, 1982; Paliwal and Ramesh, 2008). When a primary crack originates from preexisting flaws, the stress concentration at its tip increases with the applied load. This elevated stress concentration promotes the formation of wing cracks, which develop radially and align parallel to the principal stress direction. The presence of wing cracks intensifies the stress concentration effect, leading to the accelerated propagation of cracks. As the main crack continues to propagate, it interacts with the growing wing cracks, causing them to extend and

connect with adjacent wing cracks. This process gives rise to a complex network of interconnected cracks within the material. Ultimately, the progression of these wing cracks culminates in axial splitting failure, where the material fractures along the axial direction.

3.3.7 Three Dimensional (3D) Digital Image Correlation

The deformation and fragmentation of the cubes under quasi-static compressive loading were further analyzed using the 3D-DIC system. Prior to each experiment, the ARAMIS 5M DIC system was calibrated using CQ15x12 calibration cubes. A stochastic black-and-white speckle pattern was applied to the surface of the cube, and the DIC system tracked the local displacements of these speckles. The tracked displacements were then used to calculate the deformation gradient tensor (F), displacement gradient tensor (GradU), and linearized Cauchy strain tensor (ε) using Equations 3.4-3.7:

$$F = Gradx \tag{3.4}$$

$$GradU = F - I \tag{3.5}$$

$$E = \frac{1}{2}(F^T F - I) = \frac{1}{2}(GradU GradU^T + GradU + GradU^T) \tag{3.6}$$

$$\varepsilon = \frac{1}{2}(\mathrm{Grad}U + GradU^T) \tag{3.7}$$

Here, x represents the position vector of each speckle, I is the identity second-order tensor, and E is the Green-Lagrange strain tensor. By neglecting the second-order terms, the Cauchy strain tensor is expressed as shown in Equation 3.7.

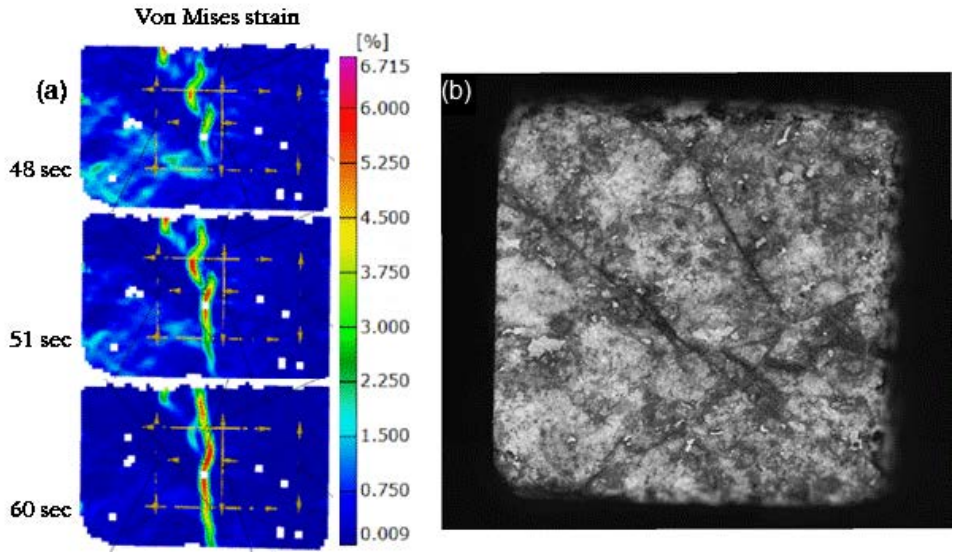

Figure 34. (a) The von Mises Strain Contour of Viñales Cube V-3 Obtained from Digital Image Correlation Measurements, Shows the Evolution of Crack Initiation, Coalescence, and Propagation Leading to Axial Failure. (b) An Optical Image of the Same Face of the Cube Is Shown. Three Horizontal and Vertical Virtual Extensometers, Indicated by Yellow Arrows in the von Mises Contour, Were Used in the DIC Measurement to Calculate Displacement and Strain.

While maximum principal strain, also called Mohr's theory, is commonly used as a failure criterion for brittle materials, this study employed the von Mises failure criterion provided by the ARAMIS software for the Vinales cubes. The advantage of using von Mises, particularly for studying meteorite cubes, is that it considers both the principal and shear strain components and provides a scaled numerical value suitable for identifying crack nucleation, growth, and propagation. Figure 34a displays the evolution of von Mises strain contours, indicating the location of maximum strain near the ultimate stress. High localized strain, observed at 48 s for cube V-3, corresponds to crack nucleation, followed by rapid crack growth leading to axial splitting failure at 60 s. The optical image of the exact cube shown in Figure

34b reveals shock features and a complex microstructure. Comparing the von Mises strain contours with the corresponding micrograph reveals that crack growth does not follow the shock melt vein but rather occurs in the weakest zone formed by the coalescence and growth of wing cracks.

The axial splitting failure mode of the other Vinales cubes is depicted in Figure 35 and Figure 36. A region of interest was selected to compute the von Mises strain from the stochastic speckle pattern. The high quality of the speckles was highlighted by the green region, and the corresponding von Mises strain contours are shown in the respective DIC contour images. All cubes exhibited splitting along the axial strain direction as a result of wing crack growth. By overlaying the von Mises strain contours onto the cubes, a correlation between localized von Mises strain and crack nucleation and growth path was established.

Vinales cubes V-2, V-5, and V-10 displayed a single axial splitting failure mode, while cubes V-11, V-12, and V-13 exhibited multiple axial splitting failures. When comparing the single and multiple axial splitting failure modes with physical properties such as density, porosity, and ultimate compressive stress, no significant correlation was found. This suggests that material heterogeneity, complex microstructure, and compositional variation in minerals and metals play a critical role in the formation of the complex crack network.

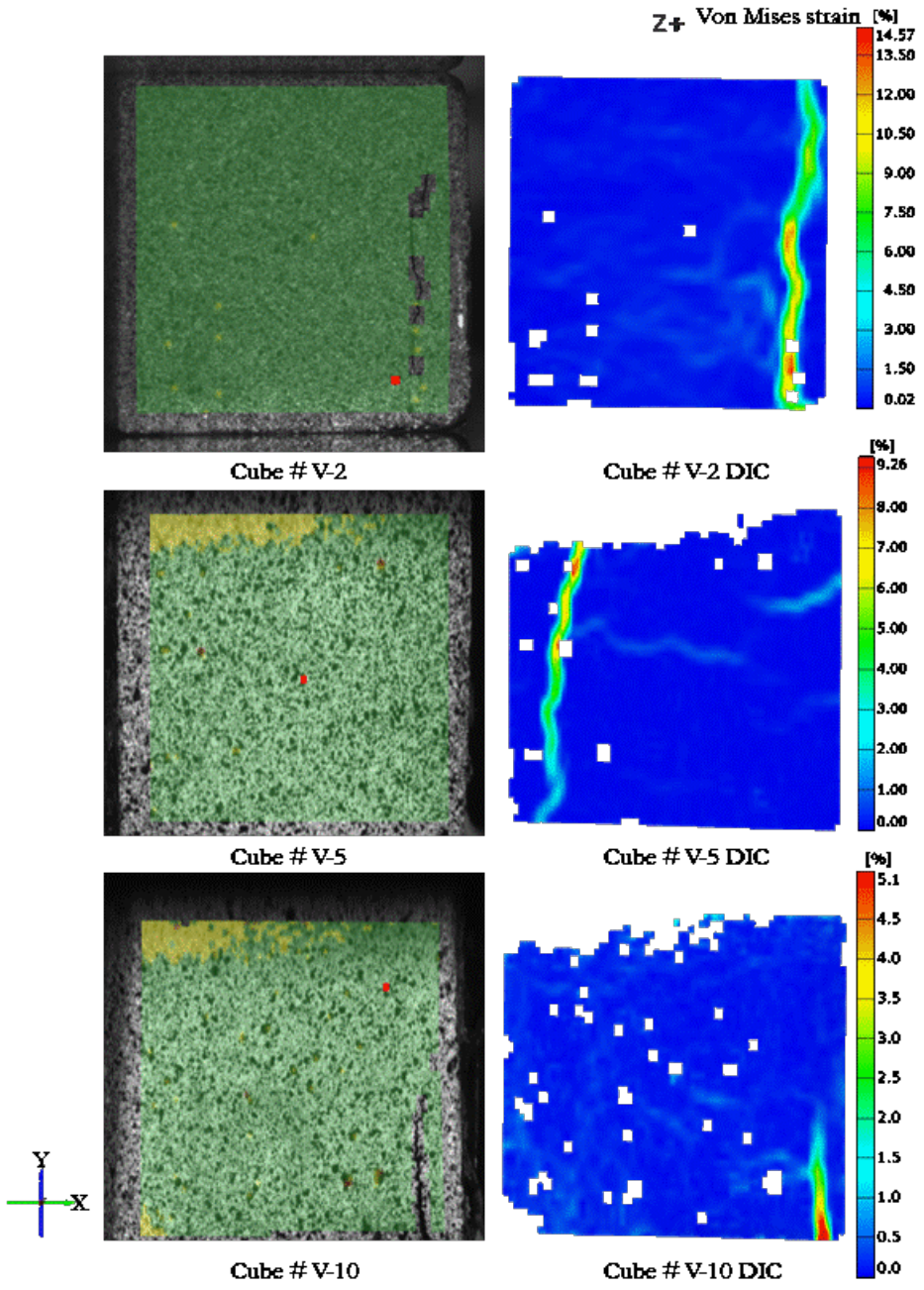

Figure 35. The DIC Analysis of Viñales Cubes (V-2, V-5, and V-10) Shows (a) the DIC Speckle Pattern, the Selected Region of Interest (ROI) Shown in Green Used to Compute the Displacement and Strain, and the Axial Splitting Crack, and (b) the von Mises Strain Contour Displaying the Location of High Strain and the Corresponding Location of Crack Initiation and Propagation of Those Cubes. The Yellow Region in the ROI and White Boxes

in the Strain Contour Indicate Spots of Low-quality Speckle Where the DIC Technique Was Unable to Compute the von Mises Strain. The Brittle Silicate Phase of the Cube Dominates the Location of Axial Splitting Leading to Final Brittle Failure.

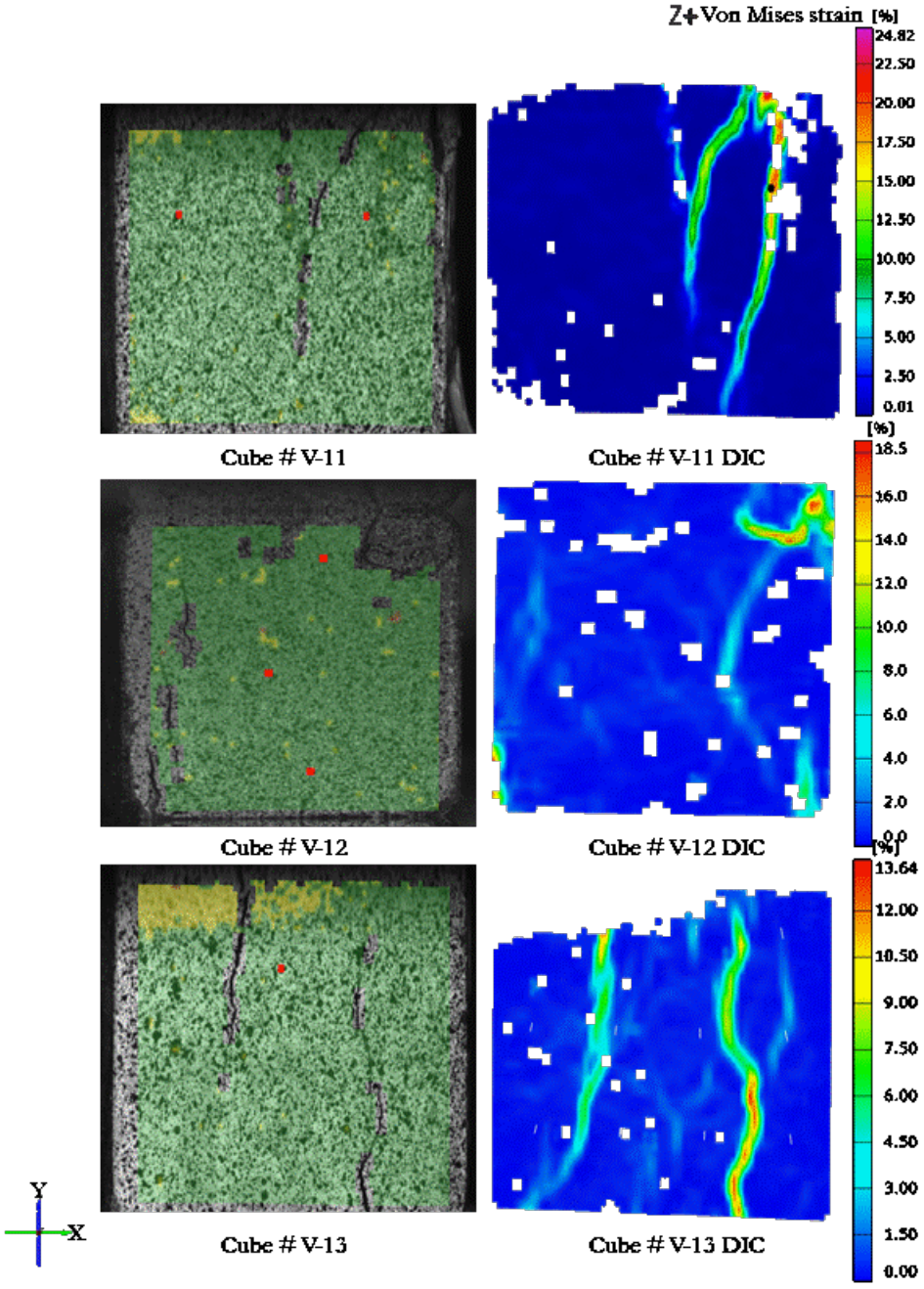

Figure 36. The DIC Analysis of Viñales Cubes (V-11, V-12, and V-13) Shows (a) the DIC Speckle Pattern, the Selected Region of Interest (ROI) Shown in Green Used to

Compute the Displacement and Strain, and the Axial Splitting Crack, and (b) the Von Mises Strain Contour Displaying the Location of High Strain and the Corresponding Location of Crack Initiation and Propagation of Those Cubes. The Yellow Region in the ROI and White Boxes in the Strain Contour Indicate Spots of Low-quality Speckle Where the DIC Technique Was Unable to Compute the Von Mises Strain. The Brittle Silicate Phase of the Cube Dominates the Location of Axial Splitting, Leading to Final Brittle Failure.

3.3.8 X-ray Micro-computed Tomography (X-CT)

X-CT analysis is a non-destructive method that allows for the examination of internal structural characteristics, such as porosity, distribution of different metals and minerals, and crack propagation in 3D reconstructed volumes. Unlike the DIC system, which can only measure displacement and strain on the speckled face, X-CT provides a more comprehensive understanding of the internal structure and behavior of the cubes (Baker et al., 2012; Ebel and Rivers, 2007; Friedrich et al., 2008).

To investigate the failure mechanism in cube V-5, the compression test was interrupted near the ultimate stress when the first drop in load was detected from the Instron load cell. This cube exhibited two large shock-melt veins, each measuring over 3 mm in size (Figure 37). The identification of these veins in the tomography data was confirmed by comparing them with the micrographs. It is worth noting that the primary load-bearing elements in the cube were the silicate phases, which made up more than 80% of the volume fraction. These silicate phases contributed to the brittle failure mechanism.

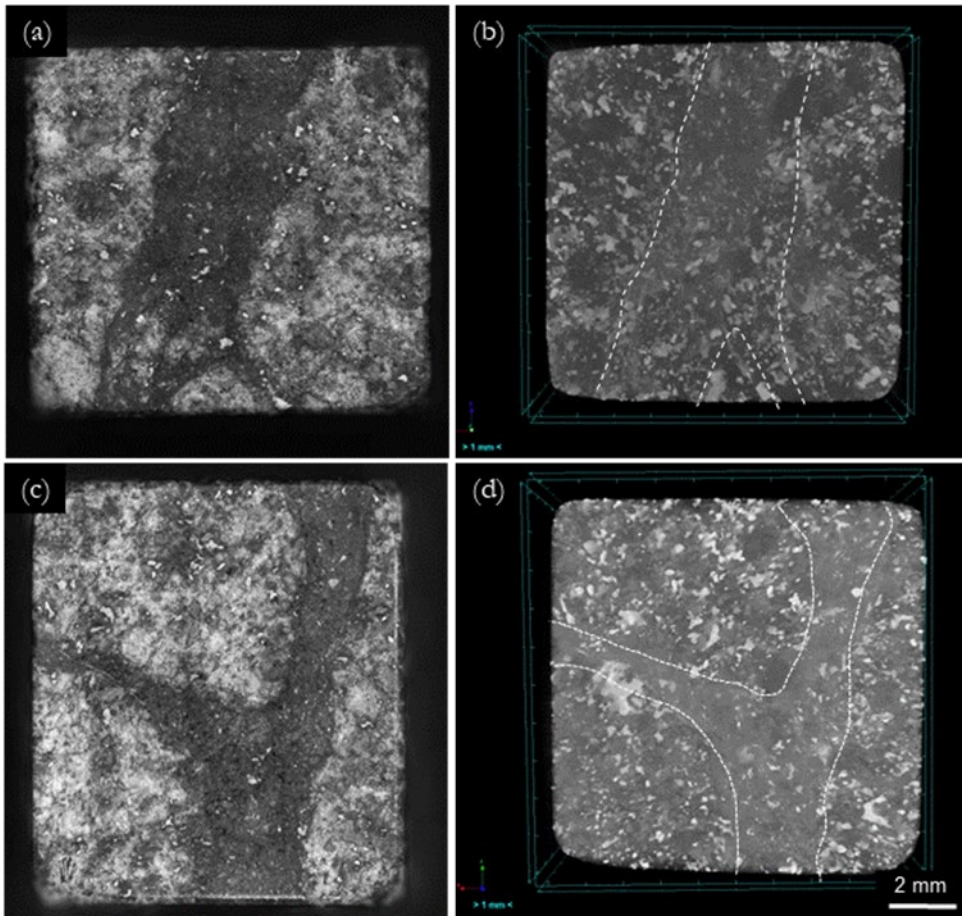

Figure 37. A Comparison of (a, c) Two Optical Images and (b, d) Corresponding X-ray Micro-CT Image of Viñales Cube V-5 Shows a Shock Melt Vein of Size > 3 mm and Randomly Dispersed Fe-Ni Metals. The White Mark in (b, d) X-ray Micro-CT Images Is Used to Identify the Large Shock Melt Vein Present in the Cube.

The X-CT analysis of the interrupted test cube provided insights into the crack propagation path through the orthogonal projection image Figure 38. In the tomography images, the metals and troilite appear as bright white and gray colors, randomly dispersed within the dark matrix composed mainly of silicate minerals such as olivine and pyroxene. A 3D volume density map was reconstructed from the tomography data, revealing the

distribution of metals within the cube. Figure 38, Figure 39, and Figure 40 demonstrate that cracks are initiated within the dark silicate phase. These cracks were observed to either deflect around the ductile metal or propagate through the boundaries between the bright metal and the dark matrix phase, resulting in inter- and intragranular fractures in the sulfide and silicate phases.

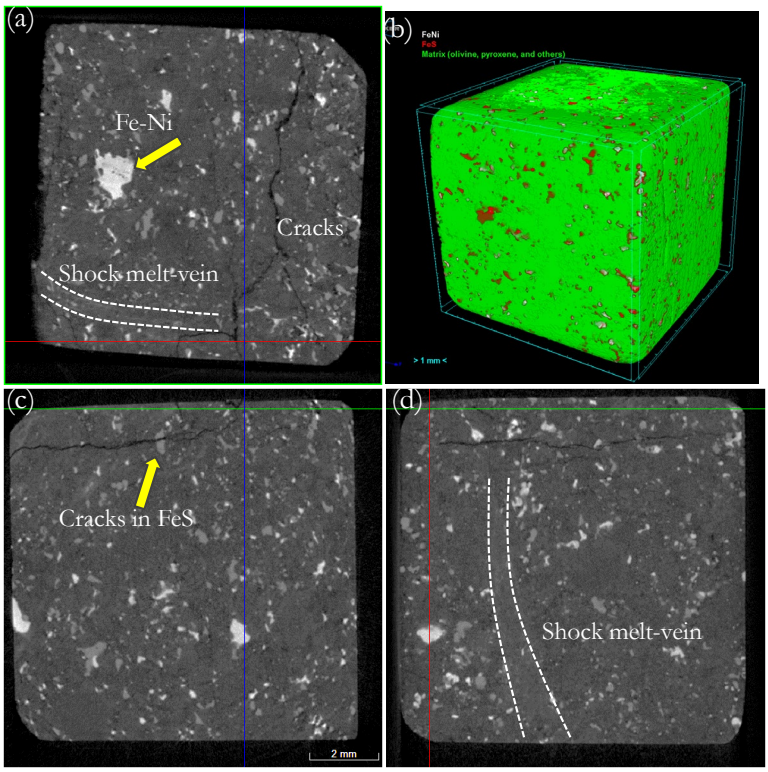

Figure 38. The X-ray Micro-CT Image of the Viñales Cube V-5 During the Interrupted Compression Experiment Shows (a, c, d) Crack Propagation Paths from the Orthogonal Projection and (b) the Reconstruction of the 3-D Cube from Tomography Images. The Orthogonal Images Show Randomly Dispersed Bright Fe-Ni, Gray FeS, and Shock Melt-veins Whereas the 3-D Reconstructed Volume Displays Fe-Ni in White, FeS in Red, and the Matrix (Which Includes Olivine, Pyroxene, and Other Minerals) in Green Color.

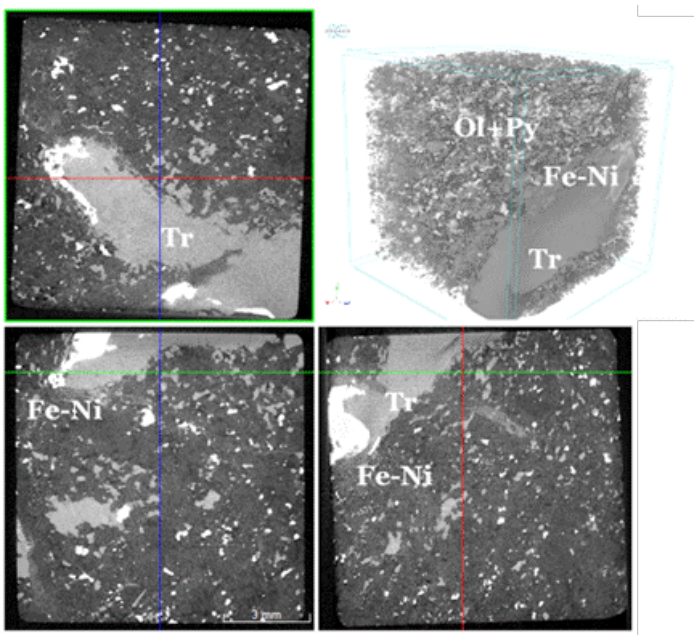

Figure 39. The X-ray Micro-CT Image of the Viñales Cube V-2 Shows Orthogonal Projections and a 3-D Reconstructed Cube Before the Compression Test. Bright FeNi, Gray FeS (Tr – Troilite), Olivine, and Pyroxene Are Segmented from the Tomography Images.

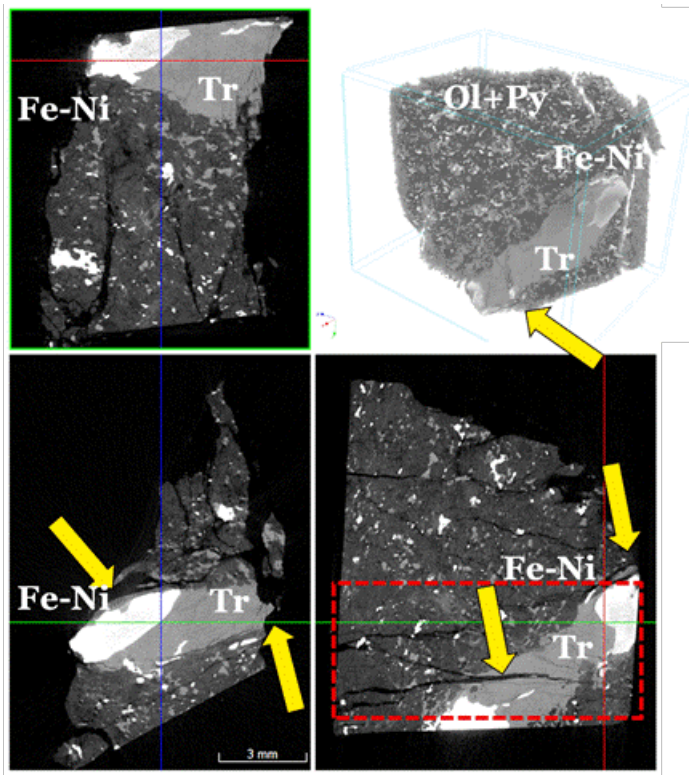

Figure 40. The X-ray Micro-CT Image of the Viñales Cube V-2 Shows Orthogonal Projections and a 3-D Reconstructed Cube after the Compression Test. The Cracks Divert Around the Ductile FeNi Boundaries but Propagate Through Brittle FeS Grains.

Following the quasi-static compression experiments, fragments of the cubes retained relatively large sizes (Figure 41). Most of the mineral phases remained unchanged, including the Fe-Ni metals that were present along the crack paths. The differences in constitutive properties between the ductile metallic phase and the brittle mineral phase led to stress concentrations under applied compressive loads. Similar to preexisting flaws, the interfaces between the metal and the matrix, with their dissimilar mechanical properties, served as sites for crack nucleation. These cracks subsequently coalesced, ultimately leading to axial splitting.

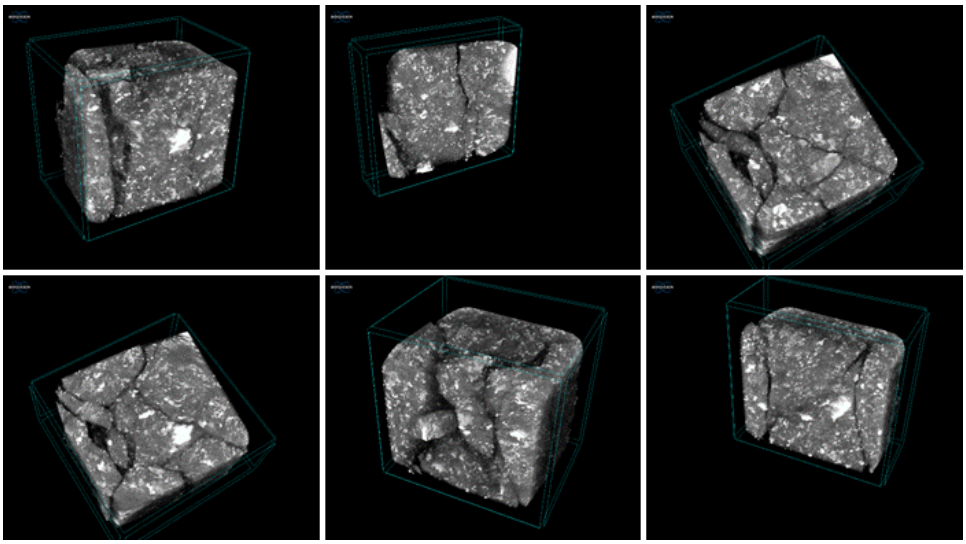

Figure 41. The 3D Volume Reconstruction of Viñales Cube V-3 after the Compression Experiment Reveals a Network of Cracks, Indicating Brittle Failure. The Bruker Skyscan CTVox Software Was Utilized to Render the 3D Volume of the Crushed Sample, with Metals Displayed in Bright White Color. Tomography Images from Various Sections and Orientations Were Recorded to Illustrate the Intricate Crack Networks Within the Cube.

The X-CT analysis revealed distinct contrasts between metals and silicates due to their different X-ray attenuations. Metals and troilite, having high X-ray attenuation, appeared as bright white in the tomography images, while the chondrules and silicate fragments exhibited lower contrast (Figure 37). For a larger sample size, such as a one-cm-sized cube, the use of high-energy X-rays was necessary. However, this approach had the unintended effect of minimizing energy attenuation by other mineral phases. Consequently, it became quite challenging to accurately segment minerals with similar densities, such as olivine and pyroxene. Figure 42 illustrates the distribution of Fe-Ni metals and the corresponding stress-strain response of cubes V-3 and V-13. While the stress-strain response may appear to correlate with porosity and mechanical response when considering only these two cubes, no significant correlation is observed when taking into account the results of the other cubes, as mentioned in the previous section.

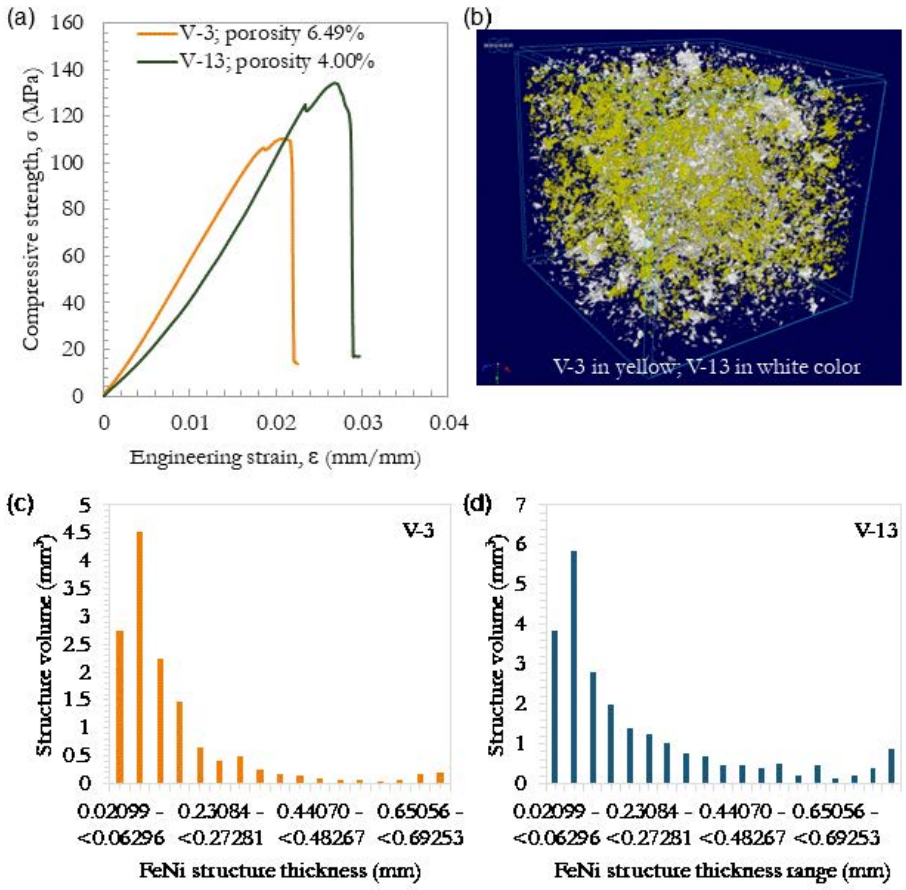

Figure 42. A Comparison Between Two Viñales Cubes (V-3 and V-13) with Porosity of 6.49% and 4.00%, respectively Shows (a) the Stress-strain Response under Uniaxial Compressive Load. Both Cubes Exhibit Brittle Failure. (b) an Overlay of 3-D Volume-reconstructed FeNi Displaying the V-3 Cube FeNi Distribution in Yellow and the V-13 Cube FeNi Distribution in White. Tomography Scans Were Performed Before the Compression Experiment to Quantify the Distribution of FeNi Metals. In (c-d) FeNi Shows a Bimodal Size Distribution in Both Cubes.

The bimodal distribution of Fe-Ni metal in these cubes suggests that cube V-13 possesses larger metal grains and a higher volume fraction of metal. This observation raises the

possibility that these factors contribute to an increase in the compressive strength of the meteorite. However, it is worth noting that a study by Farbaniec et al. (2021) argued against a direct correlation between the average compressive strength and the metal content or mean metal grain size in L ordinary chondrites subjected to quasi-static compression loading (Farbaniec et al., 2021). Therefore, further investigation is needed to fully understand the relationship between the metal distribution and the mechanical properties of the Vinales cubes. The Fe-Ni metals were successfully segmented from both the host cube and the shock vein, allowing for a detailed analysis of their characteristics. In Figure 43, the largest metal, estimated to be larger than 1 mm, is represented by a yellowish-brown color, while subsequent metals in the host cube are represented by green, and metals in the shock vein are represented by violet. Recrystallized metals in the shock melt vein appear to have a more regular shape and show less variability in size distribution compared to the metals in the host cube. The shape of the largest Fe-Ni metal, located next to the shock melt vein, provides significant insights into the internal deformation and fracturing caused by the shock events.

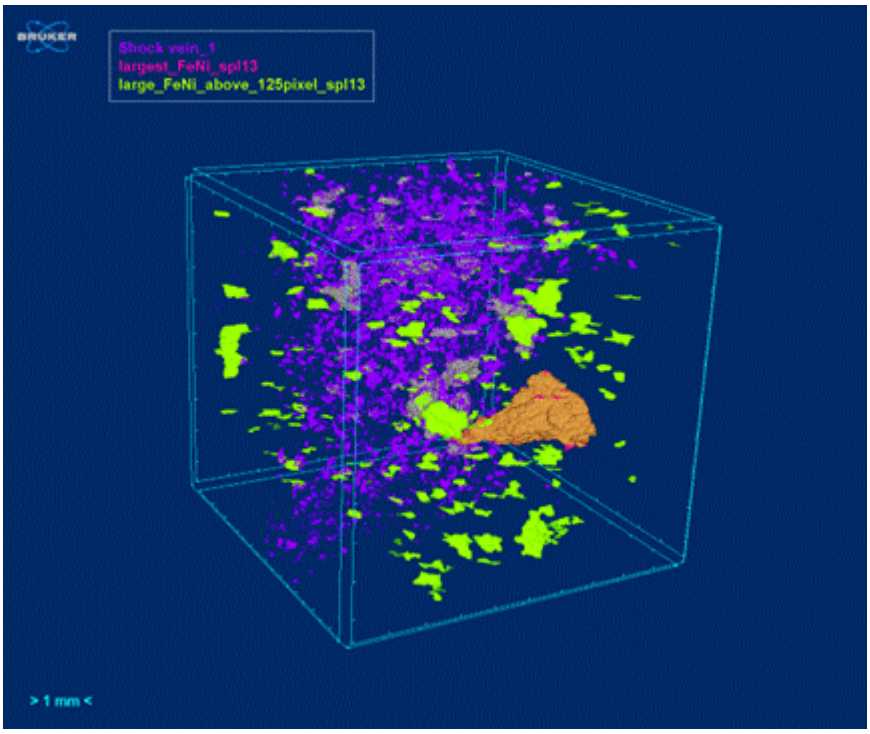

Figure 43. The 3-D Volume Reconstruction of FeNi Particles in Viñales Cube V-13 Was Obtained from X-ray CT Images. FeNi Particles with a Size Smaller than 3 Pixels Were Considered Noise and Were Removed Using a Denoise Filter in the Bruker Skyscan CTAn Software. The Resulting 3-D Volume Reconstruction Shows the Largest FeNi Particles in a Yellowish-brown Color, FeNi Particles with a Size Larger than 125 Pixels in Green, and the Shock Melt Vein in Violet Color.

Previous studies on L6 ordinary chondrites, such as Grant County (S2) and Kyushu (S5), using various stereographic methods, showed that with increasing shock loading, the collective degree of preferred metal orientation also increased (Friedrich, 2008). For Vinales cubes, it can be postulated that during the shock event, relatively ductile metals deform while brittle silicates are affected by the compression and rarefaction phases. The wide range of preferred

metal orientations could be attributed to the multiple impacts and shock events experienced by the meteorite.

3.4 Summary

The Viñales (L6) ordinary chondrite was extensively characterized to gain insights into its physical and mechanical properties, as well as to investigate its failure mechanisms. Elastic wave velocity measurements indicated isotropic material symmetry, consistent with other brittle materials and stony meteorites. Microstructural analysis using backscattered electron imaging and X-ray intensity maps revealed the presence of key phases, including olivine, pyroxene, troilite, feldspar, and metal grains. Notably, the metal grains exhibited variations in Fe and Ni concentrations, suggesting the existence of sub-grains with distinct inelastic responses.

Quasi-static compression tests combined with digital image correlation (DIC) demonstrated the development of wing cracks that ultimately resulted in the axial splitting of the Viñales meteorite. However, X-ray Computed Tomography (X-CT) analyses did not show a significant correlation between crack nucleation and the shock-melt veins. Although a correlation between the structural characteristics of Fe-Ni metals and the mechanical properties of the meteorite was observed in two cubes, this remains a subject of debate in the literature, highlighting the need for further research on the influence of metal content on meteorite mechanical properties.

In summary, the DIC and X-CT analyses emphasized the crucial role of silicate phases, which act as the primary load-bearing elements in the cube, in the brittle failure mechanism of the Viñales meteorite. These findings advance our understanding of the behavior of the

Viñales meteorite and provide valuable insights into the intricate relationship between its microstructure and mechanical properties.

CHAPTER 4

STRENGTH AND FAILURE CHARACTERIZATION OF THE GIBEON (IVA) IRON METEORITE

4.1 Introduction

Iron meteorites provide valuable insights into the formation of early planetary bodies (Goldstein et al., 2009). Many of these meteorites are believed to originate from the cores of differentiated planetesimals while others likely formed from smaller metallic pools in the mantle or crust (Scott, 2020). The process involves the melting of chondritic planetesimals due to the heat generated by radioactive decay, causing denser metallic elements like iron and nickel to sink to the core, surrounded by silicate mantles and crusts. These differentiated planetesimals experienced collisions, resulting in the loss of their outer rocky layers. Fragments of the iron-rich cores, known as iron meteoroids, are then exposed to interplanetary space, eventually deorbiting and falling onto Earth as iron meteorites (Katsura et al., 2014; Slyuta, 2013; Yang et al., 2007). Iron meteorites are relatively rare, constituting only 4-5% of all meteorite falls (Buchwald, 1975; Krot et al., 2014). However, they are found abundantly among finds in specific regions, particularly in the vicinity of terrestrial impact craters smaller than 1 km in diameter (Buchwald, 1975). Moreover, iron meteorites have also been discovered on Mars (Ashley et al., 2011), further highlighting their prevalence and distribution beyond Earth.

The NASA Psyche mission will be the first attempt to explore the largest metal-rich asteroid, 16-Psyche, which orbits the Sun between Mars and Jupiter (Dibb et al., 2023; Elkins-Tanton et al., 2020; Hutchinson et al., 2023). The primary goal of this mission is to gain a deeper understanding of the asteroid's features, composition, and texture to test hypotheses

about its formation. This mission provides a unique opportunity to examine a differentiated metal-rich body suspected to have a Fe-Ni core, which is believed to be one of the building blocks of our solar system. Therefore, studying metallic or iron meteorites is crucial to comprehending the characteristic features, composition, and mechanical behavior of metal-rich asteroids.

Iron meteorites exhibit a characteristic microstructure known as the Widmanstätten pattern, which is intricately linked to the composition and cooling rate of the parent body (Yang et al., 2010). This pattern is characterized by the presence of two primary metal phases: the body-centered cubic (BCC) α-iron phase known as ferrite, commonly referred to as kamacite, which is alloyed with approximately 7 wt.% Ni, and the face-centered cubic (FCC) iron phase containing around 30-40 wt.% Ni, known as taenite (Knox, 1970). The formation of the Widmanstätten pattern forms as a result of slow cooling, where the temperature decreases by approximately 1K throughout several hundred to thousands of years. During this extended cooling period, the solid-state transformation from FCC taenite to BCC kamacite occurs. As a result, microscopic crystals of kamacite nucleate and grow from the taenite phase, giving rise to the characteristic Widmanstätten pattern observed in iron meteorites (Goldstein et al., 2009; Short and Andersen, 1965). The phase diagram and interdiffusion rates of this binary Fe-Ni alloy necessitate an extremely slow cooling process to achieve the distinctive Widmanstätten pattern. Understanding and investigating the complexities of this microstructure is essential for comprehending the mechanical behavior of iron meteorites.

One notable characteristic of iron meteorites is the presence of distinctive microstructural features that result from impact events. Among these features, Neumann bands have been observed in the Gibeon IVA iron meteorite. These unique microstructures provide valuable

insights into the history and evolution of iron meteorites, allowing scientists to analyze the effects of impact forces and gain a deeper understanding of the processes that shaped these celestial bodies. A previous study by Uhlig (1995) has revealed that Neumann bands form as a result of shock wave experiences at low temperatures. Crystallographically, these hexahedrite bands arise from the mechanical twinning of α-iron lamellae along the (112) plane (Uhlig, 1955). In an attempt to classify the shock stages of various iron meteorite types, including IVA, IVB, and ungrouped meteorites, Yang et al. (2011) proposed that Neumann bands can be attributed to shock stage 1, indicating relatively weak collisions. Additionally, it is suggested that these bands could have disappeared if subjected to annealing from subsequent heating events, providing valuable insights into the fewer alteration processes undergone by iron meteorites after the formation of the early solar system (Ohtani et al., 2022; Yang et al., 2011).

The origin, microstructure, and compositional variation of Fe-Ni iron meteorites have been the subject of extensive research (Bunge et al., 2003; Goldstein et al., 2009; Yang et al., 2010). A limited number of studies have aimed to understand the mechanical properties of iron meteorites at different temperatures and strain rates, investigate their failure behavior, and examine the influence of the ductile-to-brittle transition temperature on the fragmentation of the parent body (Auten, 1973; Gordon, 1970; Knox, 1970; Petrovic, 2001). It has been observed that the deformation behavior of iron meteorites strongly correlates with temperature (Auten, 1973; Gordon, 1970; Johnson and Remo, 1974).

Despite the unique microstructure of iron meteorites, the crystallographic phase transformation mechanism from FCC to BCC remains similar to that of iron and other metals (Cayron, 2014; He et al., 2006; Hutchinson and Hagström, 2006; Nolze et al., 2005; Ueki et al., 2021). Previous studies on deformation behavior have shown that BCC metals, similar to

the crystallographic structure of kamacite, exhibit brittle failure at low temperatures and ductile failure at high temperatures (Johnson, 1962). Additionally, mechanical properties have been found to vary as a function of temperature. Some mechanical properties, such as hardness (Jain et al., 1972), strength (Ahles et al., 2021; Gordon, 1970; Ueki et al., 2021), and elastic modulus (Wheeler, 2021), have been studied on a limited number of iron meteorites.

While previous studies have provided insights into the mechanical properties of iron meteorites, further investigation is needed to understand the in-situ deformation behavior and the contribution of the intricate microstructure and varying composition of Fe-Ni alloys. This paper aims to address these gaps by characterizing the microstructural and mechanical properties of the Gibeon IVA iron meteorite and investigating its deformation mechanism using in-situ digital image correlation (DIC). The utilization of DIC enables us to measure full-field strains, which are essential for examining the damaged surface and gaining a better understanding of damage initiation and propagation in the tested specimens. Moreover, this study focuses on studying the damage mechanism at low temperatures. The optical and scanning electron micrographs of the post-failure surface are analyzed in conjunction with the DIC data to explore the influence of the different phases of the Gibeon IVA iron meteorite on the observed damage mechanisms. The findings of this study will lead to an improved understanding of metal-rich asteroids such as 16-Psyche. Through the provision of improved physical and mechanical properties and elastic coefficients derived from iron meteorite data, our research will support asteroid disruption and deflection models, thereby enhancing our understanding of these celestial bodies. Ultimately, these findings will aid in the refinement of strategies for managing potential asteroid threats and contribute to our broader knowledge of the behavior of metallic asteroids.

4.2 Material and Methods

The Gibeon meteorite is classified as a Group IVA iron meteorite and exhibits a fine octahedrite Widmanstätten pattern. A slow cooling through temperature ranges of 800-350°C over millions of years creates a homogeneous kamacite precipitate in the taenite matrix, which grows to form the Widmanstätten structure (Narayan and Goldstein, 1985). This structure is observed throughout the entire body, indicating that the material consisted of a single crystal taenite phase that transforms into a low-nickel kamacite phase (Hutchinson and Hagström, 2006; Scott, 2020). For this study, Gibeon meteorite samples with dimensions approximately 150 x 10 x 10 mm^3 were obtained from the Buseck Center for Meteorite Studies at Arizona State University. Chemical analysis was conducted on a polished cube to characterize the compositional variations in Fe-Ni and to examine the presence of minor elements and inclusions within the cubes. Major and minor elements of the Gibeon meteorite were determined from a 1-cm cube using a field-emission electron microprobe analysis (JEOL JXA-8530F Hyperprobe) equipped with a wavelength-dispersive spectrometer (WDS) and an energy-dispersive spectrometer (EDS). X-ray intensity maps of all major elements were obtained at an accelerating voltage of 20 kV and a microprobe beam current of 7.9 nA through continuous WDS-EDS analysis. Elastic properties were measured from four rectangular parallelepiped samples by measuring the normal and shear wave velocities. The mechanical behavior and damage mechanism of the Gibeon meteorite were studied through quasi-static compression and tension experiments. Five 1 cm cubes were prepared for the compression experiment, and eight sub-sized tensile specimens with a gauge length of 32 mm, a width of 6 mm, and a thickness of 2 mm were prepared for the tensile experiment following the ASTM

E8-21/E9 standard. Four tensile specimens were tested at ambient temperature, while the remaining four tensile specimens were used for low-temperature tensile testing.

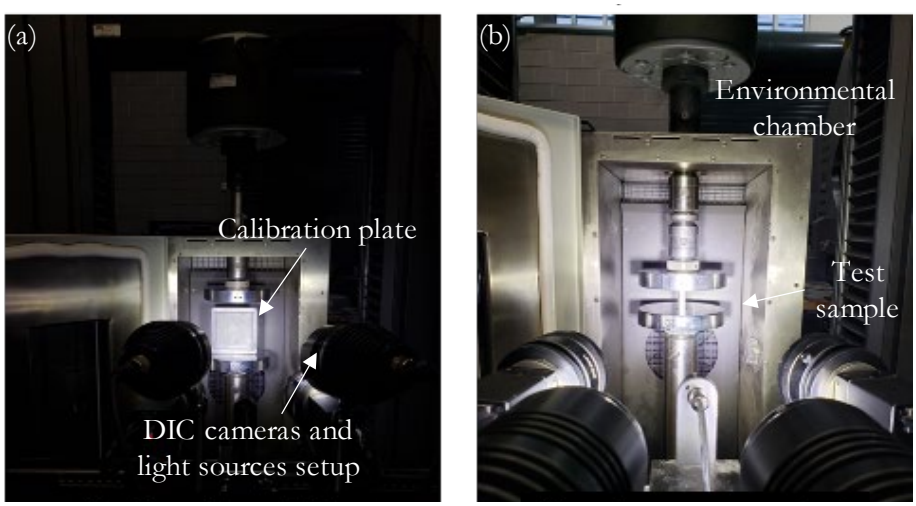

Figure 44. Experimental Setup for Quasi-static Compression Experiments Involved (a) the Utilization of Two Cameras and Light Sources for In-situ DIC Displacement and Strain Measurements. (b) Experimental Setup with the Environmental Chamber for Low-temperature Testing. Prior to Each Set of Tests, the System Was Calibrated Using a Calibration Cube Provided by ARAMIS to Ensure Accurate and Reliable Measurements.

Compression and tension tests were performed at ambient temperature using a universal testing machine, specifically the Instron 5985 frame, equipped with a 250 kN load cell. The tests were conducted at a displacement rate of 0.25 mm/min to ensure consistent and controlled loading conditions. For low-temperature tensile experiments, an Instron 3119-409 environmental chamber with a temperature range of -70° C to 250° C was utilized. This chamber allowed for testing under controlled low-temperature conditions, providing insights into the material's behavior at different temperatures.

During the mechanical testing, in-situ digital image correlation (DIC) was employed to capture and analyze the deformation and strain evolution in the samples in real-time. The ARAMIS 5M DIC system was utilized for this purpose, enabling accurate measurements and analysis of the specimen's response to loading. To ensure accuracy, the DIC system was calibrated to compensate for lens distortion and maintain dimensional consistency. The calibration process involved using a calibration cube provided by ARAMIS that ensured accurate and reliable measurements throughout the experiments (Figure 44). The displacement and strain fields both in the longitudinal and transverse directions are measured from the stochastic speckle pattern of deformed images to compute local and global strain fields; the information is useful for identifying crack initiation and propagation. Post-failure surfaces of the tested specimens were analyzed using the JEOL JXA-8530F at an accelerating voltage of 20 kV with a beam current of 7.9 nA to further investigate the failure mechanisms. To understand the microstructural evolution and damage upon loading, Optical and SEM micrographs were obtained for the original and the tested Gibeon samples (post-compression and tension tests). Pieces of the test samples were embedded in epoxy, ground flat, polished, and etched with 2% nital solution to reveal the Widmanstätten pattern and deformation mechanism.

4.3 Result and Discussion

4.3.1 Microstructural Characterization

The optical micrograph of the Gibeon meteorite displays the typical Widmanstätten structure, dominated by oriented kamacite lamellae separated by thin taenite boundaries (Figure 45). The composition of kamacite is measured as 92.28 ± 0.69 wt.% Fe, 7.11 ± 0.13

wt.% Ni, 0.39 ± 0.01 wt.% Co, and 0.04 ± 0.01 wt.% P, while that of taenite is 71.28 ± 2.72 wt. % Fe, 27.52 ± 2.82 wt. % Ni, 0.15 ± 0.05 wt. % Co, and 0.01 ± 0.01 wt. % P (Figure 47). The intricate intergrowth pattern of the Widmanstätten microstructure is revealed by etching polished Gibeon pieces with 2% Nital. The Widmanstätten structure is composed of two phases: kamacite, a nickel-poor α-iron phase (Fe ~ 7 % Ni), and taenite, a nickel-rich γ-iron phase (Fe ~ 30-40 wt.% Ni) with a specific crystallographic orientation relationship.

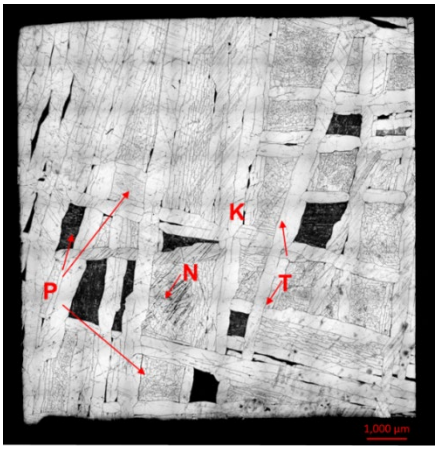

Figure 45. Reflected-light Photograph of a 1-cm Gibeon Meteorite Cube Showing the Widmanstätten Pattern. Elongated Kamacite Laths Are Visible in the Micrograph (Light-colored Regions) and Dark-etched Plessite, Indicated by P. Plessite is a Fine-scale Intergrowth of Kamacite (K) and Taenite (T). Neumann Bands, Identified as N in the Micrograph, Are Also Present. The Sample was Etched with Nital.

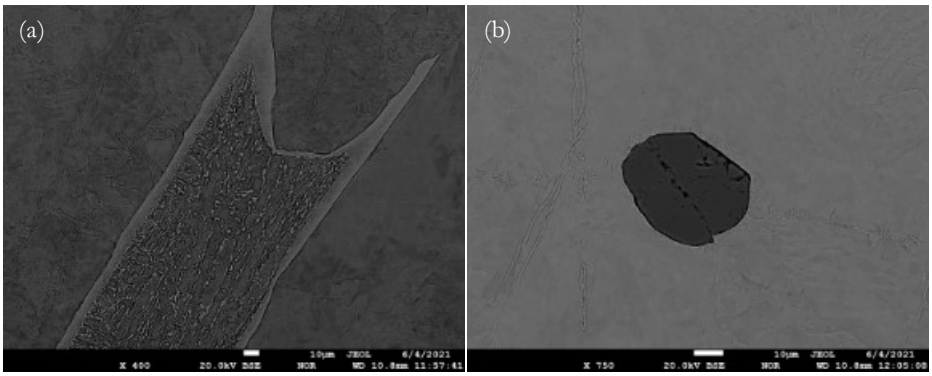

Figure 46. SEM Images of (a) Plessite Showing a Bright Taenite Rim and Mottled Interior of Kamacite and Taenite, (b) Inclusion of the Sulfide Minerals, Daubréelite, $FeCr_2S_4$.

The kamacite laths in Gibeon are 220.8 ± 77.2 μm wide and several millimeters long, consistent with a fine octahedrite (Goldstein et al., 2009). Submicron-sized dark etched plessite, a fine-grained mixture of kamacite and taenite, is also common (Figure 46). This may form at low temperatures in the prior taenite region (Goldstein et al., 2009). Plessite can form through several different mechanisms, such as direct or indirect transformation from taenite or the formation and decomposition of martensite (Goldstein and Michael, 2006). The formation of coarse plessite can be explained in terms of a lower nucleation temperature due to greater undercooling or a higher nickel content because of diffusion from adjacent Widmanstätten structures. The occurrence of Neumann bands indicates prior shock-induced deformation of the kamacite crystal and is thought to be due to impact events on the parent body of the meteorite (Buchwald, 1975). S content in iron meteorites is concentrated in the troilite inclusions and some daubréelites (Buchwald, 1975). EMPA X-ray intensity maps (Figure 47) reveal the presence of chromium-rich sulfide particles, daubréelite, measuring 42.9 μm. However, these particles are considered insignificant when analyzing the strength

properties of the Gibeon meteorite. Daubréelites typically form close to troilite (FeS) grains due to thermal metamorphism (Khodakovsky and Petaev, 1981).

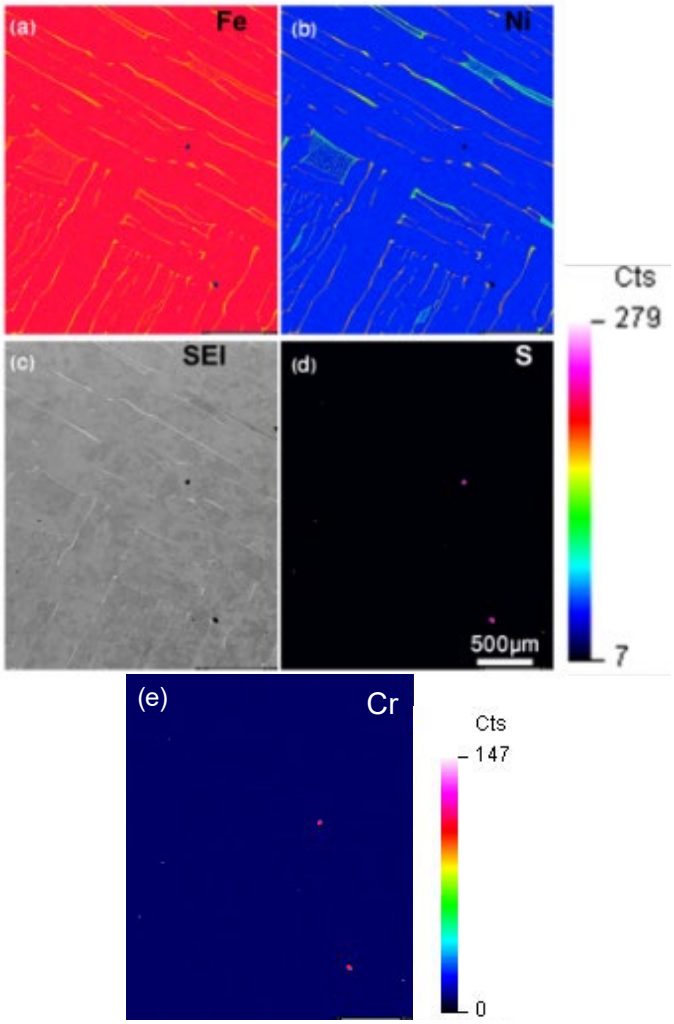

Figure 47. EPMA X-ray Intensity Maps and Secondary Electron Image (SEI) of a 1-cm Gibeon Meteorite Cube Show the Elemental Distribution of Fe, Ni, S, and Cr, Allowing the Identification of Kamacite, Taenite, and Daubréelite.

4.3.2 Physical and Mechanical Characterization

The elastic properties of Gibeon were determined using the Olympus 5077 PR ultrasonic pulse generator/receiver to measure the sound speed. The measurements were conducted

using 5 MHz full-contact transmission longitudinal ultrasonic transducers (V-110 RM, Olympus NDT) and a normal incidence shear wave transducer (V-156RM, Olympus NDT). The acquired data were analyzed in MATLAB to derive the physical and elastic properties. (

Table 12). The average density of the five cubes was 7.69 ± 0.30 g/cm3, which falls within the range of iron meteorite densities (Dyaur et al., 2020). The average values for the P-wave velocity and S-wave velocities were 4757 ± 40.6 m/s and 2605 ± 18.4 m/s, respectively. These values were then used to calculate the elastic properties.

Table 13 presents the calculated average values for the elastic modulus, shear modulus, and Poisson ratio, which were found to be 136 ± 1.41 GPa, 53 ± 0.75 GPa, and 0.28 ± 0.01, respectively. Dyaur et al. (2020) conducted similar measurements on four different iron meteorites, including Gibeon, and reported densities ranging from 7.15 g/cc to 7.85 g/cc, P-wave velocities from 5580 m/s to 7850 m/s, and S-wave velocities from 2610 m/s to 3370 m/s. Additionally, Flynn et al. (1999) reported a P-wave velocity of 6260 m/s for Gibeon, slightly higher than that of man-made steel at 5940 m/s (Flynn et al., 1999). However, the average values of the P-wave velocity of Gibeon, as measured in this study, are slightly lower compared to the literature, while the S-wave velocities are consistent with the published works.

It is well-known that elastic wave velocities are sensitive to the physical and mechanical properties of materials, including density, porosity, and material strength but are independent of the material shape. Previous studies on iron meteorites have revealed a linear relationship between elastic wave velocity and density (Dyaur et al., 2020). Additionally, Slyuta (2011) reported that from coarse to fine octahedrite structures, elastic wave velocities tend to increase (Gorshkov, 1973; Slyuta, 2013). In comparison to relatively porous meteorites like ordinary

chondrites, iron meteorites exhibit higher wave velocities and demonstrate excellent mechanical properties (Jones, 2009; Rabbi et al., 2022). These findings highlight the unique characteristics and superior mechanical performance of iron meteorites.

Table 12. Physical Properties and Compressive Yield Stress of the Five Gibeon Cubes.

Cube no.	Dimensions in mm			Mass (g)	Vol. (cm^3)	Density, ρ (g/cc)	Yield strength (MPa)
	Height	Width	Thickness				
G1	10.10	10.19	10.10	7.39	1.04	7.12	250
G2	9.88	10.10	9.17	7.16	0.92	7.87	260
G3	10.06	10.42	9.71	7.82	1.02	7.66	410
G4	10.19	9.55	9.67	7.39	0.94	7.86	360
G5	9.91	10.22	8.93	7.70	0.90	7.96	260
Avg.	10.03	10.10	9.52	7.49	0.96	7.69	308
SD	0.12	0.29	0.42	0.23	0.06	0.30	64.93

Table 13. Densities and Elastic Properties of the Four Gibeon Specimens.

Cube no.	Mass (g)	Vol. (cm^3)	Density, ρ (g/cc)	Elastic modulus, E (GPa)	Shear modulus, G (GPa)	Poisson's ratio, ν	P-wave velocities (m/s)	S-wave velocities (m/s)
G6	26.10	3.33	7.83	135	52	0.30	4830	2590
G7	26.60	3.38	7.86	134	53	0.28	4710	2580
G8	27.90	3.57	7.81	138	54	0.27	4760	2630
G9	26.20	3.35	7.81	137	54	0.27	4730	2620
Avg.	24.56	3.14	7.81	136	53	0.28	4,757	2,605
SD	4.34	0.55	0.04	1.41	0.75	0.01	40.68	18.44

4.3.3 Mechanical Response of Gibeon at Ambient Temperature

Quasi-static uniaxial compression tests were conducted on the Gibeon cubes at ambient temperature. Figure 48 illustrates the comparison between the original and deformed samples.

The compression tests were interrupted within the range of 30% to 50% of strain due to the significant elastic and plastic deformation exhibited by Gibeon. No fractures were observed in the cubes during or after compression. The applied load increased proportionally until reaching the yield point, and strain hardening continued until the end of the tests. This plastic deformation of Gibeon iron meteorites can undergo nearly 100% compression without failure.

The average yield strength of Gibeon, measured at 0.2% strain, was found to be 308 ± 64.9 MPa for comparison. Canyon Diablo iron meteorite exhibits compressive yield stresses ranging from 409 to 441 MPa at 0.2% plastic deformation (Knox, 1970; Ostrowski and Bryson, 2019). Figure 48 shows a bilinear trend within the elastic and plastic regions of the stress-strain response, along with a slight variation in yield strength among the samples. These differences in yield stress and strain hardening can be attributed to multiple factors, including the relative orientation of the structure and the direction of compression, as well as the microstructural heterogeneity present in the Gibeon iron meteorite.

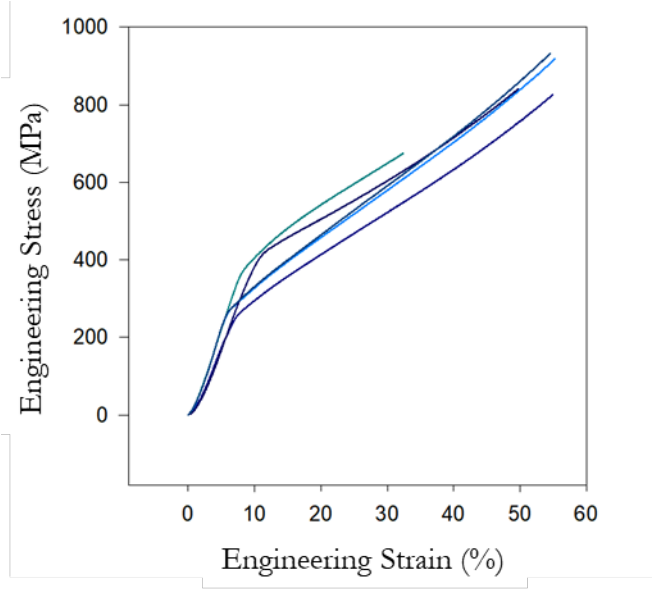

Figure 48. Engineering Stress-strain Responses of Five 1-cm Gibeon Cubes at Ambient Temperature. All Cubes Exhibited Continued Deformation as the Load Increased. Compression Tests Were Interrupted When the Displacement Reached Approximately 50% of the Original Length.

Figure 49. An Illustration of Both the Original and Compressed Gibeon Meteorite Cubes. The Cubes Exhibit Uniform Compression and Show No Cracks upon Visual Inspection.

The strength of iron meteorites is influenced by the composition of the phases present and their orientation with respect to the direction of the applied load (Marchi et al., 2020; Remo and Johnson, 1975). The presence of mineral inclusions, such as daubréelite (Figure 50), showed no significant effect on the failure of Gibeon cubes under compression. In ductile materials, the damage mechanism can be governed by either void coalescence or plastic instability of the specimens. Void nucleation typically occurs at inclusions, and plasticity aids in their growth and coalescence, eventually leading to crack formation and material fracture.

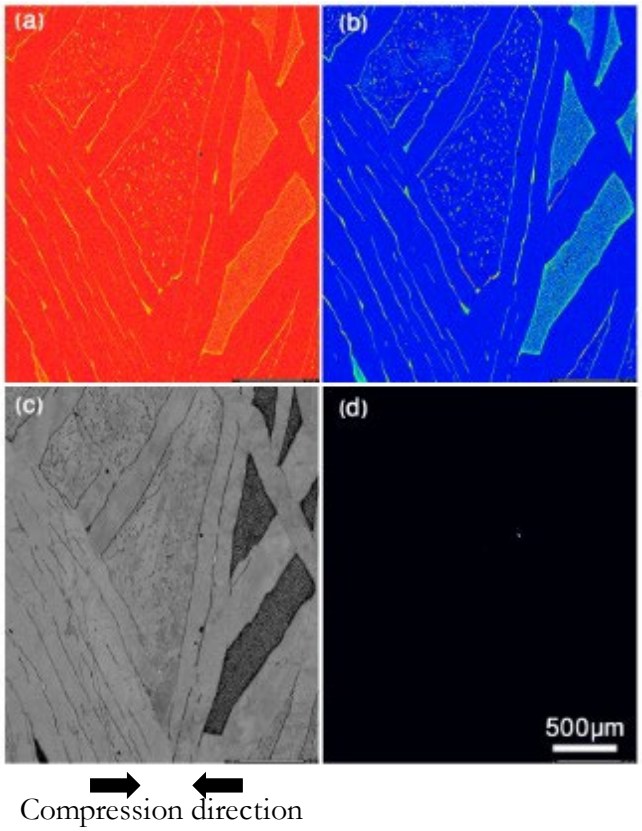

Figure 50. EPMA X-ray Intensity Maps Show the Elemental Distribution of (a) Fe, (b) Ni, and (d) S and (c) Secondary Electron Image (SEI) of a 1-cm Gibeon Meteorite Cube after Compression. Both Kamacite and Taenite were Deformed under Compressive Loading. No Cracks Were Observed in the Compressed Cube.

In the case of Gibeon specimens, the EMPA analysis did not reveal any evidence of fracture. Figure 50 displays X-ray intensity maps for elements Fe, Ni, S, and a SEI micrograph for a compressed cube. During the compression the cubes showed uniform deformation, resulting in the elongation of the kamacite lamellae perpendicular to the loading direction. The ductile deformation of the cubes displayed plastic instability when subjected to compression, leading to the development of multiple shear bands. No fracturing was observed in the Gibeon cubes during the quasi-static compression experiments.

Gibeon tensile specimens exhibit similar damage behavior in uniaxial tensile tests at a similar displacement rate and temperature; they begin stretching proportionally until the elastic limit, then undergo strain hardening and plastic deformation. However, after undergoing large nonlinear plastic deformation followed by necking at the ultimate strength, cracks start to propagate perpendicular to the load direction and the samples fail (Figure 51). The results from both compression and tension tests demonstrate ductile failure mechanisms characterized by extensive plastic deformation. The average tensile yield strength of Gibeon, measured at 0.2% strain, was found to be 255.6 ± 3.7 MPa. The average ultimate tensile strength, measured at a mean strain of 6.3 ± 0.95%, is 305.7 ± 4.6 MPa. This average value is lower than the 402.65 MPa reported by Knox (1970) for a forged rod made of Gibeon (Bethany) meteorite. The variation in tensile strength can be attributed to factors such as microstructural heterogeneity, strain rate, and the percentage of Ni concentration in the sample.

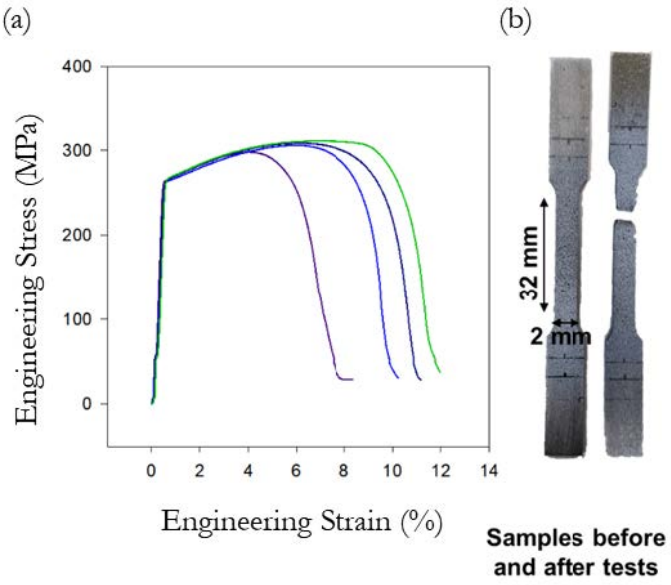

Figure 51. (a) Engineering Stress-strain Response of Four Gibeon Meteorite Tensile Samples at Ambient Temperature. Image of the Sample Shows (b) Before and after the Quasi-static Tension Experiment, Highlighting the Location of Failure and Elongation and Plastic Deformation. Stochastic Speckle Patterns on the Sample Were Utilized for In-situ DIC Measurements to Identify the Progression of Damage on the Sample.

4.3.4 In-situ Digital Image Correlation (DIC)

DIC was used to track the displacement and strain evolution in the Gibeon samples during testing. In addition, the samples were observed under an optical microscope to study the deformation in the Widmanstätten structure. When compressed, the Widmanstätten structure is elongated perpendicular to the loading direction (Figure 52), and the DIC measurement results are consistent with the optical micrograph, which shows that the local strain is concentrated along the kamacite lamellae. The von Mises strain analysis is used to identify the region of high strain concentration, which is an indication of maximum deformation on the surface. To study the local change in von Mises strain, two virtual section lines are formed along the axial and lateral directions, and the evolution of the strain is measured (Figure 53). As the compressive load increases, the samples deform plastically in the direction perpendicular to the applied load. The evolution of the von Mises strain along the section length reveals multiple peak values corresponding to the region of localized strain. The maximum values of the strain are localized on kamacite lathes, which is confirmed by the DIC results when compared with the optical images. The taenite can exhibit a strength three times higher than kamacite (Ueki et al., 2021), and this difference in mechanical properties is confirmed by the in-situ DIC displacement and strain contour results. During plastic deformation, distinct patterns of strain localizations in the von Mises strain contours (Figure

52), and shear bands (Figure 53) were observed possibly induced by the piled-up dislocations (Parz et al., 2013).

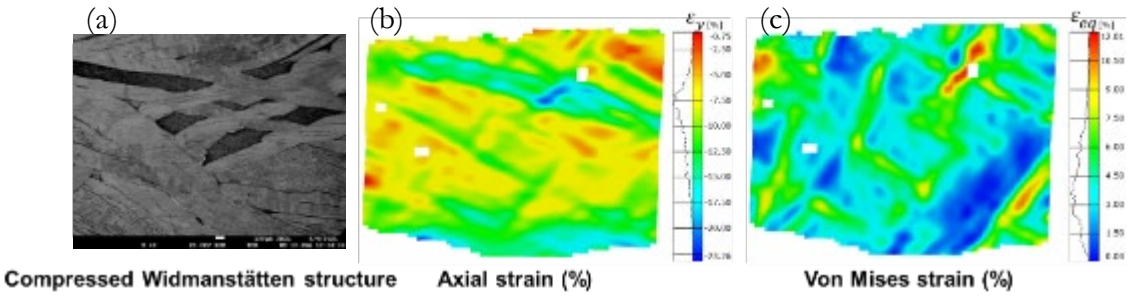

Figure 52. (a) BSE Image Displays the Deformation of the Widmanstätten Pattern in an Etch-compressed Gibeon Cube (G7). An Example of Locations of High Strains and Possible Regions of Damage Initiation Revealed from the DIC Measurements of (b) Axial Strain and (c) von Mises Strain from a Typical Gibeon Cube (G2).

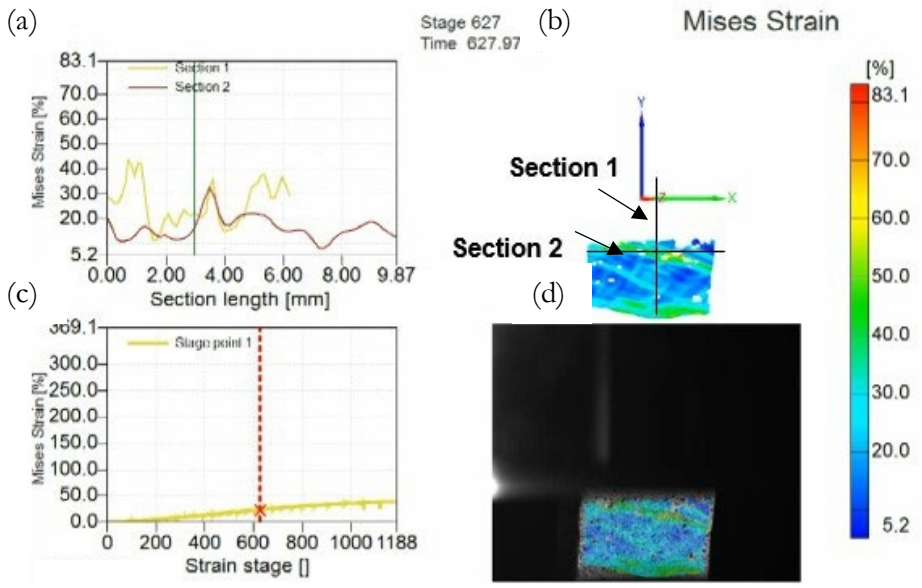

Figure 53. The von Mises Strain Contour Reveals (a) the Variation in Strain along the Axial (Section Line 1) and Lateral (Section Line 2) Directions of Compression Loading. The Strain

Contour Map (b) Provides a Visual Representation of the Strain Distribution Across the Sample. The Change in the Strain at Each Strain Stage Is Depicted in (c), and (d) Displays an Overlay of the Strain Contour on the Compressed Cube.

The DIC measurements of samples under tensile loading show crack nucleation and propagation (Figure 54). At the location of maximum von Mises strain, samples experience thickness reduction leading to a larger shear angle, which corresponds to crack initiation and final failure. The etched samples exhibit a regular Widmanstätten pattern. Overlaying the DIC strain results on the etched samples reveals that kamacite supports the primary load at the beginning of the test, followed by taenite. At higher loads, deformation was observed in both kamacite and taenite, as evident from the images obtained using the high-resolution camera (Figure 55. Similar to the DIC measurements during the compression tests, two virtual section lines along the axial and lateral direction of the gauge length of tensile samples are created to investigate strain evolution. The region of fine kamacite lamellae displays the location of maximum von Mises strains, which is supported by the peak strain from the right side of the sample shown in the DIC measurement (Figure 55). The peak values of von Mises strains and their location indicate the yielding location. Figure 56 illustrates progressive damage evolution in the tensile specimen during the onset of failure, captured using a high-speed camera to record real-time deformation. The polished face of the specimen shows the locations of deformation within the Widmanstätten pattern. At the top of the gauge section, a combination of kamacite and plessite, oriented in different directions, develops a wavy surface under tensile load. This phenomenon can be attributed to the intricate interaction of dislocations along the favorable slip plane direction. On the other hand, the bottom of the gauge section predominantly consists of kamacite lamellae aligned along the same direction and show

numerous Neumann bands. As the load increases, the occurrence of plastic instability becomes evident, manifested through the formation of shear bands. The strain concentration in the gauge region, under tension, results in the initiation of new fracture surfaces. The tensile specimens showed necking before fracture, a common failure mechanism of ductile materials. From a micro-mechanical perspective, tensile failure can be explained as follows: when the shear component of the applied stress is resolved along a slip plane, slip systems activate, and failure occurs due to the shear acting on the slip planes (Ueki et al., 2021).

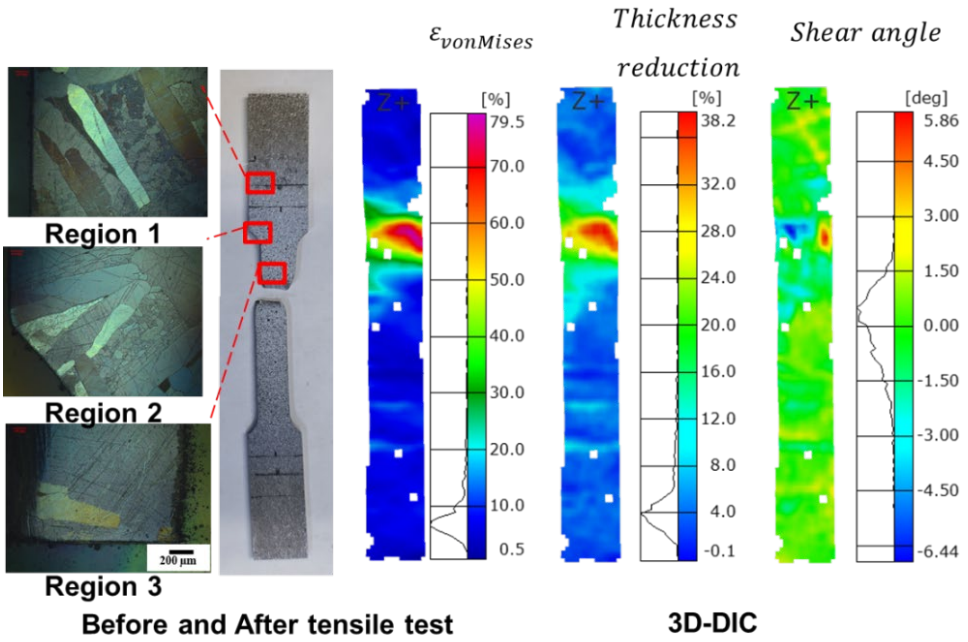

Figure 54. Gibeon Widmanstätten Structure Shown Before the Tensile Test at Three Different Regions Close to the Failure Region (Left) and Corresponding Deformation and Strain Evolution from the DIC (Right) under Tensile Loading Indicating the Location of Failure Initiation.

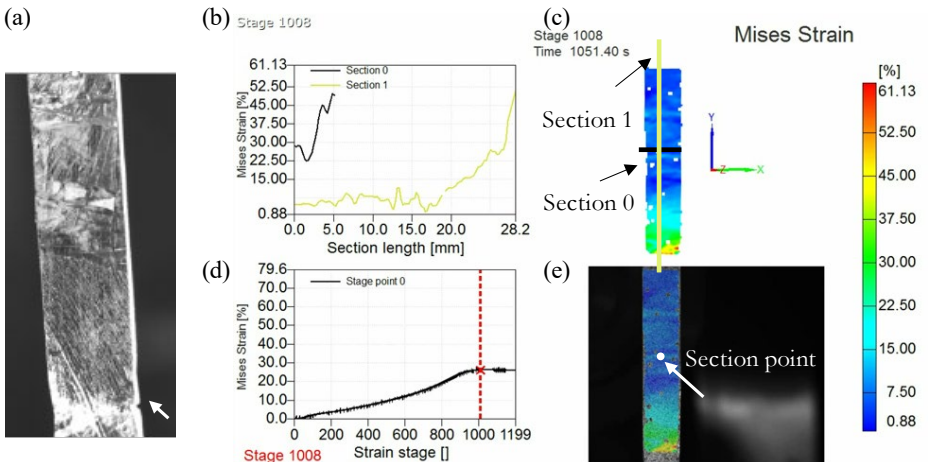

Figure 55. A Real-time Deformation in Widmanstätten Structure, (a) Captured from a High-resolution Camera under Tensile Loading and Corresponding DIC Results (b-e) Showing Von Mises Strain Evolution along the Axial and Lateral Direction of the Loading and an Overlay of Strain Contour on the Gibeon Sample.

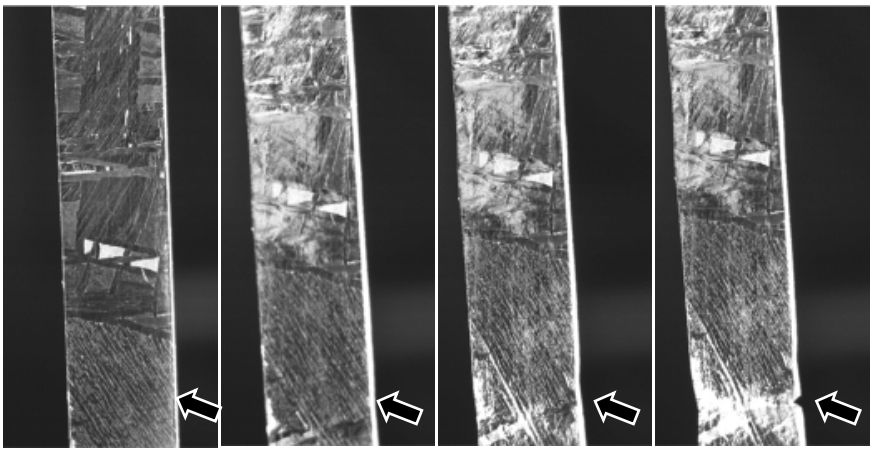

Figure 56. Deformation in Large Kamacite Lamella of the Tensile Specimen Shows the Evolution of the Crack Nucleation and Formation of Shear Bands at Onset of the Failure, Marked by the Arrow in the Widmanstätten Pattern.

4.3.5 Mechanical Response of Gibeon at Low Temperature

Quasi-static tensile tests were conducted on four specimens at low temperatures. To achieve the desired temperature range, liquid nitrogen was utilized to cool the Instron 3119-409 environmental chamber, which can operate between 203 K to 523 K. Four low-temperature tests were carried out at 200 K, 200 K, 205 K, and 206 K, respectively. The temperatures were recorded using a thermocouple attached to each specimen. To ensure temperature stability, the chamber temperature was controlled to reach equilibrium with the temperature of the specimen.

Conducting tests on the Gibeon specimens near 200 K is crucial for understanding their physical and mechanical behavior on the surface of the metal asteroid, specifically on 16 Psyche. The estimated subsolar temperature of 16 Psyche is near 230 K (Landsman et al., 2018; Matter et al., 2013), with a significant day-night temperature variation of approximately 40 K (Marchi et al., 2020). It is well-established that the mechanical properties of iron meteorites are influenced by temperature (Auten, 1973; Gordon, 1970; Johnson and Remo, 1974; Knox, 1970).

The average ultimate tensile strength of the Gibeon specimens was measured to be 391.78 ± 7.7 MPa at 203 ± 2.7 K. The strain to ultimate strength was estimated to be 6.79 ± 0.67% based on the stress-strain response (Figure 57). A significant increase in yield stress of approximately 100 MPa was observed when the temperature was lowered to 203 K. Figure 58a illustrates the effect of temperature change ranging from 206 K to 200 K on the stress-strain response.

All four specimens exhibited ductile behavior (Figure 57). However, compared to failure at ambient temperature (Figure 58b-d), the fracture surface exhibited irregularities, indicating the suppression of dislocation motion and resulting in an irregular and rough fracture boundary. The variations in strain observed in the low-temperature tests suggest the influence of microstructure and the dominant kamacite phase on the failure behavior of the Gibeon specimens. It is worth noting that BCC metals typically undergo a transition from ductile to brittle failure mechanism at low temperatures. The specific temperature at which this transition occurs depends on factors such as mineralogy, composition, grain size, and strain rate (Johnson and Remo, 1974). Generally, the transition temperature for impact testing is higher by 100 K to 200 K than the temperature observed in low-temperature low-strain rate uniaxial tensile tests (Marchi et al., 2020).

The results of all four low-temperature (203 K) experiments conducted on the Gibeon specimens did not show brittle failure. It is estimated that the Gibeon meteorite exhibits ductile to brittle failure at temperatures around 50 K for uniaxial tests but at higher temperatures, around 200 K, for impact events (Johnson and Remo, 1974; Marchi et al., 2020).

All the conducted tensile tests, both at ambient and low temperatures, demonstrated initial grip-slipping, as depicted in the inset of Figure 57. Consequently, the cross-head displacement yielded a low elastic modulus (~ 71.7 GPa for G2). However, when considering the strain measured by DIC, the elastic modulus was calculated to be 131.3 GPa, which closely aligns with the elastic modulus calculated from the elastic wave measurement. Thus, the elastic modulus calculation was performed using DIC strain measurements, enabling the elimination of grip-slipping effects from the experimental data.

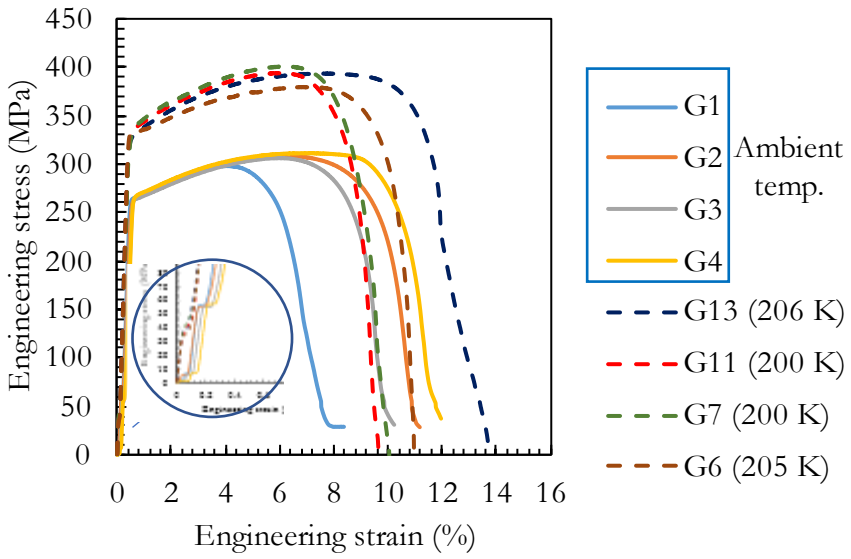

Figure 57. Engineering Stress-strain Response of Gibeon Tensile Sample Both Ambient and Low Temperature. The Yield Strength of the Samples shows an Increase at Low Temperatures Compared to the Ambient Temperature Experiments. The. The Inset Shows the Mechanical Grip Slipping Near the Beginning of the Experiments, Observed at Low Stress for Both Ambient and Low-temperature. Hence Stiffness Is Calculated from the DIC Strain Instead.

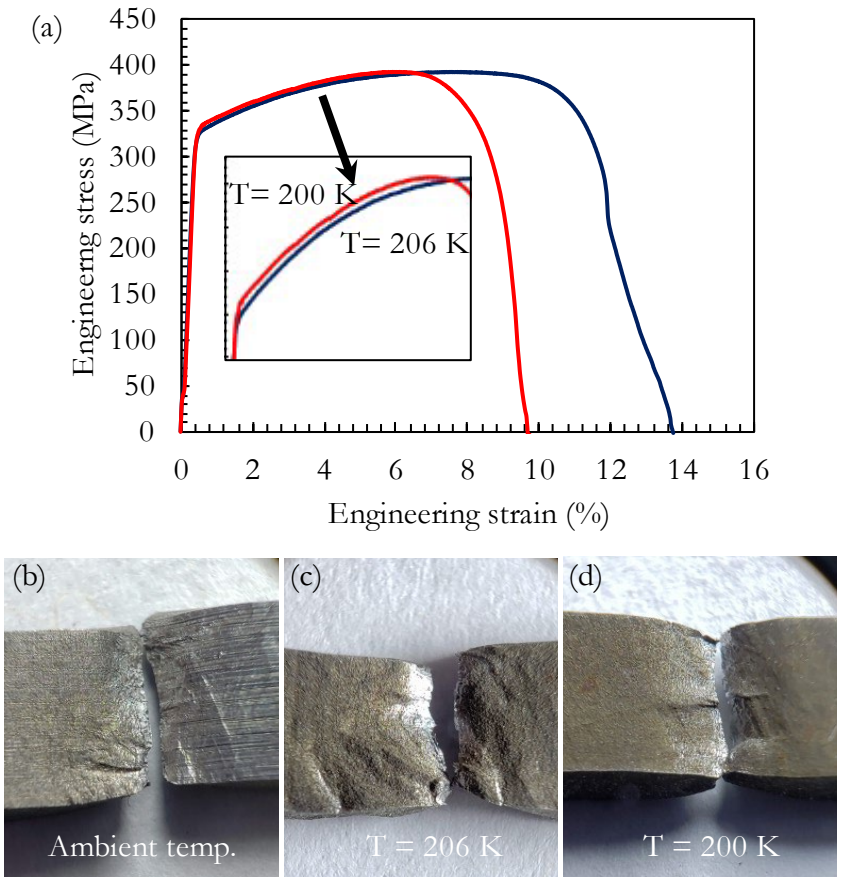

Figure 58. a) Engineering Stress-strain Response of Gibeon Tensile Sample at Low Temperature. A Small Change in Temperature Changes the Yield Strength of the Material. Comparing the Fractography of the Sample (b) G1 at Ambient Temperature, to the Fractography (b) G13 at 206 K, and (c) G11 at 200 K Shows a Relatively Rough Fracture Surface Associated with the Impedance of the Motion of Dislocation due to Low Temperature.

Figure 59 and Figure 60 present the in-situ DIC measurements of displacement and strain during low-temperature tensile experiments for sample G13. As all the tensile samples displayed a similar mechanical response at low temperatures, the G13 sample was chosen to demonstrate the typical behavior using DIC. The displacement contours in the x, y, and z

directions were analyzed to identify regions of elongation and contraction. Near the top of the gauge section, along the y direction, there was a maximum displacement of ~3.72 mm. The z-direction displacement contours at the same location indicate deformation along the thickness, suggesting a potential region of crack nucleation. This observation was further supported by examining the axial strain and equivalent von Mises strain contours. The maximum DIC axial strain recorded was approximately 25.4%, while the DIC equivalent von Mises strain reached around 27.2%. Both strains were found to correspond to the region of maximum y displacement. These strain contours provide information about the potential location of crack nucleation during low-temperature tensile testing.

The Gibeon meteorite tensile specimen (G13) tested at 206 K, yielding a tensile yield strength of 304.6 MPa and an ultimate strength of 393.4 MPa. The strain to failure for this specimen was approximately 7.84%. During testing, the specimen exhibited ductile behavior with diffuse necking, characterized by contraction occurring in both the thickness and width of the specimen, as evident from the equivalent von Mises strain contour. The in-situ DIC measurements, combined with the analysis of displacement and strain, provide insights into the deformation and failure behavior of the Gibeon meteorite during low-temperature tensile testing.

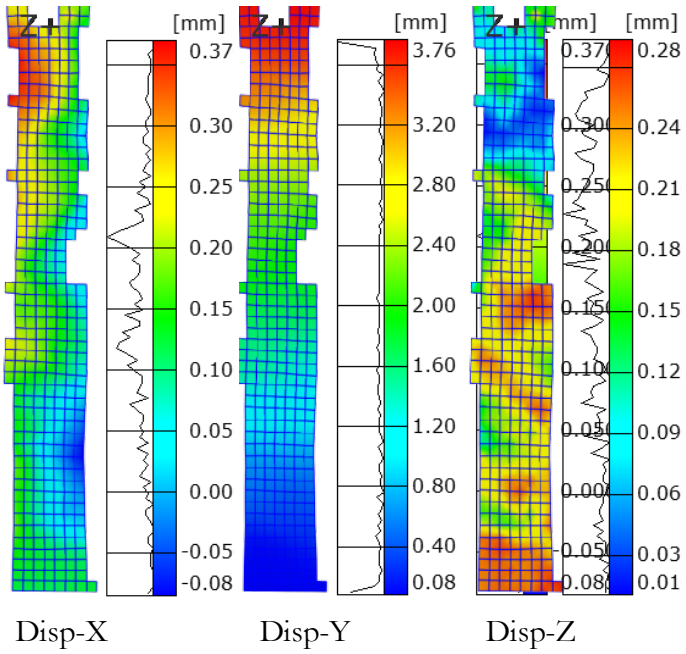

Figure 59. DIC Measurement of the Tensile Sample (G13) at 206 K Shows the Displacement Contour along the X, Y, and Z-axis. The Location of Maximum Displacement Occurs Near the Top of the Gauge Section.

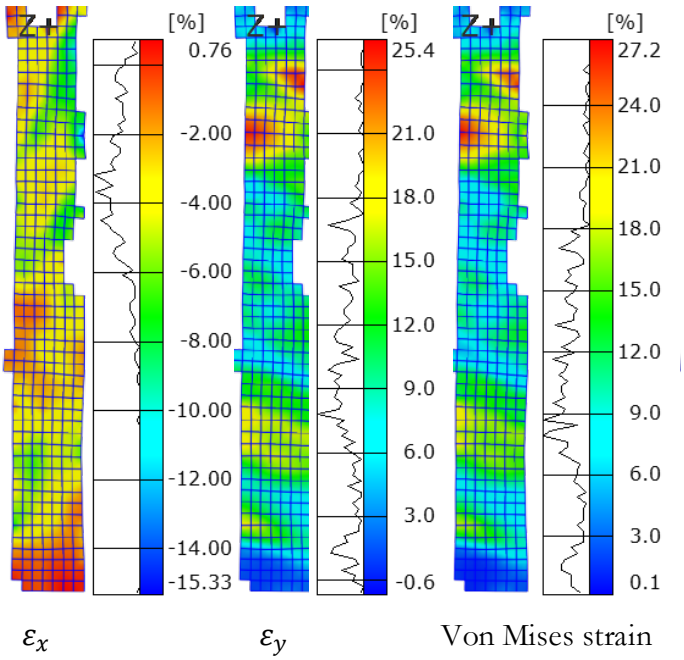

Figure 60. DIC Measurement of the Tensile Sample (G13) at 206 K Shows the Axial, Lateral, and Equivalent von Mises Contours. High von Mises Strain Concentrated near the Top of the Gauge Section of the Sample and Corresponding Shear Strain Contour Provides an Indication of the Location of Crack Nucleation.

4.3.6 Damage Mechanism

Both kamacite and taenite present in Gibeon exhibit plastic deformation (Figure 61). Micrographs of a compressed sample show the elongation of the Widmanstätten pattern perpendicular to the loading direction (Figure 61 and Figure 62), with the applied load mainly supported by kamacite, followed by taenite due to its greater ductility and higher strength and hardness (Knox, 1970; Ueki et al., 2021). Chemical analysis using an electron microprobe analyzer was carried out on the compressed sample, with four locations identified (Figure 62), and their corresponding chemical compositions are shown in Table 14. Higher nickel percentages at points 1, 3, and 4 indicate taenite, while point 2 with a lower nickel represents kamacite. Compressed samples exhibit a wavy and relatively linear morphology in kamacite and taenite along the compression direction. Taenite appears as a film between the kamacite lamella. So, observing deformation in the taenite is often challenging. Relatively small deformation in taenite suggests that dislocation movement responsible for failure initiation likely occurred in kamacite. Images of the fracture surface from the tensile specimens reveal that they slipped along the plane of shear, with a smooth edge appearing on the fracture surface (Figure 64). Optical and scanning electron micrographs are consistent with the DIC strain contours.

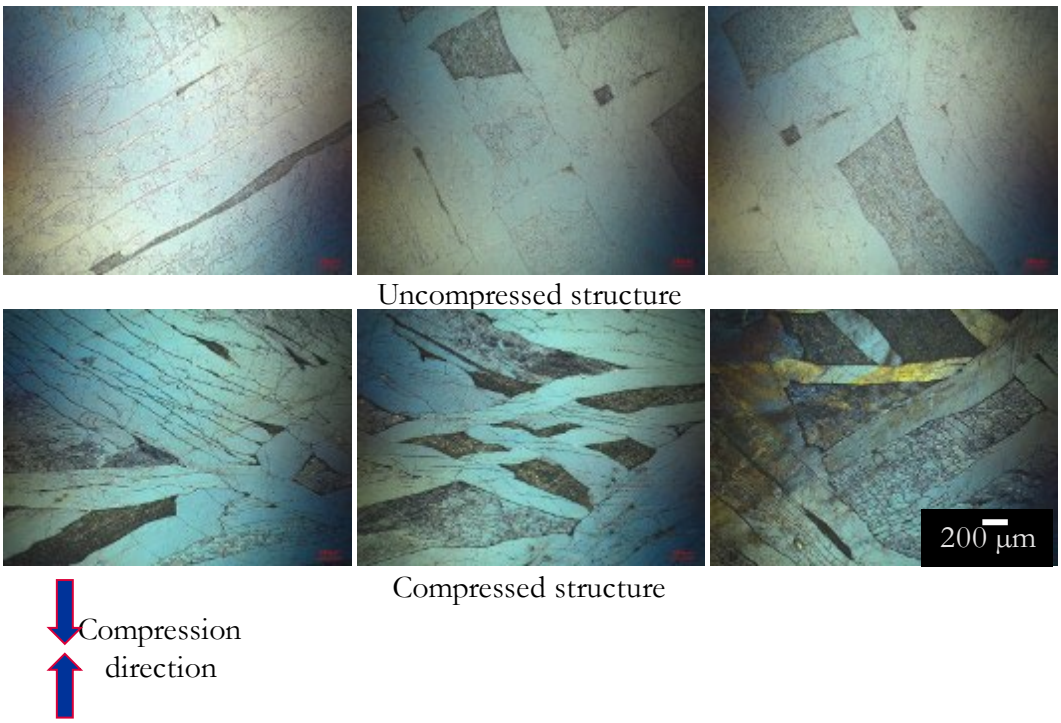

Figure 61. A Comparison of the Compressed (G1, G2, and G3) and Uncompressed (G1, G2, and G3) Widmanstätten Patterns at Different Locations Before and after the Quasi-static Uniaxial Compression Reveals Deformation in the Kamacite and Taenite Phases.

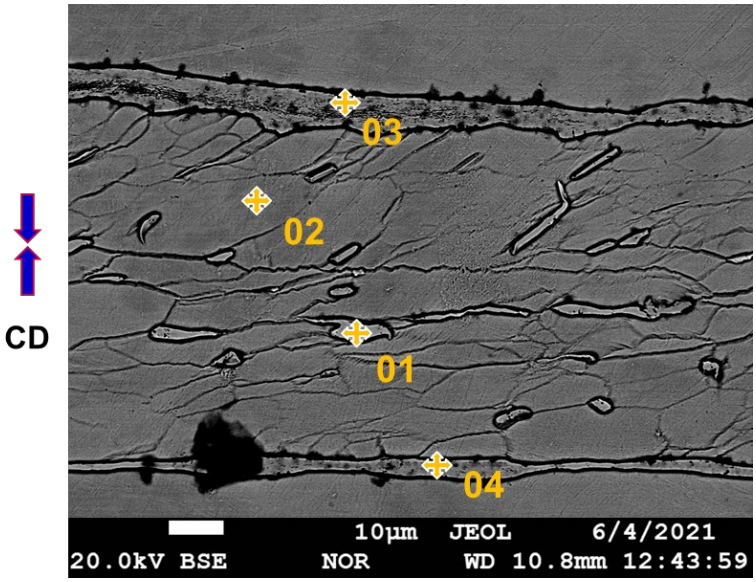

Figure 62. SEM Image Shows the Kamacite and Taenite Interface of a Compressed Gibeon Cube. The Composition of Fe-Ni at Different Points Is Indicated in Table 13 to Illustrate the Kamacite, Taenite, and Plessite. Taenite Grains are Enclosed within Plessite, and the Plessite is Bounded by Taenite. In the Taenite Region, the Kamacite is Polycrystalline.

Table 14. Elemental Composition of the Selected Points of the Compressed Sample.

Points	**Fe (wt.%)**	**Ni (wt.%)**	**O (wt.%)**
01	65.55	34.45	
02	93.01	6.99	
03	75.96	21.65	2.39
04	66.75	26.98	6.26

Many shear bands were observed on the kamacite laths, which, in several kamacite lamellae, formed near 45° to the loading direction (Figure 63). Since the yield strength of taenite is almost twice that of kamacite (Ueki, 2021), during tensile loading, deformation was observed to initiate from the wider kamacite laths, likely with low twin boundaries (Neumann bands). High-strength taenite on kamacite boundaries and Neumann bands resist deformation by blocking the dislocation movement in those kamacite laths, resulting in strain hardening that shows up in the stress-strain curve. Also, deformation continues for the smaller kamacite grains that show very fine taenite boundaries and apparently without Neumann bands in the plessite region (Figure 63). At ultimate strength, slipping occurs along the plane of shear and initiates cracks from the kamacite in plessite regions, which eventually results in ductile failure (Figure 64).

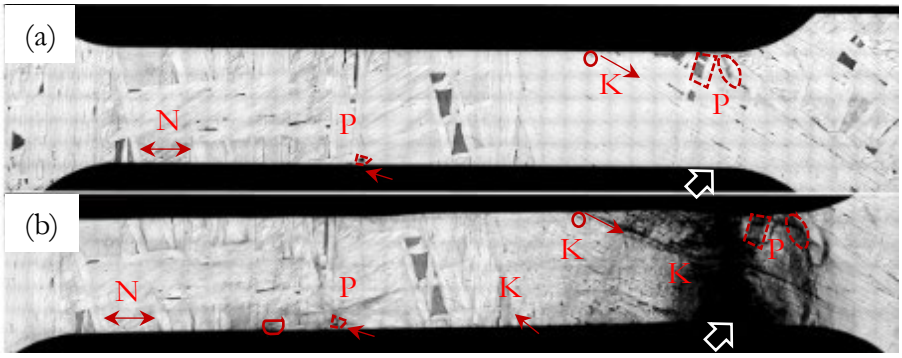

Figure 63. The Optical Image of an Etched Tensile Sample Reveals the Distinct Widmanstätten Pattern and Deformation Characteristics. In (a) and (b), the Images Illustrate the Sample Before and after the Quasi-static Tensile Test, respectively. Notably, Red Marks Are Used to Highlighting Various Features Within the Tensile Specimens, Including the Concentration of Neumann Bands (N), the Location of Plessite (P), and Kamacite Lamellae (K) in the Gauge Region. A Comparison of the Deformation in the Damaged Specimen Is Also Illustrated. Furthermore, the Black Arrow Indicates the Location of the Fracture Surface.

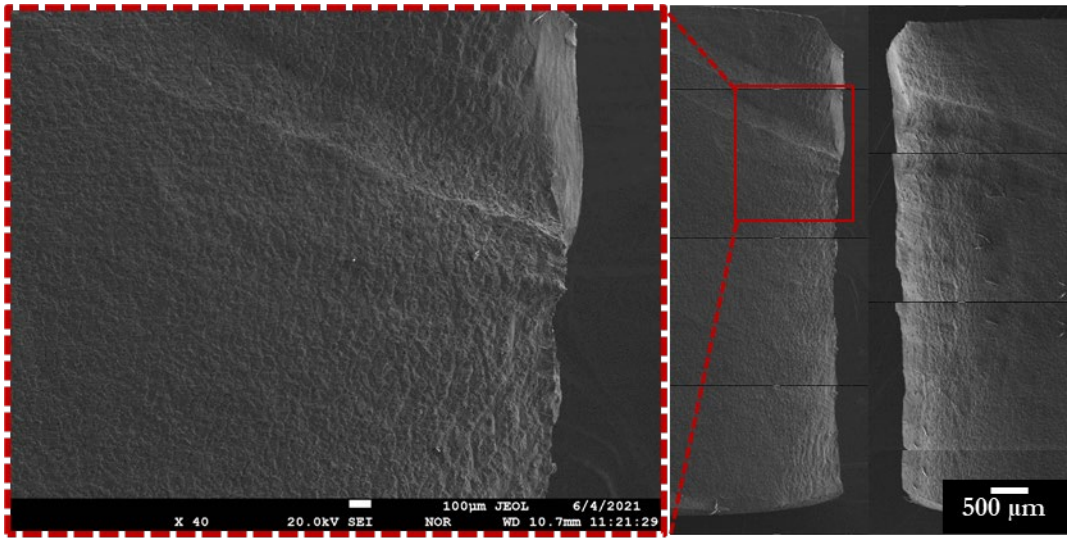

Figure 64. SEM Image of a Tensile Sample Showing a Deformation Band on the Fracture Surface (in Red Box) and Fracture Surfaces from the Top and Bottom Part of the Sample.

A combination of zigzagged and slant fracture surfaces that characterize cup and cone fracture, commonly referred to as diffuse necking, was observed in the Gibeon specimen following the tensile experiments (Figure 65). This diffused necking involves the contraction of both the thickness and width of the specimen. Figure 58 (b-d) displays the zigzagged and slant fracture surfaces resulting from the necking behavior observed during ambient and low-temperature tensile testing. Additionally, the von Mises equivalent strain obtained from DIC analysis highlights the localized formation of necking as a consequence of thickness reduction along the +Z direction (Figure 54 and Figure 60). The thickness of the specimen continues to decrease under the applied tensile load, while the width along the necking region remains relatively unchanged. Simultaneously, shear bands begin to form, potentially triggered by microstructural inhomogeneity, which concentrates deformation in a narrow region and hinders dislocation motion (Gilman, 1994; Yadav and Sagapuram, 2020).

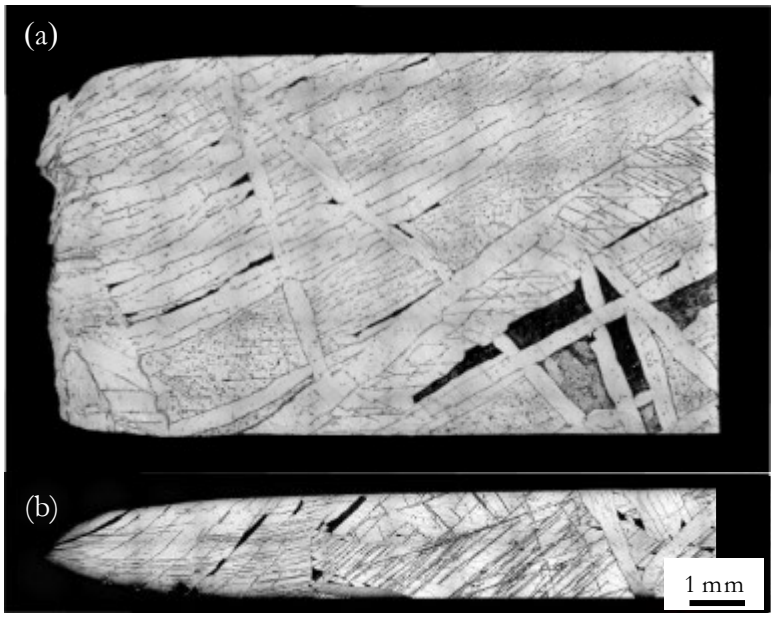

Figure 65. Optical Image of the Etched Fracture Surface of the Tensile Sample Showing Deformation of the Widmanstätten Pattern from the (a) Top and (b) Side of the Specimen (G3).

The Gibeon meteorite is primarily composed of ~95% kamacite, plessite, and taenite, which exhibit similar mechanical properties and demonstrate ductile behavior under tensile loading at a given temperature (Johnson and Remo, 1974). However, the single-crystal taenite within the meteorite displays superior strength and toughness compared to kamacite (Ueki et al., 2021). The discrepancy in mechanical properties between kamacite and taenite can result in stress concentration at the interface between these phases (Figure 66). The DIC analysis revealed that strain tends to concentrate along the kamacite lamellae, indicating that plastic deformation and damage in the Gibeon meteorite are primarily governed by the relatively low strength and toughness of the kamacite phase.

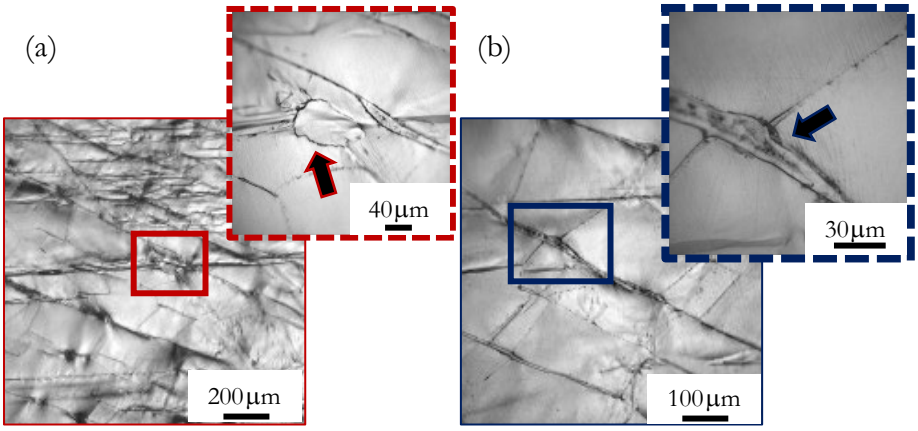

Figure 66. Optical Image of the Etched Fracture Surface of the Tensile Sample Showing Deformation of the Widmanstätten Pattern Where (a) Crack Nucleates from the Kamacite and Taenite Boundary and (b) Slip Bands Observed in Kamacite. Slip Bands Are Oriented along the Same Direction in All Similar-oriented Kamacite Lamella.

In the BCC crystalline structure of kamacite, there can be at least 12 slip systems, consisting of 6 slip planes and 2 slip directions. On the other hand, the face-centered cubic (FCC) crystalline structure of taenite has 12 slip systems, with 4 slip planes and 3 slip directions (He et al., 2005). Although kamacite has a cubic crystal structure and more slip systems, the crystal structure of BCC kamacite is not as closely packed as FCC taenite. This results in increased lattice friction, which in turn leads to reduced ductility and a higher propensity for dislocation pileup in BCC kamacite (Pineau et al., 2016). The less favorable packing arrangement in kamacite makes it more prone to dislocation entanglement and hindered dislocation motion, limiting its ability to undergo plastic deformation. According to Schmid's law, slip or dislocation glide occurs when the critically resolved shear stress on a slip plane exceeds a critical value.

Additionally, the activation of multiple slip systems at higher stress levels contributes to increased strain hardening, as observed in compression and tension experiments. The activation of multiple slip systems allows for a greater distribution of deformation, leading to different strain-hardening responses and strain to failure. However, the less ductile nature of BCC kamacite compared to FCC taenite can result in a more localized strain concentration, increasing the likelihood of shear band formation and localized plastic instability. Furthermore, the average length of these slip bands, formed by the accumulation of dislocations, also depends on the material's microstructure. The relationship between yield stress (σ_y) and the kamacite lamellae diameter or width (l) can be described by the empirical Hall-Petch equation (Johnson and Remo 1974):

$$\sigma_y = \sigma_0 + k_y * l^{-\frac{1}{2}} \tag{4.1}$$

Here, σ_0 represents the material constant associated with the initial stress required for dislocation motion, k_y is the strengthening coefficient, and l refers to the diameter or width of the lamellae in octahedrite materials. This relation highlights the significant influence of the microstructure of Gibeon on the observed variation in yield strength during compression and tension. Moreover, the presence of mechanical twins, commonly referred to as Neumann bands, acts as obstacles to dislocation motion, impeding the formation of shear bands. This phenomenon can contribute to variations in the strain hardening rate and yield strength. Ultimately, it leads to plastic instability, which is evident from the occurrence of zigzagged fractures in the Gibeon specimens. The interaction between the microstructure, mechanical twins, and dislocation motion plays a crucial role in the overall mechanical behavior and failure characteristics of the material.

4.4 Summary

The mechanical behavior and damage mechanism of the Gibeon meteorite were investigated through a combination of quasi-static mechanical tests under compression and tension conditions, along with in-situ full-field DIC analyses. Quasi-static compression tests were conducted at ambient temperature, while quasi-static tensile tests were performed at both ambient and low temperatures. The inclusion of DIC measurements allowed for a comprehensive understanding of the influence of temperature on the material's mechanical response and damage mechanism.

Both compression and tensile specimens exhibited significant ductile deformation within the Widmanstätten pattern. The Gibeon meteorite demonstrated a higher mean compressive yield strength of 308 ± 64.9 MPa compared to the mean tensile yield strength of 255.6 ± 3.7 MPa. In compression samples, no significant fracture surfaces were observed even at strain ranges from 30% to 50%. On the other hand, tensile samples exhibited diffuse necking leading to failure, with an average ultimate strength of 305.7 ± 4.6 MPa and a failure strain of 6.3 ± 0.95%. At low temperatures (-70.3 ± 2.7°C), the ultimate tensile strength increased to 391.78 ± 7.7 MPa. DIC strain contours were utilized to identify the locations of damaged nucleation and propagation in the specimens, providing insights into the deformation patterns leading to fracture.

Post-failure surface analysis using optical and scanning electron microscopes revealed deformation marks on the kamacite phases and shear bands on the fracture planes. While taenite exhibited plastic deformation, some regions exhibited a serrated boundary between the kamacite and taenite. Overall, the bulk failure mechanism observed in the mechanical response

and fractography was predominantly governed by the kamacite, with limited apparent influence from the surrounding taenite. These findings align well with the strain localization patterns observed in the DIC strain contours.

The characterization of strength and failure behavior in the Gibeon meteorite, as demonstrated through the utilization of DIC techniques, provides valuable insights into the physical and mechanical properties of iron meteorites. This work enhances our understanding of the strength and failure of iron-rich bodies, contributing to the broader understanding of the formation, collisions, and disintegration of planetary bodies.

CHAPTER 5

CONTRIBUTION AND FUTURE WORK

5.1 Contribution

This research advances our understanding of the strength and fracture properties of meteorites, which is crucial for accurately assessing their behavior during entry and impact on Earth, and for hazard mitigation strategies. The study highlights the need to directly study meteorites to better comprehend their unique bulk properties and by extension, the asteroids from which they came from. However, relying solely on our knowledge of terrestrial rocks may lead to inaccurate estimations of meteoroid survivability. By investigating the mineralogy, physical properties, and elastic properties of meteorites, this research emphasizes the importance of comprehending their mechanical properties. The findings of this work serve as a gateway to gaining deeper insights into the fundamental physical and mechanical characteristics of early solar system materials. To advance our understanding of meteorites and extend our knowledge to Near-Earth Objects (NEOs), this study focuses specifically on stony and iron meteorites. This work systematically investigates their physical and mechanical properties and their fracture behavior. The mechanical properties and microstructural characteristics of two stony meteorites, Aba Panu (L3) and Viñales (L6) meteorites are analyzed at ambient temperature, while the mechanical behavior of the Gibeon (IVA) iron meteorite is examined at ambient and low temperatures. The findings of this study reveal that the Aba Panu meteorite exhibits higher strength compared to previously studied ordinary chondrites. The microstructural analysis indicates the presence of a heterogeneous microstructure with spatial variations in the mineralogy and crack distribution. Both the Aba

Panu and Viñales meteorites demonstrate axial splitting under quasi-static compression. The correlative study of the Aba Panu meteorite identifies strong load-bearing phases such as olivine and pyroxene, as well as weak phases like troilite. For the Viñales meteorite, the correlation between crack nucleation and the distribution of metals and shock-melt veins remains inconclusive. The Gibeon iron meteorite exhibits higher compressive yield strength compared to tensile yield strength. Under compression, no significant fracture surfaces are observed even at high strain ranges, while under tension, diffuse necking occurs, leading to ductile failure. The deformation patterns and failure mechanisms observed are influenced by the kamacite. The following achievements summarize the significant contributions of this research:

- Characterized the bulk chemical, physical, and mechanical properties of the ordinary chondrites Aba Panu (L3) and Viñales (L6) and the iron meteorite Gibeon (IVA) to understand the physical and mechanical behavior of NEOs with similar compositions.
- Investigated the dominant mineral phases of chondritic and iron meteorites through correlative studies involving chemical analysis using the electron microprobe analyzer, structural and textural analysis using X-ray microtomography, and micromechanical properties using nanoindentation. This investigation facilitated a deeper understanding of their strength and fracture behaviors.
- Examined the failure mechanisms in stony and iron meteorites using non-contact in-situ 3-D DIC, which employed full-field displacement and strain analysis, to assess the role of the complex microstructure on failure mechanisms. Also, utilized

X-CT to analyze the influence of metals, including their distribution and structure, on failure initiation under compressive loads for chondritic meteorites.

- Characterized the fracture-related mechanical properties of stony and iron meteorites, including failure strength, failure mode, and fracture behavior. Additionally, the temperature-dependent mechanical behavior of iron meteorites under tensile loads was investigated.
- Developed in-situ low-temperature testing for iron meteorites and studied the response of unique microstructure and failure of iron meteorites.

By advancing our understanding of meteorite properties and their strength and fracture behavior, this research significantly contributes to our knowledge of the physical characteristics and behavior of Near-Earth Objects (NEOs), which can give insights into the breakup, fragmentation, and survivability of asteroidal materials when they reach Earth. The establishment of the strength-scale dependence is crucial for addressing the effects of strength selection in meteorite falls and findings. Additionally, this study investigates the physical and mechanical properties, including stress-strain response and post-peak behavior, providing the knowledge base necessary for quantitative predictions for asteroid disruption and deflection models. The findings from this research have implications for the field of planetary science, as they help in assessing the potential risks associated with asteroid impacts on Earth and improving our overall understanding of these celestial events.

5.2 Future work

This research establishes a framework for investigating the microstructural, mineralogical, and physical properties of ordinary chondrite and iron meteorites, along with their

corresponding mechanical responses and fracture behaviors. However, it is important to note that the study only examines two L ordinary chondrites and one iron meteorite, which may not fully represent the full range of variability in meteorite properties. This highlights the need for future studies to include a larger sample size and consider samples from different meteorite falls, encompassing a wider range of ordinary chondrites, including L- and H-chondrites, as well as carbonaceous chondrites.

The microstructural and mineralogical complexity formed during the early solar system can lead to variations in the physical and mechanical behavior between different meteorite types. Therefore, future research should aim to explore the relationship between microstructural features and mechanical properties in a more systematic manner. This can be achieved through the use of advanced imaging techniques and analytical methods, which can provide deeper insights into the correlation between crack nucleation, metal and troilite distribution, and shock-melt veins, especially in meteorites like Viñales where the relationship remains uncertain.

To enhance our understanding of the mechanical behavior of meteorites, it would be valuable to incorporate quantitative analysis techniques such as finite element modeling or statistical analysis. These approaches can help develop robust physics-based models that can predict damage initiation and propagation under static or dynamic loadings. Such models are crucial for improving our ability to develop effective asteroid deflection and hazard mitigation strategies.

In addition to studying meteorites at room temperature, it is important to investigate their mechanical behaviors under the temperature conditions experienced by asteroids in the

asteroid belt. The diurnal temperature variations in the asteroid belt differ from those on Earth, and understanding the temperature effects on the strength of meteorites is therefore essential for comprehending the physical behavior of asteroids within the asteroid belt. The temperature-dependent study presented in Chapter 4 provides key insights and can be applied to evaluate the mechanical response and failure mechanisms of other meteorites under different temperature conditions.

These research findings have significant relevance to several NASA studies and contribute to the scientific community's understanding of meteorites. However, it is important to acknowledge the limitations of the current study and continue to explore and expand our knowledge through future research endeavors.

REFERENCES

Abdulqader, A., Rizos, D.C., 2020. Advantages of using digital image correlation techniques in uniaxial compression tests. Results Eng. 6, 100109. https://doi.org/10.1016/j.rineng.2020.100109

Ahles, A.A., Emery, J.D., Dunand, D.C., 2021. Mechanical properties of meteoritic Fe–Ni alloys for in-situ extraterrestrial structures. Acta Astronaut. 189, 465–475. https://doi.org/10.1016/j.actaastro.2021.09.001

Ashley, J.W., Golombek, M.P., Christensen, P.R., Squyres, S.W., McCoy, T.J., Schroeder, C., Fleischer, I., Johnson, J.R., Herkenhoff, K.E., Parker, T.J., 2011. Evidence for mechanical and chemical alteration of iron-nickel meteorites on Mars: Process insights for Meridiani Planum. https://doi.org/10.1029/2010JE003672

Auten, T.A., 1973. ON THE BRITTLENESS OF GIBEON METEORITIC IRON. Meteoritics 8, 189–196. https://doi.org/10.1111/j.1945-5100.1973.tb01247.x

Baker, D.R., Mancini, L., Polacci, M., Higgins, M.D., Gualda, G.A.R., Hill, R.J., Rivers, M.L., 2012. An introduction to the application of X-ray microtomography to the three-dimensional study of igneous rocks. Lithos 148, 262–276. https://doi.org/10.1016/j.lithos.2012.06.008

Bardestani, R., Patience, G.S., Kaliaguine, S., 2019. Experimental methods in chemical engineering: specific surface area and pore size distribution measurements—BET, BJH, and DFT. Can. J. Chem. Eng. 97, 2781–2791.

Benz, W., Asphaug, E., 1999. Catastrophic disruptions revisited. Icarus 142, 5–20. https://doi.org/10.1006/icar.1999.6204

Bieniawski, Z.T., Bernede, M.J., 1979. Suggested methods for determining the uniaxial compressive strength and deformability of rock materials: Part 1. Suggested method for determining deformability of rock materials in uniaxial compression. Int. J. Rock Mech. Min. Sci. Geomech. Abstr. 16, 138–140. https://doi.org/10.1016/0148-9062(79)91451-7

Binzel, R.P., Lupishko, D.F., Di Martino, M., Whiteley, R.J., Hahn, G.J., 2002. Physical properties of near-Earth objects. Asteroids III 255.

Binzel, R.P., Reddy, V., Dunn, T., 2015. The near-Earth object population: Connections to comets, main-belt asteroids, and meteorites. Asteroids IV 1, 243.

Birch, F., 1961. The Velocity of Compressional Waves in Rocks to 10 Kilobars, Part 2. J. Geophys. Res. 66, 2199–2224. https://doi.org/10.1029/JZ066i007p02199

Blum, J., Schräpler, R., Davidsson, B.J.R., Trigo-Rodríguez, J.M., 2006. The Physics of Protoplanetesimal Dust Agglomerates. I. Mechanical Properties and Relations to

Primitive Bodies in the Solar System. Astrophys. J. 652, 1768. https://doi.org/10.1086/508017

Bobet, A., Einstein, H., 1998. Fracture coalescence in rock-type materials under uniaxial and biaxial compression. Int. J. Rock Mech. Min. Sci. 35, 863–888.

Borodich, F.M., 1999. Fractals and fractal scaling in fracture mechanics. Int. J. Fract. 95, 239–259.

Bottke Jr, W.F., Cellino, A., Paolicchi, P., Binzel, R.P., 2002. An overview of the asteroids: the asteroids III perspective. Asteroids III 1, 3–15.

Bottke, W.F., Cellino, A., Paolicchi, P., Binzel, R.P. (Eds.), 2002. Asteroids III. University of Arizona Press. https://doi.org/10.2307/j.ctv1v7zdn4

Britt, D.T., Consolmagno, G.J.S.J., 2003. Stony meteorite porosities and densities: A review of the data through 2001. Meteorit. Planet. Sci. 38, 1161–1180. https://doi.org/10.1111/j.1945-5100.2003.tb00305.x

Brownlee, D., 2014. The Stardust mission: analyzing samples from the edge of the solar system. Annu. Rev. Earth Planet. Sci. 42, 179–205.

Brusnitsina, E., Muftakhetdinova, R., Yakovlev, G., Grokhovsky, V., 2019. Nanoindentation of Phase and Structural Components of Pallasite Seymchan (PMG). KnE Eng. 1, 34. https://doi.org/10.18502/keg.v1i1.4388

Buchwald, V.F., 1975. Handbook of iron meteorites. Their history, distribution, composition and structure. Ariz. State Univ.

Buddhue, J.D., 1957. The oxidation and weathering of meteorites. Univ. N. M. Press No. 3.

Buddhue, J.D., 1942. The Compressive Strength of Meteorites. Contrib. Soc. Res. Meteor. 3, 39–40. https://doi.org/10.1111/j.1945-5100.1942.tb00140.x

Bunge, H.J., Weiss, W., Klein, H., Wcislak, L., Garbe, U., Schneider, J.R., 2003. Orientation relationship of Widmannstätten plates in an iron meteorite measured with high-energy synchrotron radiation. J. Appl. Crystallogr. 36, 137–140. https://doi.org/10.1107/S0021889802021386

Carlson, W.D., Rowe, T., Ketcham, R.A., Colbert, M.W., 2003. Applications of high-resolution X-ray computed tomography in petrology, meteoritics and palaeontology. Geol. Soc. Lond. Spec. Publ. 215, 7–22.

Carry, B., 2012. Density of asteroids. Planet. Space Sci. 73, 98–118. https://doi.org/10.1016/j.pss.2012.03.009

Cayron, C., 2014. EBSD imaging of orientation relationships and variant groupings in different martensitic alloys and Widmanstätten iron meteorites. Mater. Charact. 94, 93–110. https://doi.org/10.1016/j.matchar.2014.05.015

Cheng, A.F., Agrusa, H.F., Barbee, B.W., Meyer, A.J., Farnham, T.L., Raducan, S.D., Richardson, D.C., Dotto, E., Zinzi, A., Della Corte, V., Statler, T.S., Chesley, S., Naidu, S.P., Hirabayashi, M., Li, J.-Y., Eggl, S., Barnouin, O.S., Chabot, N.L., Chocron, S., Collins, G.S., Daly, R.T., Davison, T.M., DeCoster, M.E., Ernst, C.M., Ferrari, F., Graninger, D.M., Jacobson, S.A., Jutzi, M., Kumamoto, K.M., Luther, R., Lyzhoft, J.R., Michel, P., Murdoch, N., Nakano, R., Palmer, E., Rivkin, A.S., Scheeres, D.J., Stickle, A.M., Sunshine, J.M., Trigo-Rodriguez, J.M., Vincent, J.-B., Walker, J.D., Wünnemann, K., Zhang, Y., Amoroso, M., Bertini, I., Brucato, J.R., Capannolo, A., Cremonese, G., Dall'Ora, M., Deshapriya, P.J.D., Gai, I., Hasselmann, P.H., Ieva, S., Impresario, G., Ivanovski, S.L., Lavagna, M., Lucchetti, A., Epifani, E.M., Modenini, D., Pajola, M., Palumbo, P., Perna, D., Pirrotta, S., Poggiali, G., Rossi, A., Tortora, P., Zannoni, M., Zanotti, G., 2023. Momentum Transfer from the DART Mission Kinetic Impact on Asteroid Dimorphos. Nature 1–3. https://doi.org/10.1038/s41586-023-05878-z

Chu, T.C., Ranson, W.F., Sutton, M.A., 1985. Applications of digital-image-correlation techniques to experimental mechanics. Exp. Mech. 25, 232–244. https://doi.org/10.1007/BF02325092

Consolmagno, G.J., Britt, D.T., Macke, R.J., 2008. The significance of meteorite density and porosity. Geochemistry 68, 1–29. https://doi.org/10.1016/j.chemer.2008.01.003

Consolmagno S.J., G.J., Britt, D.T., Stoll, C.P., 1998. The porosities of ordinary chondrites: Models and interpretation. Meteorit. Planet. Sci. 33, 1221–1229. https://doi.org/10.1111/j.1945-5100.1998.tb01307.x

Cotto-Figueroa, D., Asphaug, E., Garvie, L.A.J., Rai, A., Johnston, J., Borkowski, L., Datta, S., Chattopadhyay, A., Morris, M.A., 2016. Scale-dependent measurements of meteorite strength: Implications for asteroid fragmentation. Icarus 277, 73–77. https://doi.org/10.1016/j.icarus.2016.05.003

Cotto-Figueroa, D., Rabbi, M.F., Garvie, L.A., Asphaug, E., Gabriel, T., Khafagy, K.H., Chattopadhyay, A., 2021. On the Strength of the Viñales (L6) Meteorite: A Test of the Robustness of the Derived Strength Scale-dependence of Ordinary Chondrites. Presented at the AAS/Division for Planetary Sciences Meeting Abstracts, pp. 303–04.

Cotto-Figueroa, D., Rabbi, M.F., Rai, A., Chattopadhyay, A., Garvie, L.A.J., Asphaug, E., 2019. On the Strength of the Aba Panu (L3) Meteorite: Implications for Hazard Mitigation. Presented at the EPSC-DPS Joint Meeting 2019, p. 2.

Council, N.R., Sciences, D. on E. and P., Board, A. and S.E., Board, S.S., Strategies, C. to R.N.-E.-O.S. and H.M., 2010. Defending Planet Earth: Near-Earth-Object Surveys and Hazard Mitigation Strategies. National Academies Press.

Daly, R.T., Ernst, C.M., Barnouin, O.S., Chabot, N.L., Rivkin, A.S., Cheng, A.F., Adams, E.Y., Agrusa, H.F., Abel, E.D., Alford, A.L., Asphaug, E.I., Atchison, J.A., Badger, A.R., Baki, P., Ballouz, R.-L., Bekker, D.L., Bellerose, J., Bhaskaran, S., Buratti, B.J., Cambioni, S., Chen, M.H., Chesley, S.R., Chiu, G., Collins, G.S., Cox, M.W., DeCoster, M.E., Ericksen, P.S., Espiritu, R.C., Faber, A.S., Farnham, T.L., Ferrari, F., Fletcher, Z.J., Gaskell, R.W., Graninger, D.M., Haque, M.A., Harrington-Duff, P.A., Hefter, S., Herreros, I., Hirabayashi, M., Huang, P.M., Hsieh, S.-Y.W., Jacobson, S.A., Jenkins, S.N., Jensenius, M.A., John, J.W., Jutzi, M., Kohout, T., Krueger, T.O., Laipert, F.E., Lopez, N.R., Luther, R., Lucchetti, A., Mages, D.M., Marchi, S., Martin, A.C., McQuaide, M.E., Michel, P., Moskovitz, N.A., Murphy, I.W., Murdoch, N., Naidu, S.P., Nair, H., Nolan, M.C., Ormö, J., Pajola, M., Palmer, E.E., Peachey, J.M., Pravec, P., Raducan, S.D., Ramesh, K.T., Ramirez, J.R., Reynolds, E.L., Richman, J.E., Robin, C.Q., Rodriguez, L.M., Roufberg, L.M., Rush, B.P., Sawyer, C.A., Scheeres, D.J., Scheirich, P., Schwartz, S.R., Shannon, M.P., Shapiro, B.N., Shearer, C.E., Smith, E.J., Steele, R.J., Steckloff, J.K., Stickle, A.M., Sunshine, J.M., Superfin, E.A., Tarzi, Z.B., Thomas, C.A., Thomas, J.R., Trigo-Rodríguez, J.M., Tropf, B.T., Vaughan, A.T., Velez, D., Waller, C.D., Wilson, D.S., Wortman, K.A., Zhang, Y., 2023. Successful Kinetic Impact into an Asteroid for Planetary Defense. Nature 1–3. https://doi.org/10.1038/s41586-023-05810-5

Dibb, S.D., Bell III, J.F., Elkins-Tanton, L.T., Williams, D.A., 2023. Visible to Near-Infrared Reflectance Spectroscopy of Asteroid (16) Psyche: Implications for the Psyche Mission's Science Investigations. Earth Space Sci. 10, e2022EA002694. https://doi.org/10.1029/2022EA002694

Dionnet, Z., Brunetto, R., Aléon-Toppani, A., Rubino, S., Baklouti, D., Borondics, F., Buellet, A.-C., Djouadi, Z., King, A., Nakamura, T., Rotundi, A., Sandt, C., Troadec, D., Tsuchiyama, A., 2020a. Combining IR and X-ray microtomography data sets: Application to Itokawa particles and to Paris meteorite. Meteorit. Planet. Sci. 55, 1645–1664. https://doi.org/10.1111/maps.13538

Dionnet, Z., Suttle, M.D., Longobardo, A., Rotundi, A., Folco, L., Corte, V.D., King, A., 2020b. X-ray computed tomography: Morphological and porosity characterization of giant Antarctic micrometeorites. Meteorit. Planet. Sci. 55, 1581–1599. https://doi.org/10.1111/maps.13533

Dotto, E., Della Corte, V., Amoroso, M., Bertini, I., Brucato, J., Capannolo, A., Cotugno, B., Cremonese, G., Di Tana, V., Gai, I., 2021. LICIACube-the Light Italian Cubesat for Imaging of Asteroids in support of the NASA DART mission towards asteroid (65803) Didymos. Planet. Space Sci. 199, 105185.

Dunn, T.L., Cressey, G., McSWEEN Jr, H.Y., McCOY, T.J., 2010. Analysis of ordinary chondrites using powder X-ray diffraction: 1. Modal mineral abundances. Meteorit. Planet. Sci. 45, 123–134.

Durda, D.D., Chapman, C.R., Cintala, M.J., Flynn, G.J., Strait, M.M., Minnick, A., 2011. Experimental investigation of the impact fragmentation of blocks embedded in

regolith. Meteorit. Planet. Sci. 46, 149–155. https://doi.org/10.1111/j.1945-5100.2010.01163.x

Dyaur, N., Stewart, R.R., Cassidy, M.M., 2020. Elastic properties of Iron Meteorites. Presented at the Lunar and Planetary Science Conference, p. 3063.

Ebel, D.S., Rivers, M.L., 2007. Meteorite 3-D synchrotron microtomography: Methods and applications. Meteorit. Planet. Sci. 42, 1627–1646. https://doi.org/10.1111/j.1945-5100.2007.tb00595.x

Elkins-Tanton, L.T., Asphaug, E., Bell, J.F., Bercovici, H., Bills, B., Binzel, R., Bottke, W.F., Dibb, S., Lawrence, D.J., Marchi, S., McCoy, T.J., Oran, R., Park, R.S., Peplowski, P.N., Polanskey, C.A., Prettyman, T.H., Russell, C.T., Schaefer, L., Weiss, B.P., Wieczorek, M.A., Williams, D.A., Zuber, M.T., 2020. Observations, Meteorites, and Models: A Preflight Assessment of the Composition and Formation of (16) Psyche. J. Geophys. Res. Planets 125. https://doi.org/10.1029/2019JE006296

Emmett, P., 1946. Multilayer adsorption equations. J. Am. Chem. Soc. 68, 1784–1789.

Endress, M., Zinner, E., Bischoff, A., 1996. Early aqueous activity on primitive meteorite parent bodies. Nature 379, 701–703.

Epstein, B., 1948. Statistical aspects of fracture problems. J. Appl. Phys. 19, 140–147.

Farahani, B.V., Amaral, R., Tavares, P.J., Moreira, P.M., Santos, A. dos, 2020. Material characterization and damage assessment of an AA5352 aluminium alloy using digital image correlation. J. Strain Anal. Eng. Des. 55, 3–19. https://doi.org/10.1177/0309324719892727

Farbaniec, L., Chapman, D.J., Patten, J.R.W., Smith, L.C., Hogan, J.D., Rack, A., Eakins, D.E., 2021. In-situ visualisation of dynamic fracture and fragmentation of an L-type ordinary chondrite by combined synchrotron X-ray radiography and microtomography. Icarus 359, 114346. https://doi.org/10.1016/j.icarus.2021.114346

Flynn, G.J., 2006. PHYSICAL PROPERTIES OF METEORITES AND INTERPLANETARY DUST PARTICLES: CLUES TO THE PROPERTIES OF THE METEORS AND THEIR PARENT BODIES. Earth Moon Planets 95, 361–374. https://doi.org/10.1007/s11038-005-9025-y

Flynn, G.J., Consolmagno, G.J., Brown, P., Macke, R.J., 2018. Physical properties of the stone meteorites: Implications for the properties of their parent bodies. Geochemistry 78, 269–298. https://doi.org/10.1016/j.chemer.2017.04.002

Flynn, G.J., Durda, D.D., 2004. Chemical and mineralogical size segregation in the impact disruption of inhomogeneous, anhydrous meteorites. Planet. Space Sci. 52, 1129–1140. https://doi.org/10.1016/j.pss.2004.07.010

Flynn, G.J., Klöck, W., Krompholz, R., 1999. Speed of Sound, Elastic and Shear Modulus Measurements on Meteorites: Implications for Cratering and Disruption of Asteroids 30.

Foschini, L., 2001. On the atmospheric fragmentation of small asteroids. Astron. Astrophys. 365, 612–621.

Friedrich, J.M., Wignarajah, D.P., Chaudhary, S., Rivers, M.L., Nehru, C.E., Ebel, D.S., 2008. Three-dimensional petrography of metal phases in equilibrated L chondrites—Effects of shock loading and dynamic compaction. Earth Planet. Sci. Lett. 275, 172–180. https://doi.org/10.1016/j.epsl.2008.08.024

Gattacceca, J., Mccubbin, F.M., Bouvier, A., Grossman, J., 2020. The Meteoritical Bulletin, No. 107. Meteorit. Planet. Sci. 55, 460–462. https://doi.org/10.1111/maps.13440

Gehri, N., Mata-Falcón, J., Kaufmann, W., 2020. Automated crack detection and measurement based on digital image correlation. Constr. Build. Mater. 256, 119383. https://doi.org/10.1016/j.conbuildmat.2020.119383

Gilman, J.J., 1994. Micromechanics of shear banding. Mech. Mater. 17, 83–96. https://doi.org/10.1016/0167-6636(94)90051-5

Goldstein, J.I., Michael, J.R., 2006. The formation of plessite in meteoritic metal. Meteorit. Planet. Sci. 41, 553–570. https://doi.org/10.1111/j.1945-5100.2006.tb00482.x

Goldstein, J.I., Scott, E.R.D., Chabot, N.L., 2009. Iron meteorites: Crystallization, thermal history, parent bodies, and origin. Geochemistry 69, 293–325. https://doi.org/10.1016/j.chemer.2009.01.002

GOM, 2013. ARAMIS user manual–Software.

Gordon, R.B., 1970. Mechanical properties of iron meteorites and the structure of their parent planets. J. Geophys. Res. 75, 439–447. https://doi.org/10.1029/JB075i002p00439

Gorshkov, E.S., 1973. Elastic Properties of Meteorites. Meteoritika 126–135.

Grady, M.M., Wright, I., Lauretta, D.S., McSween, H.Y., 2006. Types of extraterrestrial material available for study. Meteor. Early Sol. Syst. II 3–18.

Greenberg, M.L., Castagna, J.P., 1992. Shear-Wave Velocity Estimation in Porous Rocks: Theoretical Formulation, Preliminary Verification and Applications1. Geophys. Prospect. 40, 195–209. https://doi.org/10.1111/j.1365-2478.1992.tb00371.x

Griffith, A.A., Taylor, G.I., 1921. VI. The phenomena of rupture and flow in solids. Philos. Trans. R. Soc. Lond. Ser. Contain. Pap. Math. Phys. Character 221, 163–198. https://doi.org/10.1098/rsta.1921.0006

Hamza, M.H., Galluscio, C.A., Rabbi, M.F., Garvie, L.A.J., Cotto-Figueroa, D., Asphaug, E., Chattopadhyay, A., 2023. Characterization and Mechanical Testing of Ordinary Chondrites, in: TMS 2023 152nd Annual Meeting & Exhibition Supplemental Proceedings, The Minerals, Metals & Materials Series. Springer Nature Switzerland, Cham, pp. 303–312. https://doi.org/10.1007/978-3-031-22524-6_28

Hart, K.A., 2015. Finite Element Estimation of Meteorite Structural Properties. Presented at the Georgia Tech Student Seminar Series.

Hawkins, G.S., 1960. Asteroidal fragments. Astron. J. 65, 318.

He, Y., Godet, S., Jacques, P.J., Jonas, J.J., 2006. Crystallographic relations between face- and body-centred cubic crystals formed under near-equilibrium conditions: Observations from the Gibeon meteorite. Acta Mater. 54, 1323–1334. https://doi.org/10.1016/j.actamat.2005.11.008

He, Y.L., Godet, S., Jacques, P.J., Jonas, J.J., 2005. Crystallographic Relationships between FCC and BCC Crystals: A Study Using EBSD Techniques. Solid State Phenom. 105, 121–126. https://doi.org/10.4028/www.scientific.net/SSP.105.121

Hogan, J.D., Kimberley, J., Hazeli, K., Plescia, J., Ramesh, K.T., 2015. Dynamic behavior of an ordinary chondrite: The effects of microstructure on strength, failure and fragmentation. Icarus 260, 308–319. https://doi.org/10.1016/j.icarus.2015.07.027

Holsapple, K.A., 2009. On the "strength" of the small bodies of the solar system: A review of strength theories and their implementation for analyses of impact disruptions. Planet. Space Sci. 57, 127–141. https://doi.org/10.1016/j.pss.2008.05.015

Hons, M.S., Hildebrand, A.R., 2004. Compressional and Shear Wave Velocities in Meteorites 2004, P11A-05.

Housen, K., 1999. Scale Effects in Strength-Dominated Collisions of Rocky Asteroids. Icarus 142, 21–33. https://doi.org/10.1006/icar.1999.6206

Hu, E., Wang, W., 2016. The elastic constants measurement of metal alloy by using ultrasonic nondestructive method at different temperature. Math. Probl. Eng. 2016.

Huss, G.R., Rubin, A.E., Grossman, J.N., 2006. Thermal Metamorphism in Chondrites, Meteorites and the Early Solar System II.

Hutchinson, B., Hagström, J., 2006. Austenite decomposition structures in the gibeon meteorite. Metall. Mater. Trans. A 37, 1811–1818. https://doi.org/10.1007/s11661-006-0123-x

Hutchinson, L., Imken, T., Crowley Farenga, J., Solish, B., Matthes, C., Arthur, P., 2023. Psyche Mission Launch and Solar Array Deployment Phase, in: 2023 IEEE Aerospace Conference. Presented at the 2023 IEEE Aerospace Conference, pp. 1–13. https://doi.org/10.1109/AERO55745.2023.10115775

Ibrahim, M., Hildebrand, A., 2012. The Elastic Properties of Carbonaceous Chondrites Apparently Reflect Impact Damage from an Unsampled Weaker Impactor Population. Asteroids Comets Meteors 2012 1667, 6376.

Jain, A.V., Gordon, R.B., Lipschutz, M.E., 1972. Hardness of kamacite and shock histories of 119 meteorites. J. Geophys. Res. 77, 6940–6954. https://doi.org/10.1029/JB077i035p06940

Jedicke, R., Larsen, J., Spahr, T., 2002. Observational selection effects in asteroid surveys and estimates of asteroid population sizes. Asteroids III 71–87.

Jenniskens, P., Rubin, A.E., Yin, Q.-Z., Sears, D.W.G., Sandford, S.A., Zolensky, M.E., Krot, A.N., Blair, L., Kane, D., Utas, J., Verish, R., Friedrich, J.M., Wimpenny, J., Eppich, G.R., Ziegler, K., Verosub, K.L., Rowland, D.J., Albers, J., Gural, P.S., Grigsby, B., Fries, M.D., Matson, R., Johnston, M., Silber, E., Brown, P., Yamakawa, A., Sanborn, M.E., Laubenstein, M., Welten, K.C., Nishiizumi, K., Meier, M.M.M., Busemann, H., Clay, P., Caffee, M.W., Schmitt-Kopplin, P., Hertkorn, N., Glavin, D.P., Callahan, M.P., Dworkin, J.P., Wu, Q., Zare, R.N., Grady, M., Verchovsky, S., Emel'Yanenko, V., Naroenkov, S., Clark, D.L., Girten, B., Worden, P.S., Consortium), (The Novato Meteorite, 2014. Fall, recovery, and characterization of the Novato L6 chondrite breccia. Meteorit. Planet. Sci. 49, 1388–1425. https://doi.org/10.1111/maps.12323

Johnson, A.A., Remo, J.L., 1974. A new interpretation of the mechanical properties of the Gibeon Meteorite. J. Geophys. Res. 79, 1142–1146. https://doi.org/10.1029/JB079i008p01142

Jones, S.F., 2009. Elastic Wave Velocity, Porosity, and Pore Geometry of Ordinary Chondrites and Artificially Shocked Samples xxiii, 178 leaves : ill.; 30 cm. https://doi.org/10.11575/PRISM/22027

Kalasová, D., Zikmund, T., Spurný, P., Haloda, J., Borovička, J., Kaiser, J., 2020. Chemical and physical properties of Žďár nad Sázavou L chondrite and porosity differentiation using computed tomography. Meteorit. Planet. Sci. 55, 1073–1081. https://doi.org/10.1111/maps.13460

Katsura, T., Nakamura, A.M., Takabe, A., Okamoto, T., Sangen, K., Hasegawa, S., Liu, X., Mashimo, T., 2014. Laboratory experiments on the impact disruption of iron meteorites at temperature of near-Earth space. Icarus 241, 1–12. https://doi.org/10.1016/j.icarus.2014.06.007

Khodakovsky, I.L., Petaev, M.I., 1981. The Thermodynamic Properties and Origin of Osbornite, Sinoite, Carlsbergite and Daubreelite in Meteorites, in: Lunar and Planetary Science Conference. pp. 543–545.

Khout, T., 2009. Physical properties of meteorites and their role in planetology 62.

Kimberley, J., Ramesh, K.T., 2011. The dynamic strength of an ordinary chondrite: The dynamic strength of an ordinary chondrite. Meteorit. Planet. Sci. 46, 1653–1669. https://doi.org/10.1111/j.1945-5100.2011.01254.x

Kimberley, J., Ramesh, K.T., Barnouin, O.S., 2011. Rate effects in the failure strength of extraterrestrial materials, in: Proulx, T. (Ed.), Experimental and Applied Mechanics, Volume 6, Conference Proceedings of the Society for Experimental Mechanics Series. Springer New York, New York, NY, pp. 317–320. https://doi.org/10.1007/978-1-4419-9792-0_52

Knott, J., 1997. Recent advances in the micro-modelling of cleavage fracture in steel.

Knox, R., 1970. THE YIELD STRENGTH OF METEORITIC IRON. Meteoritics 5, 63–74. https://doi.org/10.1111/j.1945-5100.1970.tb00391.x

Krot, A.N., Keil, K., Scott, E.R.D., Goodrich, C.A., Weisberg, M.K., 2014. Classification of Meteorites and Their Genetic Relationships, in: Treatise on Geochemistry. Elsevier, pp. 1–63. https://doi.org/10.1016/B978-0-08-095975-7.00102-9

Kuila, U., Prasad, M., 2013. Specific surface area and pore-size distribution in clays and shales: *Specific surface area and pore-size distribution in clays and shales*. Geophys. Prospect. 61, 341–362. https://doi.org/10.1111/1365-2478.12028

Kuls'kov, S., Tomaš, J., Buyakova, S., 2006. Fractal dimension of the surface of porous ceramic materials. Tech. Phys. Lett. 32, 73–75.

Landsman, Z.A., Emery, J.P., Campins, H., Hanuš, J., Lim, L.F., Cruikshank, D.P., 2018. Asteroid (16) Psyche: Evidence for a silicate regolith from spitzer space telescope spectroscopy. Icarus 304, 58–73.

Lauretta, D., Balram-Knutson, S., Beshore, E., Boynton, W., Drouet d'Aubigny, C., DellaGiustina, D., Enos, H., Golish, D., Hergenrother, C., Howell, E., 2017. OSIRIS-REx: sample return from asteroid (101955) Bennu. Space Sci. Rev. 212, 925–984.

Lauretta, D.S., McSween, H.Y., 2006. Meteorites and the early solar system II. University of Arizona Press.

Leroux, H., 2001. Microstructural shock signatures of major minerals in meteorites. Eur. J. Mineral. 13, 253–272. https://doi.org/10.1127/0935-1221/01/0013-0253

Li, S., Wang, S., Li, X., Li, Y., Liu, S., Coulson, I.M., 2012. A new method for the measurement of meteorite bulk volume via ideal gas pycnometry: MEASUREMENT OF METEORITE BULK VOLUME. J. Geophys. Res. Planets 117. https://doi.org/10.1029/2012JE004202

Li, X., Zhang, D., Yu, G., Li, H., Xiao, W., 2021. Research on Damage and Acoustic Emission Properties of Rock Under Uniaxial Compression. Geotech. Geol. Eng. 39, 3549–3562. https://doi.org/10.1007/s10706-021-01710-5

Li, Y., Huang, R., 2015. Relationship between joint roughness coefficient and fractal dimension of rock fracture surfaces. Int. J. Rock Mech. Min. Sci. 75, 15–22. https://doi.org/10.1016/j.ijrmms.2015.01.007

Liang, B., Cuadra, J., Hazeli, K., Soghrati, S., 2020. Stress field analysis in a stony meteorite under thermal fatigue and mechanical loadings. Icarus 335, 113381. https://doi.org/10.1016/j.icarus.2019.07.015

Macke, R.J., 2010. Survey Of Meteorite Physical Properties Density, Porosity And Magnetic Susceptibility 333.

Mainzer, A., Grav, T., Bauer, J., Masiero, J., McMillan, R., Cutri, R., Walker, R., Wright, E., Eisenhardt, P., Tholen, D., 2011. NEOWISE observations of near-Earth objects: Preliminary results. Astrophys. J. 743, 156.

Marchi, S., Durda, D.D., Polanskey, C.A., Asphaug, E., Bottke, W.F., Elkins-Tanton, L.T., Garvie, L.A.J., Ray, S., Chocron, S., Williams, D.A., 2020. Hypervelocity Impact Experiments in Iron-Nickel Ingots and Iron Meteorites: Implications for the NASA Psyche Mission. J. Geophys. Res. Planets 125. https://doi.org/10.1029/2019JE005927

Matsumoto, T., Hasegawa, S., Nakao, S., Sakai, M., Yurimoto, H., 2018. Population characteristics of submicrometer-sized craters on regolith particles from asteroid Itokawa. Icarus 303, 22–33.

Matter, A., Delbo, M., Carry, B., Ligori, S., 2013. Evidence of a metal-rich surface for the Asteroid (16) Psyche from interferometric observations in the thermal infrared. Icarus 226, 419–427.

Mc Crosky, R.E., 1968. The distribution of magnitudes, masses, and energies of large meteoric bodies.

McSween Jr, H.Y., Lauretta, D.S., Leshin, L.A., 2006. Recent advances in meteoritics and cosmochemistry. Meteor. Early Sol. Syst. II 53–66.

Medvedev, R., Gorbatsevich, F., Zotkin, I., 1985. Determination of the physical properties of stony meteorites applied to the study of their destruction processes. Meteoritika 44, 105–110.

Mees, F., Swennen, R., Geet, M.V., Jacobs, P., 2003. Applications of X-ray computed tomography in the geosciences. Geol. Soc. Lond. Spec. Publ. 215, 1–6.

Melosh, H., 1984. Impact ejection, spallation, and the origin of meteorites. Icarus 59, 234–260.

Melosh, H.J., Ryan, E.V., Asphaug, E., 1992. Dynamic fragmentation in impacts: Hydrocode simulation of laboratory impacts. J. Geophys. Res. 97, 14735. https://doi.org/10.1029/92JE01632

Miao, S., Pan, P.-Z., Yu, P., Zhao, S., Shao, C., 2020. Fracture analysis of Beishan granite after high-temperature treatment using digital image correlation. Eng. Fract. Mech. 225, 106847. https://doi.org/10.1016/j.engfracmech.2019.106847

Molaro, J.L., Byrne, S., Langer, S.A., 2015. Grain-scale thermoelastic stresses and spatiotemporal temperature gradients on airless bodies, implications for rock breakdown: Thermoelastic stresses on airless bodies. J. Geophys. Res. Planets 120, 255–277. https://doi.org/10.1002/2014JE004729

Molesky, M.J., Patmore, E.B., Strait, M.M., 2015. Measurement of density and compression strength in meteorites. 78th Annu. Meet. Meteorit. Soc. 2015 1.

Moyano-Cambero, C.E., Pellicer, E., Trigo-Rodríguez, J.M., Williams, I.P., Blum, J., Michel, P., Küppers, M., Martínez-Jiménez, M., Lloro, I., Sort, J., 2017. Nanoindenting the Chelyabinsk Meteorite to Learn about Impact Deflection Effects in asteroids. Astrophys. J. 835, 157. https://doi.org/10.3847/1538-4357/835/2/157

Narayan, C., Goldstein, J.I., 1985. A major revision of iron meteorite cooling rates—An experimental study of the growth of the Widmanstätten pattern. Geochim. Cosmochim. Acta 49, 397–410. https://doi.org/10.1016/0016-7037(85)90032-8

Nelson, M.L., Britt, D.T., Lebofsky, L.A., 1993. Review of asteroid compositions. Resour. - Earth Space 493–522.

Nemat-Nasser, S., Horii, H., 1982. Compression-induced nonplanar crack extension with application to splitting, exfoliation, and rockburst. J. Geophys. Res. Solid Earth 87, 6805–6821. https://doi.org/10.1029/JB087iB08p06805

Nolze, G., Geist, V., Neumann, R.S., Buchheim, M., 2005. Investigation of orientation relationships by EBSD and EDS on the example of the Watson iron meteorite. Cryst. Res. Technol. 40, 791–804. https://doi.org/10.1002/crat.200410434

Norton, O.R., 2002. The Cambridge encyclopedia of meteorites.

Ohtani, E., Sakurabayashi, T., Kurosawa, K., 2022. Experimental simulations of shock textures in BCC iron: implications for iron meteorites. Prog. Earth Planet. Sci. 9, 1–15. https://doi.org/10.1186/s40645-022-00482-7

Opeil, C., Consolmagno, G., Britt, D., 2010. The thermal conductivity of meteorites: New measurements and analysis. Icarus 208, 449–454.

Opeil Sj, C.P., Consolmagno Sj, G.J., Safarik, D.J., Britt, D.T., 2012. Stony meteorite thermal properties and their relationship with meteorite chemical and physical states: Meteorite thermal properties. Meteorit. Planet. Sci. 47, 319–329. https://doi.org/10.1111/j.1945-5100.2012.01331.x

Ostrowski, D., Bryson, K., 2020. Laboratory examination of the physical properties of ordinary chondrites. Meteorit. Planet. Sci. 55, 2007–2020. https://doi.org/10.1111/maps.13562

Ostrowski, D., Bryson, K., 2019. The physical properties of meteorites. Planet. Space Sci. 165, 148–178. https://doi.org/10.1016/j.pss.2018.11.003

Otto, K.A., Matz, K., Schröder, S., Parekh, R., Krohn, K., Honda, R., Kameda, S., Jaumann, R., Schmitz, N., Stephan, K., 2021. Surface roughness of asteroid (162173) Ryugu and comet 67P/Churyumov–Gerasimenko inferred from in situ observations. Mon. Not. R. Astron. Soc. 500, 3178–3193.

Paliwal, B., Ramesh, K.T., 2008. An interacting micro-crack damage model for failure of brittle materials under compression. J. Mech. Phys. Solids 56, 896–923. https://doi.org/10.1016/j.jmps.2007.06.012

Pan, B., 2011. Recent progress in digital image correlation. Exp. Mech. 51, 1223–1235.

Pan, B., Qian, K., Xie, H., Asundi, A., 2009. Two-dimensional digital image correlation for in-plane displacement and strain measurement: a review. Meas. Sci. Technol. 20, 062001. https://doi.org/10.1088/0957-0233/20/6/062001

Parz, P., Leitner, M., Sprengel, W., Reingruber, H., Puff, W., 2013. Defect investigations of an iron-nickel meteorite. J. Phys. Conf. Ser. 443, 012032. https://doi.org/10.1088/1742-6596/443/1/012032

Peng, J., Rong, G., Cai, M., Zhou, C.-B., 2015. A model for characterizing crack closure effect of rocks. Eng. Geol. 189, 48–57. https://doi.org/10.1016/j.enggeo.2015.02.004

Perron, C., Zanda, B., 2005a. Meteorites: samples of NEOs in the laboratory. Comptes Rendus Phys. 6, 345–360. https://doi.org/10.1016/j.crhy.2005.01.005

Perron, C., Zanda, B., 2005b. Meteorites: samples of NEOs in the laboratory. Comptes Rendus Phys. 6, 345–360.

Petrovic, J., 2001. Review mechanical properties of meteorites and their constituents. J. Mater. Sci. 36, 1579–1583.

Petrovic, J.J., 2001. Review Mechanical properties of meteorites and their constituents 5.

Pineau, A., Benzerga, A.A., Pardoen, T., 2016. Failure of metals I: Brittle and ductile fracture. Acta Mater. 107, 424–483. https://doi.org/10.1016/j.actamat.2015.12.034

Pohl, L., Britt, D.T., 2020. Strengths of meteorites—An overview and analysis of available data. Meteorit. Planet. Sci. 55, 962–987. https://doi.org/10.1111/maps.13449

Popova, O., Borovička, J., Hartmann, W.K., Spurný, P., Gnos, E., Nemtchinov, I., Trigo-Rodríguez, J.M., 2011. Very low strengths of interplanetary meteoroids and small

asteroids: Very low strengths of interplanetary meteoroids and small asteroids. Meteorit. Planet. Sci. 46, 1525–1550. https://doi.org/10.1111/j.1945-5100.2011.01247.x

Popova, O.P., Jenniskens, P., Emel'yanenko, V., Kartashova, A., Biryukov, E., Khaibrakhmanov, S., Shuvalov, V., Rybnov, Y., Dudorov, A., Grokhovsky, V.I., 2013. Chelyabinsk airburst, damage assessment, meteorite recovery, and characterization. Science 342, 1069–1073.

Rabbi, M. F., Datta, S., Chattopadhyay, A., Garvie, L.A., Asphaug, E., Cotto-Figueroa, D., 2021. Mechanical Characterization and Brittle Failure of Stony Meteorite (Aba Panu) using Digital Image Correlation, in: AIAA Scitech 2021 Forum. Presented at the AIAA Scitech 2021 Forum, American Institute of Aeronautics and Astronautics, VIRTUAL EVENT. https://doi.org/10.2514/6.2021-0169

Rabbi, M F, Garvie, L.A.J., Cotto-Figueroa, D., Asphaug, E., Khafagy, K.H., Datta, S., Chattopadhyay, A., 2021. Understanding asteroidal failure through quasi-static compression testing and 3-D digital image correlation of the Aba Panu (L3) chondrite. Meteorit. Planet. Sci. maps.13761. https://doi.org/10.1111/maps.13761

Rabbi, M.F., Hamza, M.H., Garvie, L.A.J., Cotto-Figueroa, D., Asphaug, E., Chottopadhyay, A., 2023. Investigation of Mechanical Properties of the Viñales (L6) Ordinary Chondrite.

Rabbi, M.F., Khafagy, K.H., Garvie, L.A.J., Asphaug, E., Cotto-Figueroa, D., Chattopadhyay, A., 2022. Strength and Failure Characterization of the Gibeon (IVA) Iron Meteorite, in: Zhang, M., Li, J., Li, B., Monteiro, S.N., Ikhmayies, S., Kalay, Y.E., Hwang, J.-Y., Escobedo-Diaz, J.P., Carpenter, J.S., Brown, A.D., Soman, R., Peng, Z. (Eds.), Characterization of Minerals, Metals, and Materials 2022, The Minerals, Metals & Materials Series. Springer International Publishing, Cham, pp. 17–23. https://doi.org/10.1007/978-3-030-92373-0_2

Ramesh, K.T., Hogan, J.D., Kimberley, J., Stickle, A., 2015. A review of mechanisms and models for dynamic failure, strength, and fragmentation. Planet. Space Sci., VIII Workshop on Catastrophic Disruption in the Solar System 107, 10–23. https://doi.org/10.1016/j.pss.2014.11.010

Remo, J.L., Johnson, A.A., 1975. A preliminary study of the ductile-brittle transition under impact conditions in material from an octahedrite. J. Geophys. Res. 80, 3744–3748. https://doi.org/10.1029/JB080i026p03744

ReVelle, D.O., 2001. Bolide dynamics and luminosity modeling: Comparisons between uniform bulk density and porous meteoroid models. Presented at the European Space Agency, (Special Publication) ESA SP, pp. 513–517.

Riad, R., Ibhi, A., Douzi, H., Elhajji, M., Rozenbaum, O., Harba, R., Jennane, R., 2014. Investigation of the meteorites porosity by X-ray tomography and 3D image

processing, in: 2014 Second World Conference on Complex Systems (WCCS). IEEE, pp. 710–714.

Richardson, D.C., Leinhardt, Z.M., Melosh, H.J., Bottke, W.F., Jr., Asphaug, E., 2002. Gravitational Aggregates: Evidence and Evolution, Asteroids III.

Rivkin, A.S., Cheng, A.F., 2023. Planetary defense with the Double Asteroid Redirection Test (DART) mission and prospects. Nat. Commun. 14, 1003. https://doi.org/10.1038/s41467-022-35561-2

Rouquerol, J., Avnir, D., Fairbridge, C.W., Everett, D.H., Haynes, J.M., Pernicone, N., Ramsay, J.D.F., Sing, K.S.W., Unger, K.K., 1994. Recommendations for the characterization of porous solids (Technical Report). Pure Appl. Chem. 66, 1739–1758. https://doi.org/10.1351/pac199466081739

Rubin, A., Ma, C., 2021. Meteorite mineralogy. Cambridge University Press.

Rubin, A.E., 1997. Mineralogy of meteorite groups. Meteorit. Planet. Sci. 32, 231–247. https://doi.org/10.1111/j.1945-5100.1997.tb01262.x

Saouma, V.E., Barton, C.C., 1994. Fractals, fractures, and size effects in concrete. J. Eng. Mech. 120, 835–854.

Sasso, M.R., Macke, R.J., Boesenberg, J.S., Britt, D.T., Rivers, M.L., Ebel, D.S., Friedrich, J.M., 2009. Incompletely compacted equilibrated ordinary chondrites. Meteorit. Planet. Sci. 44, 1743–1753.

Schneider, C.A., Rasband, W.S., Eliceiri, K.W., 2012. NIH Image to ImageJ: 25 years of image analysis. Nat. Methods 9, 671–675. https://doi.org/10.1038/nmeth.2089

Schubnel, A., Guéguen, Y., 2003. Dispersion and anisotropy of elastic waves in cracked rocks. J. Geophys. Res. Solid Earth 108.

Scott, E.R.D., 2020. Iron Meteorites: Composition, Age, and Origin, in: Oxford Research Encyclopedia of Planetary Science. Oxford University Press. https://doi.org/10.1093/acrefore/9780190647926.013.206

Sears, D.W., 2004. The origin of chondrules and chondrites. Cambridge University Press.

Sears, D.W., Bryson, K., Ostrowski, D., 2016. The internal structure of Earth-impacting meteoroids: The view from the microscope, the laboratory bench, and the telescope, in: 54th AIAA Aerospace Sciences Meeting. Presented at the 54th AIAA Aerospace Sciences Meeting, American Institute of Aeronautics and Astronautics, San Diego, California, USA. https://doi.org/10.2514/6.2016-0997

Sears, D.W.G., Ostrowski, D.O., Bryson, K., Venkatapathy, E., Lee, T.J., Dotson, J., Syal, M., Swift, D.C., 2015. PLANETARY DEFENSE: A METEORITE PERSPECTIVE. p. 11.

Shoemaker, E.M., 1983. Asteroid and comet bombardment of the Earth. Annu. Rev. Earth Planet. Sci. 11, 461–494.

Short, J.M., Andersen, C.A., 1965. Electron microprobe analyses of the Widmanstätten structure of nine iron meteorites. J. Geophys. Res. 1896-1977 70, 3745–3759. https://doi.org/10.1029/JZ070i015p03745

Sing, K.S.W., 1998. Adsorption methods for the characterization of porous materials. Adv. Colloid Interface Sci. 76–77, 3–11. https://doi.org/10.1016/S0001-8686(98)00038-4

Slyuta, E.N., 2017. Physical and mechanical properties of stony meteorites. Sol. Syst. Res. 51, 64–85. https://doi.org/10.1134/S0038094617010051

Slyuta, E.N., 2013. Physicomechanical properties and gravitational deformation of metallic asteroids. Sol. Syst. Res. 47, 109–126. https://doi.org/10.1134/S0038094613010085

Slyuta, E.N., 2010. Physical-Mechanical Anisotropy of Ordinary Chondrites and the Shape of Small Rocky Bodies 41, 1103.

Soini, A. -J., Kukkonen, I.T., Kohout, T., Luttinen, A., 2020. Thermal and porosity properties of meteorites: A compilation of published data and new measurements. Meteorit. Planet. Sci. 55, 402–425. https://doi.org/10.1111/maps.13441

Svetsov, V., Nemtchinov, I., Teterev, A., 1995. Disintegration of large meteoroids in Earth's atmosphere: Theoretical models. Icarus 116, 131–153.

Taylor, S.R., 2016. Lunar science: A post-Apollo view: Scientific results and insights from the lunar samples. Elsevier.

Thomas, C.A., Naidu, S.P., Scheirich, P., Moskovitz, N.A., Pravec, P., Chesley, S.R., Rivkin, A.S., Osip, D.J., Lister, T.A., Benner, L.A.M., Brozović, M., Contreras, C., Morrell, N., Rożek, A., Kušnirák, P., Hornoch, K., Mages, D., Taylor, P.A., Seymour, A.D., Snodgrass, C., Jørgensen, U.G., Dominik, M., Skiff, B., Polakis, T., Knight, M.M., Farnham, T.L., Giorgini, J.D., Rush, B., Bellerose, J., Salas, P., Armentrout, W.P., Watts, G., Busch, M.W., Chatelain, J., Gomez, E., Greenstreet, S., Phillips, L., Bonavita, M., Burgdorf, M.J., Khalouei, E., Longa-Peña, P., Rabus, M., Sajadian, S., Chabot, N.L., Cheng, A.F., Ryan, W.H., Ryan, E.V., Holt, C.E., Agrusa, H.F., 2023. Orbital Period Change of Dimorphos Due to the DART Kinetic Impact. Nature 1–3. https://doi.org/10.1038/s41586-023-05805-2

Thomason, P., 1990. Ductile fracture of metals. Pergamon Press Plc Ductile Fract. Met. 1990 219.

Tiryakioğlu, M., 2015. Weibull Analysis of Mechanical Data for Castings II: Weibull Mixtures and Their Interpretation. Metall. Mater. Trans. A 46, 270–280. https://doi.org/10.1007/s11661-014-2610-9

Tsuchiyama, A., Mashio, E., Imai, Y., Noguchi, T., Miura, Y., Yano, H., Nakamura, T., 2009. Strength Measurement of Carbonaceous Chondrites and Micrometeorites Using Micro Compression Testing Machine. Meteorit. Planet. Sci. Suppl. 72, 5189.

Tsvetkov, V.I., Skripnik, A.Y., 1991. Atmospheric Fragmentation of Meteorites According to the Strength Theory. Sol. Syst. Res. 25, 273.

Ueki, S., Mine, Y., Takashima, K., 2021. Excellent mechanical properties of taenite in meteoric iron. Sci. Rep. 11, 4750. https://doi.org/10.1038/s41598-021-83792-y

Uhlig, H.H., 1955. Contribution of metallurgy to the origin of meteorites Part II—the significance of neumann bands in meteorites. Geochim. Cosmochim. Acta 7, 34–42. https://doi.org/10.1016/0016-7037(55)90043-0

Vaneghi, R.G., Saberhosseini, S.E., Dyskin, A.V., Thoeni, K., Sharifzadeh, M., Sarmadivaleh, M., 2021. Sources of variability in laboratory rock test results. J. Rock Mech. Geotech. Eng. 13, 985–1001. https://doi.org/10.1016/j.jrmge.2021.03.007

Veski, S., Heinsalu, A., Kirsimäe, K., Poska, A., Saarse, L., 2001. Ecological catastrophe in connection with the impact of the Kaali meteorite about 800–400 B.C. on the island of Saaremaa, Estonia. Meteorit. Planet. Sci. 36, 1367–1375. https://doi.org/10.1111/j.1945-5100.2001.tb01830.x

Voropaev, S.A., Kocherov, A.V., Lorenz, C.A., Korochantsev, A.V., Dushenko, N.V., Kuzina, D.M., Nugmanov, I.I., Jianguo, Y., 2017. Features in constructing a certificate of strength of extraterrestrial material by the example of the Chelyabinsk meteorite. Dokl. Phys. 62, 486–489. https://doi.org/10.1134/S1028335817100111

Walker, R.M., Cameron, A.G.W., 2006. Meteorites and the Early Solar System II. University of Arizona Press. https://doi.org/10.2307/j.ctv1v7zdmm

Weibull, W., 1951. A statistical distribution function of wide applicability. J. Appl. Mech.

Weiss, B.P., Vali, H., Baudenbacher, F.J., Kirschvink, J.L., Stewart, S.T., Shuster, D.L., 2002. Records of an ancient Martian magnetic field in ALH84001. Earth Planet. Sci. Lett. 201, 449–463.

Wheeler, J.M., 2021. Mechanical phase mapping of the Taza meteorite using correlated high-speed nanoindentation and EDX. J. Mater. Res. 36, 94–104. https://doi.org/10.1557/s43578-020-00056-7

Wilkison, S.L., McCOY, T.J., McCAMANT, J.E., Robinson, M.S., Britt, D.T., 2003. Porosity and density of ordinary chondrites: Clues to the formation of friable and porous ordinary chondrites. Meteorit. Planet. Sci. 38, 1533–1546.

Wu, J., Jin, X., Mi, S., Tang, J., 2020. An effective method to compute the box-counting dimension based on the mathematical definition and intervals. Results Eng. 6, 100106.

Yadav, S., Sagapuram, D., 2020. In situ analysis of shear bands and boundary layer formation in metals. Proc. R. Soc. Math. Phys. Eng. Sci. 476, 20190519. https://doi.org/10.1098/rspa.2019.0519

Yang, J., Goldstein, J.I., Scott, E.R.D., 2010. Main-group pallasites: Thermal history, relationship to IIIAB irons, and origin. Geochim. Cosmochim. Acta 74, 4471–4492. https://doi.org/10.1016/j.gca.2010.04.016

Yang, J., Goldstein, J.I., Scott, E.R.D., 2007. Iron meteorite evidence for early formation and catastrophic disruption of protoplanets. Nature 446, 888–891. https://doi.org/10.1038/nature05735

Yang, J., Goldstein, J.I., Scott, E.R.D., Michael, J.R., Kotula, P.G., Pham, T., McCOY, T.J., 2011. Thermal and impact histories of reheated group IVA, IVB, and ungrouped iron meteorites and their parent asteroids. Meteorit. Planet. Sci. 46, 1227–1252. https://doi.org/10.1111/j.1945-5100.2011.01210.x

Yang, M., Zhao, M., Cao, W., 2005. Method for determining the parameters of statistical damage softening constitutive model for rock. J. Hydraul. Eng. 36, 345–349.

Yeomans, D., Chodas, P., 2013. Additional details on the large fireball event over Russia on Feb. 15, 2013. NASA NEO Program Off. Announc. March 1.

Yin, F., Dai, D., 2021. Petrology and mineralogy of the Viñales meteorite, the latest fall in Cuba. Sci. Prog. 104, 003685042110198. https://doi.org/10.1177/00368504211019859

Yoshikawa, M., Kawaguchi, J., Fujiwara, A., Tsuchiyama, A., 2015. Hayabusa sample return mission. Asteroids IV 1, 1.

Zanda, B., Rotaru, M., 2001. Meteorites: their impact on science and history. Cambridge University Press.

Zotkin, I., Medvedev, P., Gorbatsevich, F., 1987. The strength properties of the Tsarev meteorite. Meteoritika 46, 86–93.